AFWAL-TR-84-4073

AD-A146 630

CONSTITUTIVE MODELING OF ENGINE MATERIALS

Dr. Dale A. Wilson
Pratt & Whitney
Government Products Division
P.O. Box 2691, West Palm Beach, Florida 33402

and

Dr. Kevin P. Walker
Hibbitt, Karlsson, Sorensen, Inc.
35 South Angell Street
Providence, Rhode Island 02906
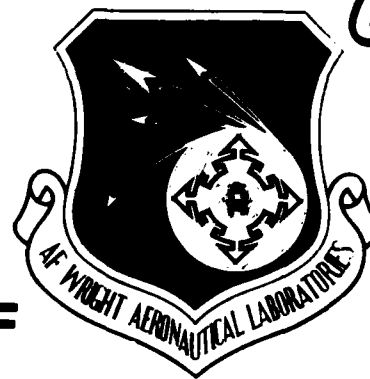
July 1984

Final Report for Period July 1981 - October 1983

MATERIALS LABORATORY
AIR FORCE WRIGHT AERONAUTICAL LABORATORIES
WRIGHT-PATTERSON AIR FORCE BASE, OHIO 45433
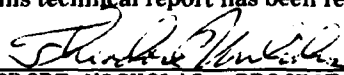
DTIC
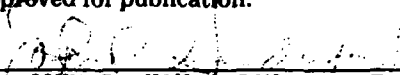ELECTE
OCT 1 5 1984

E

84 10 15 015

NOTICE

When Government drawings, specifications, or other data are used for any purpose other than in connection with a definitely related Government procurement operation, the United States Government thereby incurs no responsibility nor any obligation whatsoever; and the fact that the Government may have formulated, furnished, or in any way supplied the said drawings, specifications, or other data, is not to be regarded by implication or otherwise as in any manner licensing the holder or any other person or corporation, or conveying any rights or permission to manufacture, use, or sell any patented invention that may in any way be related thereto.
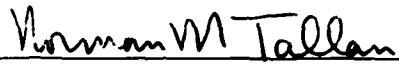
This report has been reviewed by the Office of Public Affairs (ASD/PA) and is releasable to the National Technical Information Service (NTIS). At NTIS, it will be available to the general public, including foreign nations.

This technical report has been reviewed and is approved for publication.

THEODORE NICHOLAS, PROJECT ENGINEER
METALS BEHAVIOR BRANCH
METALS AND CERAMICS DIVISION

JOHN P. HENDERSON, CHIEF
METALS BEHAVIOR BRANCH
METALS AND CERAMICS DIVISION

FOR THE COMMANDER

NORMAN M. TALLAN, CHIEF
METALS AND CERAMICS DIVISION
MATERIALS LABORATORY

REPORT DOCUMENTATION PAGE

1a. REPORT SECURITY CLASSIFICATION UNCLASSIFIED	1b. RESTRICTIVE MARKINGS
2a. SECURITY CLASSIFICATION AUTHORITY	3. DISTRIBUTION/AVAILABILITY OF REPORT Approved for public release; distribution unlimited.
2b. DECLASSIFICATION/DOWNGRADING SCHEDULE	

4. PERFORMING ORGANIZATION REPORT NUMBER(S) FR-17911	5. MONITORING ORGANIZATION REPORT NUMBER(S) AFWAL-TR-84-4073.

6a. NAME OF PERFORMING ORGANIZATION United Technologies Pratt & Whitney	6b. OFFICE SYMBOL (If applicable)	7a. NAME OF MONITORING ORGANIZATION Materials Laboratory (AFWAL/MLLN)
6c. ADDRESS (City, State and ZIP Code) Government Products Division West Palm Beach, FL 33402		7b. ADDRESS (City, State and ZIP Code) Air Force Wright Aeronautical Laboratories Wright-Patterson AFB OH 45433

8a. NAME OF FUNDING/SPONSORING ORGANIZATION	8b. OFFICE SYMBOL (If applicable)	9. PROCUREMENT INSTRUMENT IDENTIFICATION NUMBER Contract F33615-81-C-5040

8c. ADDRESS (City, State and ZIP Code)	10. SOURCE OF FUNDING NOS.			
	PROGRAM ELEMENT NO.	PROJECT NO.	TASK NO.	WORK UNIT NO.
	62102F	2420	03	11

11. TITLE (Include Security Classification)
Constitutive Modeling of Engine Materials

12. PERSONAL AUTHOR(S)
Kevin P. Walker and Dale A. Wilson

13a. TYPE OF REPORT Final	13b. TIME COVERED FROM Jul 81 TO Oct 83	14. DATE OF REPORT (Yr., Mo., Day) July 1984	15. PAGE COUNT 85

16. SUPPLEMENTARY NOTATION

17. COSATI CODES			18. SUBJECT TERMS (Continue on reverse if necessary and identify by block number)
FIELD	GROUP	SUB. GR.	Constitutive Modeling, Crack Growth, Creep Crack Growth, Elevated Temperature, Fatigue, INCONEL 718, ABAQUS
11	06		
20	11		

19. ABSTRACT (Continue on reverse if necessary and identify by block number)
This investigation examines the capability to predict the growth of cracks in critical structural components operating at elevated temperatures where time-dependent behavior occurs. A viscoplasic constitutive model for INCO 718 was developed to determine this behavior in the area of the crack tip. The model constants were obtained from monotonically increasing, cyclic, and sustained loading. Therefore, the model has the capability to account for load history effects as well as material damage accumulation. Theoretical predictions are compared to the experimental results.

20. DISTRIBUTION/AVAILABILITY OF ABSTRACT UNCLASSIFIED/UNLIMITED ☒ SAME AS RPT. ☐ DTIC USERS ☐	21. ABSTRACT SECURITY CLASSIFICATION Unclassified
22a. NAME OF RESPONSIBLE INDIVIDUAL T. Nicholas	22b. TELEPHONE NUMBER (Include Area Code) 513-255-2689	22c. OFFICE SYMBOL AFWAL/MLLN

DD FORM 1473, 83 APR   EDITION OF 1 JAN 73 IS OBSOLETE.   UNCLASSIFIED

PREFACE

Accession For

NTIS GRA&I	☒
DTIC TAB	☐
Unannounced	☐
Justification	

By_____
Distribution/_____
Availability Codes

Dist	Avail and/or Special
A-1	

iii

4130C

CONTENTS

ILLUSTRATIONS

467:X

ILLUSTRATIONS

ILLUSTRATIONS

ILLUSTRATIONS

TABLES

SECTION 1.0

INTRODUCTION

The Air Force and Pratt & Whitney are developing technology to allow for an eventual damage tolerant design approach to turbine engine components and to retire existing components based on the detection of service initiated flaws. This approach is based heavily on the capability to predict the growth of flaws in critical structural components during the service life of the component. The majority of critical structural components operate at elevated temperatures where plasticity and time-dependent creep occur, particularly in regions of stress concentrations and near the tips of fatigue cracks. Considerable research is currently being conducted on modeling crack growth behavior in engine materials. These research efforts require an understanding of crack tip behavior in order to successfully evolve realistic crack growth criteria. Because of the complex inelastic behavior, closed-form solutions to crack problems are not practical. An alternate approach is to use finite element methods for modeling the test geometries. Such an approach, however, depends heavily on realistic constitutive models of the material behavior as well as localized failure criteria for crack growth problems.

The objective of this contract is to develop a constitutive model for engine materials at elevated temperatures where creep and plasticity occur and to apply this model in numerical computations of creep and fatigue crack propagation. The constitutive model has the capability to model the types of material behavior which occur under loading conditions typical of turbine engine disks, and yet is mathematically efficient to allow calculations of crack growth behavior under cyclic loading conditions. It is expected that the results obtained in this program will be applied to the modeling of laboratory test specimens under engine spectrum loading and eventually to the prediction of stress and strain fields in turbine engine components with creep/fatigue cracks.

The program involved the development of a constitutive model for INCO 718, a nickel base alloy, at 1200°F (649°C) under monotonic, cyclic, and sustained loading. The model has the capability of accounting for load history effects as well as material failure or damage accumulation. The model has been incorporated into a two-dimensional finite element program to simulate the crack growth behavior in laboratory test specimens, and data have been generated to evaluate the applicability of the model. The model development was based on prior constitutive modeling efforts, and as such, primarily involved modifications and refinements to established approaches.

1-1

SECTION 2.0

TECHNICAL APPROACH

2.1 PROBLEM DESCRIPTION AND SOLUTION APPROACH

The research effort in this contract is directed towards the development of a nonlinear fracture mechanics capability to predict crack growth at elevated temperatures under both creep and fatigue loading conditions.

At elevated temperatures the material in the vicinity of a crack tip can fail or rupture under both creep (constant load) and fatigue (alternating load) conditions due to the high stress concentration. To predict crack growth analytically it is first necessary to determine the stress-strain behavior of the material in the vicinity of the crack tip. Once the stress and strain histories are known at a particular material point, the time or the number of load cycles required to fail the material at that point can then be determined by a suitable failure criterion.

This contract has concentrated on determining the crack growth in compact type specimens of INCO 718 material at 1200°F (649°C) under creep, fatigue, and combined creep-fatigue conditions. The theoretical effort makes use of a unified viscoplastic constitutive formulation to determine the time-dependent material behavior in the crack tip vicinity, while a continuum damage model is used to predict either the time or the number of load cycles required to fail a particular point in the crack tip neighborhood. Both the viscoplastic constitutive model and the continuum damage model have been incorporated as FORTRAN subroutines into the ABAQUS [1] general purpose nonlinear finite element program. When the continuum damage criterion dictates that the material at the Gaussian integration point in the finite element closest to the crack tip has failed, the node at the crack tip is released, and the crack advances to the adjacent node in the crack plane.

The experimental crack growth measurements were made under both creep (constant load) and fatigue (alternating load) conditions.

Under creep conditions the small amount of crack growth is difficult to determine by conventional experimental crack measuring techniques. Instead of measuring crack length as a function of time, the displacement of two points located on either side of the crack tip is monitored as a function of time by an optical interferometric displacement measurement technique. The nodes along the crack plane in the finite element model are released in such a manner that the computed displacements of the two points due to both the viscoplastic material behavior and the crack growth matches the experimental displacements as time progresses. Crack length, as a function of time, then becomes a product of the finite element analysis rather than an input. Since the failure criterion under creep conditions is determined by a continuum damage model, the material constants in this model can be chosen to give a least square fit to the creep crack growth experiments in the INCO 718 compact type specimen at 1200°F (649°C) carried out under different applied loads. The material constants in the continuum damage model can also be determined to give a least square fit to the creep rupture data obtained from uncracked uniaxial specimens of INCO 718 at 1200°F (649°C). If creep crack growth is governed by creep rupture of the material directly ahead of the crack tip, then the material constants determined from the creep rupture experiments on the uncracked uniaxial specimens should coincide with those obtained from the creep crack growth experiments on the compact type specimens.

In the fatigue crack growth experiments the crack length versus load cycle number can be measured by a conventional traveling microscope. Once again the nodes along the crack plane in

the finite element model are released in such a manner that the computed crack length versus load cycle number matches the experimental crack growth rate. The failure criterion under fatigue conditions is also determined by a continuum damage model. Material constants in this model can be chosen to give a least square fit to the fatigue crack growth experiments in the INCO 718 compact type specimen at 1200°F (649°C). They can also be chosen to give a least square fit to conventional fatigue failure data obtained from experiments at different load amplitudes on uniaxial bar specimens of INCO 718 at 1200°F (649°C). If fatigue crack growth is governed by fatigue rupture of the material directly ahead of the crack tip, then the material constants in the continuum damage model obtained from the fatigue experiments on the uncracked uniaxial specimens should coincide with those obtained from the fatigue crack growth experiments on the compact type specimens.

The viscoplastic constitutive model used in the creep crack growth predictions is presented in an integral form in Appendix A. Two state variables, representing the effect of the inelastic deformation history on the subsequent response of the material, are incorporated into the model. The tensor state variable Ω_{ij} allows the model to exhibit a nonlinear kinematic hardening response, while the scalar state variable K allows for isotropic hardening. In the absence of thermal recovery, the state variable Ω_{ij} represents the stress state which is obtained under very slow loading conditions. It is also the stress state to which the material will relax under conditions where the components of the strain tensor are held at a constant value. In the literature the state variable Ω_{ij} is called the equilibrium, rest, or back stress while the state variable K is called the drag stress.

The model has been used to describe Hastelloy-X constitutive behavior with the inelastic strain rate depending upon a power law expression of the stress minus the equilibrium stress. However, at strain rates above 10^{-4} per second, a power law expression for the inelastic strain rate tends to overestimate the stress. For this reason, the modelling of INCO 718 data was accomplished by using the exponential expression given in Appendix B. In the integral formulation presented in Appendix A, the dependence of inelastic strain rate on stress is given by the logarithmic term in equation (6) for the expression Q(t). The exponential law allows the inelastic strain rate to grow more rapidly with increasing stress values than the power law; conversely, the stress increases more slowly with increasing strain rate using the exponential expression for the inelastic strain rate. The exponential variation of strain rate with stress is similar to the hyperbolic sine function used in Miller's viscoplastic model [2]. At strain rates above 10^{-4} per second INCO 718 exhibits a rate insensitive material response and the strong nonlinear dependence of inelastic strain rate on stress, given by the exponential (or hyperbolic sine) expression, is needed to model this behavior.

The constitutive model in Appendix A also has the damage parameter D incorporated into its formulation. This damage may be assumed to be due to creep, fatigue, or creep-fatigue interaction. Its growth must be specified by a suitable evolution equation. For the creep crack growth predictions the damage parameter D is assumed to evolve with creep damage according to Chaboche's creep rupture law presented in Appendix C.

Viscoplastic constitutive models are usually given in differential form. A differential equation relating the inelastic strain rate with stress and state variables is given together with differential equations governing the growth of the state variables with deformation history. In the present formulation, two state variables, viz. the equilibrium stress and drag stress, are used.

Equation (1) of Appendix A is an integral form of the differential equation governing the growth of the inelastic strain rate with stress and state variables Ω_{ij} and K. The integral expression contains the rate-dependent term Q(t), which governs the rate sensitivity, of the constitutive model. This term also contains the drag stress state variable K, which governs the "yield" behavior of the material and its isotropic cyclic hardening response.

Equation (2) of Appendix A is the integral form of the differential expression governing the growth of the equilibrium stress state variable. The first term, given by equation (5), allows the material to exhibit an asymmetric response in tension and compression under both tensile loading and creep conditions. The second term in equation (2) governs the slope of the equilibrium stress versus strain curve at large strain values. Since this term is linear in the inelastic strain, the variation of the equilibrium stress with strain, and hence the variation of the actual stress with strain, is linear at large values. This may be seen from equation (1) since the integral term containing Q(t) saturates to a constant value under large strain conditions. The third term in equation (2) governs the growth of the equilibrium stress with deformation history in the intermediate strain region; it saturates to a constant value at large strains.

Equation (3) of Appendix A governs the growth of the drag stress with cumulative deformation history. In the present calculations no thermal recovery is included in the drag stress state variable, but this can easily be incorporated if required.

The constitutive formulation has been incorporated into the ABAQUS nonlinear finite element program in both its differential and integral forms. For creep crack growth predictions in high strength creep resistant alloys such as INCO 718, most of the creep crack growth occurs due to the release of nodes along the crack plane; little crack growth occurs due to viscoplastic material behavior in the vicinity of the crack tip. For this reason, creep crack growth predictions can be made with any constitutive relation which provides an adequate description of inelastic strain rate versus stress state.

The use of combined experimental and theoretical procedures to determine crack growth criteria has been labeled the Hybrid Experimental-Numerical procedure by Kobayashi [3]. Hinnerichs [4] used this procedure to determine a creep crack growth criterion for IN100 at 1350°F (732°C) from experiments carried out on a center cracked plate test specimen by Sharpe [5]. He found that a critical damage accumulation criterion for creep crack growth similar to that employed in the present contract gave good correlation with the experiments conducted by Sharpe.

2.2 CONSTITUTIVE FORMULATION

Cyclic hysteresis loops and creep curves have been generated for INCO 718 at 1200°F (649°C). Figure 2-1 shows a plot of log σ vs log ε from creep tests and cyclic hysteresis loops generated in the present contract and from tests conducted by Domas, Sharpe, Ward, and Yau [6] in NASA contract NAS3-22522. The plot shows the variation of secondary creep rate (or extension rate in a tensile/hysteresis test) with applied stress. At the largest strain rate of 5.3×10^{-3} per second, the stress point is the estimated ultimate stress value. Discrepancies between the present data and that generated by Domas, et al [6], occur at both low and high stress levels. At high stress levels corresponding to the uniaxial tensile tests, the data points are estimates obtained by extrapolating the test data to obtain the ultimate stress values.

At high strain rates (10^{-4} to 10^{-3} per second) the material behavior becomes insensitive to strain rate. This may be seen by the flattening of the log σ vs log ε curves as shown in Figure 2-1 and is exhibited by the data generated in this contract and in the data generated by Sharpe and his colleagues. The rate insensitivity can also be seen in the cyclic hysteresis loops shown in Figure 2-2, where the first 30 cycles were carried out at a strain amplitude of ± 0.5 percent at a strain rate of $\varepsilon = 3.33 \times 10^{-3}$ per second, while the following 10 cycles were carried out at a strain rate of $\varepsilon = 3.33 \times 10^{-4}$ per second. No discernible difference in the loops due to the decrease in strain rate by an order of magnitude can be detected. The hysteresis loops carried out under strain control at amplitudes of ± 0.8 percent and ± 1.0 percent shown in Figures 2-3 and 2-4 also displayed no discernible sensitivity to strain rate increases and decreases by an order of magnitude.
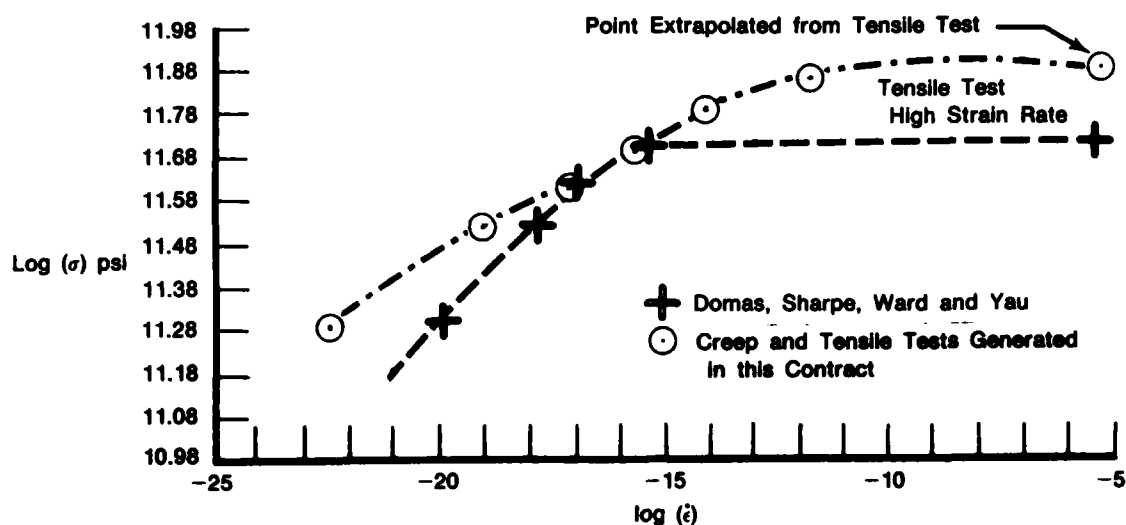
Figure 2-1. *Plot of Log (Stress) vs Log (Plastic Strain Rate) from Creep and Tensile Tests on INCO 718 at 649°C*
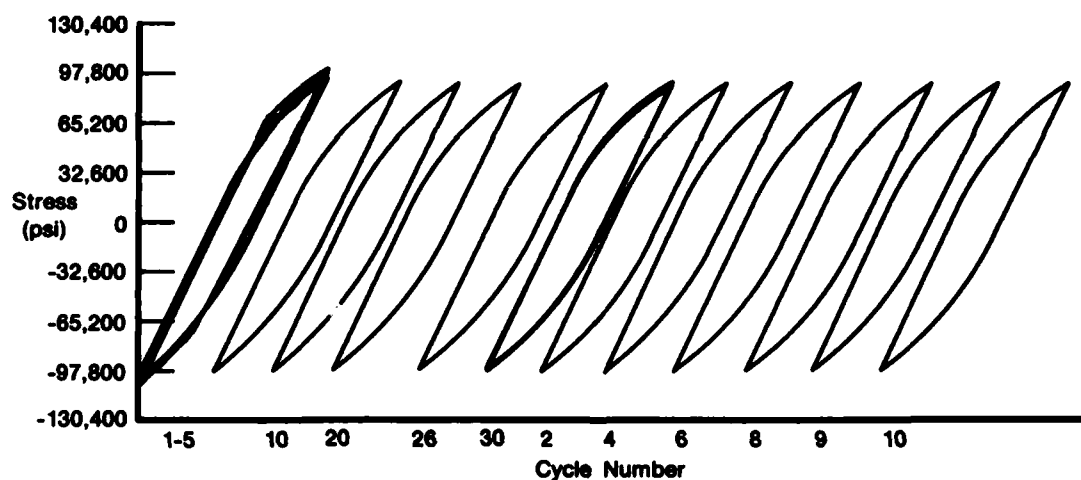
Figure 2-2. *Cyclic Strain Controlled Hysteresis Loops at ± 0.5 Percent Strain Amplitude. The First 30 Cycles are Carried Out at a Strain Rate of $\varepsilon = 3.33 \times 10^{-3}$ Per Second. The Next 10 Cycles are Carried Out at a Strain Rate of $\varepsilon = 3.33 \times 10^{-4}$ Per Second*

2-4
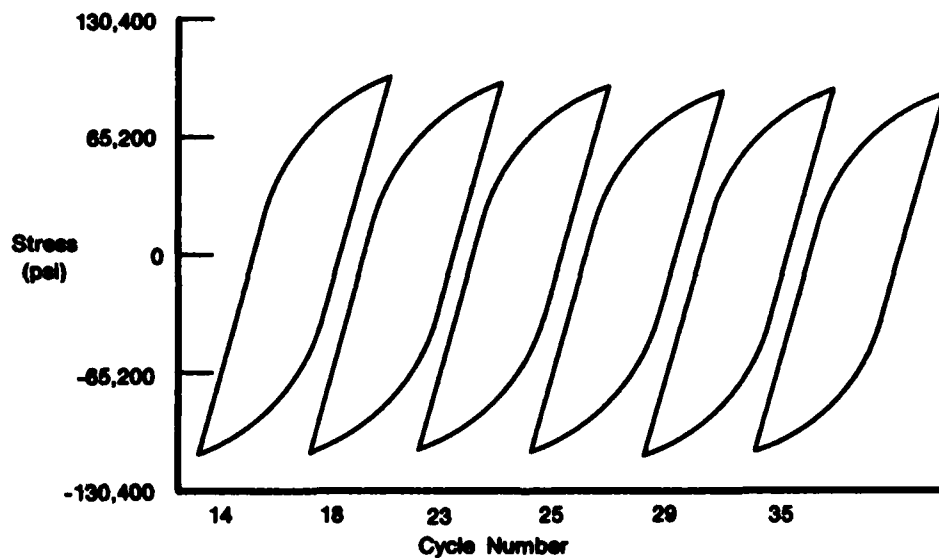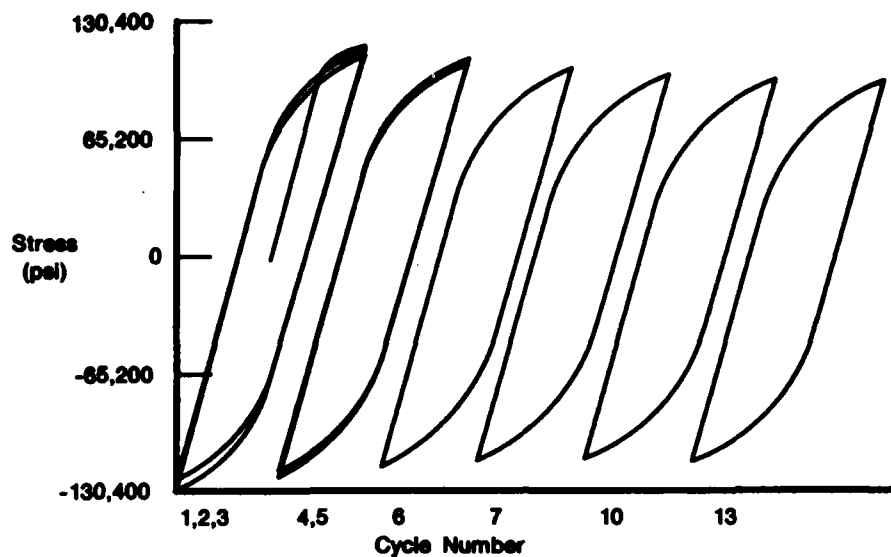
FD 268872

Figure 2-3. Cyclic Strain Controlled Hysteresis Loops at ± 0.8 Percent Strain Amplitude. Loops Were Carried Out at a Strain Rate of $\varepsilon = 5.33 \times 10^{-4}$ Per Second. Loops Carried Out at $\varepsilon = 5.33 \times 10^{-3}$ Per Second and $\varepsilon = 5.33 \times 10^{-5}$ Per Second Showed No Discernible Difference to the Loops Shown Above

2-5

Stress
(psi)

130,400
97,800
65,200
32,600
0
— 32,600
— 65,200
— 97,800
—130,400

1   4   8   12   20   40   60   80

Cycle Number

Stress
(psi)

130,400
97,800
65,200
32,600
0
— 32,600
— 65,200
— 97,800
—130,400

100   122   138   140   142   143-144   145-146

Cycle Number
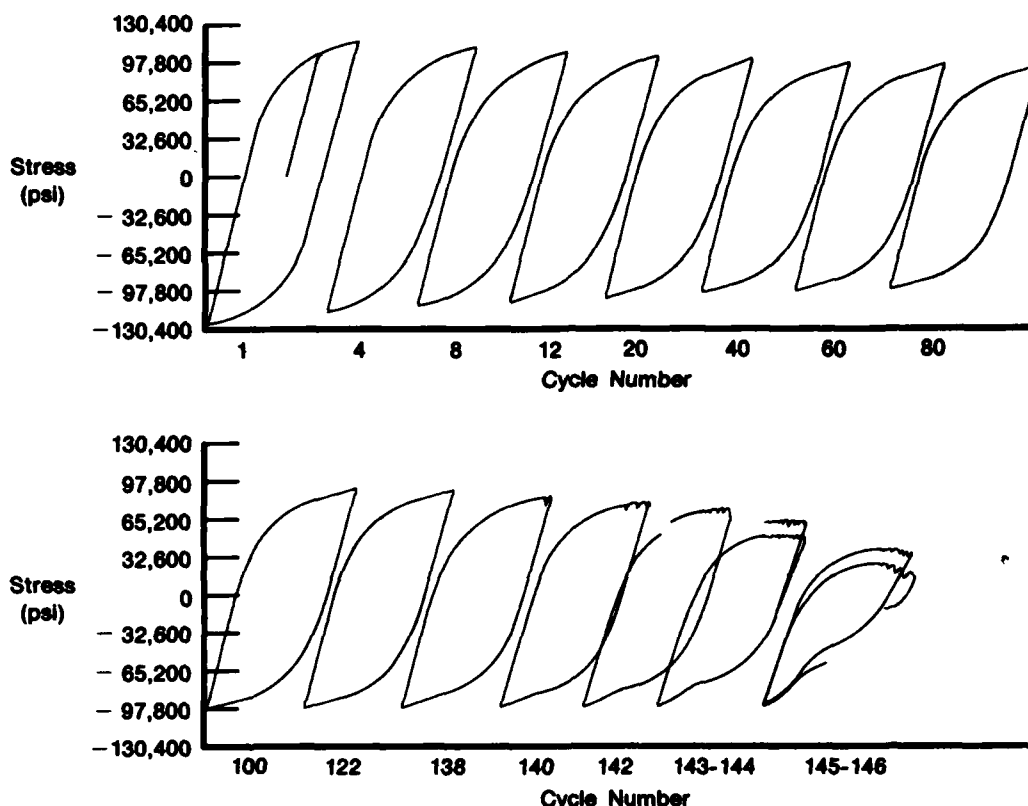
FD 268873

Figure 2-4.   *Cyclic Strain Controlled Hysteresis Loops at ± 1.0 Percent Strain Amplitude.*
Loops Were Carried Out at a Strain Rate of $\varepsilon = 5.3 \times 10^{-3}$ Per Second.
Loops Carried Out at $\varepsilon = 5.33 \times 10^{-4}$ Per Second Showed No Discernible
Difference to the Loops Shown Above

The rate insensitivity displayed by INCO 718 at 1200°F (649°C) in the strain rate region
around $\varepsilon = 10^{-4}$ per second precludes the use of tensile and hysteresis loop data to obtain the
strain rate material constants in the unified viscoplastic formulation detailed in Appendix B.
Strain rate material constants were obtained from a combination of the tensile/hysteresis loop
data at high strain rates (10^{-4} to 10^{-3} per second) and secondary creep data at low strain rates
(10^{-6} to 10^{-10} per second).

A power law expression [7] for the inelastic strain rate in terms of the applied stress, σ, and
equilibrium stress, Ω, was first fitted to the creep and hysteresis data. When fitting unified
viscoplastic theories to test data, the usual procedure is to assume that the functional form of the
inelastic strain rate is correct, and that any deviation of the test data from the assumed
functional form is due to thermal recovery. In this manner the constants for both rate effects and
thermal recovery can be determined from the test data.

A reasonable correlation of stress versus strain rate was achieved with the power law at low
to intermediate strain rates providing thermal recovery was taken into account. However, the
power law may be expected to hold only over a relatively small strain rate range, and the stresses
at high strain rates tend to be overestimated with a power law expression. This was clearly
evident in the predicted stress results for strain rates of 5.3×10^{-4} per second and 5.3×10^{-3} per

2-6

second used in the hysteresis loop testing. To obtain a better overall correlation of stress versus strain rate, it was decided to use an exponential law for the inelastic strain rate in place of the power law. This provided a much better fit to the experimental data at all strain rates without including thermal recovery effects. Thermal recovery is present at 1200°F (649°C), but to derive the current set of material constants, thermal recovery has been neglected. Table 2-1 shows the correlation between experiment and theory using the exponential law given in Appendix B.

Table 2-1. Stress vs Strain Rate With Exponential Law

ε (Per Second)	σ (psi, Test)	σ (psi, Theory)
5.3 E-3	172000 (Extrapolated)	177536
5.3 E-4	—	164492
6.88 E-6	140000	140000
8.22 E-7	130000	127971
1.52 E-7	120000	118406
3.66 E-8	110000	110435
5.67 E-9	100000	100000
3.65 E-10	80000	86377

INCO 718 displays cyclic softening at 1200°F (649°C). The softening can be seen in Figures 2-2, 2-3, and 2-4 from the decrease in the stress amplitude of the hysteresis loops as cycling proceeds under constant strain amplitude. It can also be observed in the increase in the width of the hysteresis loops under constant stress amplitude in the fatigue tests. This cyclic softening can be modeled with the viscoplastic formulation at small cyclic strain amplitudes by allowing the drag stress, K, to decrease with cumulative inelastic strain. In the finite element calculations the drag stress was assumed to be constant and cyclic softening was not permitted. Material constants for the cyclic softening case and for the noncyclic softening case used in the finite element calculations are listed in Appendix B.

Figure 2-5 shows the predicted steady state hysteresis loops for the case in which the drag stress is assumed to have a constant value. The hysteresis loops are executed between ±1.5 percent strain limits at strain rates corresponding to values in Table 2-1. Figure 2-6 shows the predicted effect of creep damage on the hysteresis loops shown in Figure 2-5. The loops in Figure 2-6 represent the theoretical hysteresis response on the second cycle. Little creep damage is apparent in the second cycle at high strain rates. However, at low strain rates the effect of creep damage is prevalent. Figures 2-7 and 2-8 show the predicted cyclic softening of a hysteresis loop executed at one cycle per minute (cpm) between ±0.8 percent strain limits.

Tertiary creep and creep damage accumulation have been included in the constitutive formulation by using Chaboche's continuum creep damage model [8]. Details are given in Appendix C. Experimental results of creep rupture time and creep rupture strain as a function of stress level are given in Table 2-2.

Table 2-2.   Creep Rupture Details of INCO 718 at 1200°F (649°C)
             Obtained in Present Contract

| Stress (ksi) | Strain on Loading | | Rupture Time (hr) | Final Elongation (%) | Reduction in Area (%) |
	Elastic (%)	Inelastic (%)			
140	0.508	0.639	1.4	8.2	12.6
135	0.610	0.607	2.0	9.0	14.2
130	0.251	0.151	6.9	7.4	12.2
120	0.279	0.056	25.5	10.5	16.2
110	0.292	0.006	56.7	8.0	13.2
100	0.286	0.0	281.1	13.4	41.9
80	0.277	0.0	Discontinued after 358 hr		

Further creep rupture results obtained from data generated by Domas, Sharpe, Ward, and Yau [6], and Thakker and Cowles [9] are given in Tables 2-3 and 2-4.

Table 2-3.   Creep Rupture Details of INCO 718 at 1200°F
             (649°C) Obtained by Domas, Sharpe, Ward,
             and Yau

Stress (ksi)	Rupture Time (hr)	Average Standard* Rupture Time (hr)
120	26	15
110	92	50
100	131	160
80	1583	1600

*C50TF6 Specification

Table 2-4.   Creep Rupture Details of INCO 718 at 1200°F (649°C) Obtained
             by Thakker and Cowles

| Stress (ksi) | Strain on Loading | | Rupture Time (hr) | Final Elongation (%) | Reduction in Area (%) |
	Elastic (%)	Inelastic (%)			
120	0.597	0.060	20.1	13.1	15.9
110	0.581	0.012	48.3	14.8	52.3
105	0.476	0.009	116.0	23.7	56.8
90	0.450	0.005	494.8	28.0	61.3

Figures 2-9 through 2-13 compare the experimental and theoretical creep response at stress levels of 100, 110, 120, 130, and 140 ksi. In general, the theoretical formulation overestimates the amount of primary creep and displays less tertiary creep in the early parts of the creep tests compared with experiment. The amounts of primary creep could be reduced towards the experimental levels by increasing the constants n_2 and n_3 which control the growth of the equilibrium stress state variable Ω_{ij}. Table 2-5 displays the computed value of k in Chaboche's creep rupture model compared with the value estimated from the test results. Table 2-6 compares the experimental and theoretical creep rupture times.

240,000

ε̇ (Per Second)
5.3 × 10⁻³
5.3 × 10⁻⁴
6.88 × 10⁻⁶
8.22 × 10⁻⁷
1.52 × 10⁻⁷
3.66 × 10⁻⁸
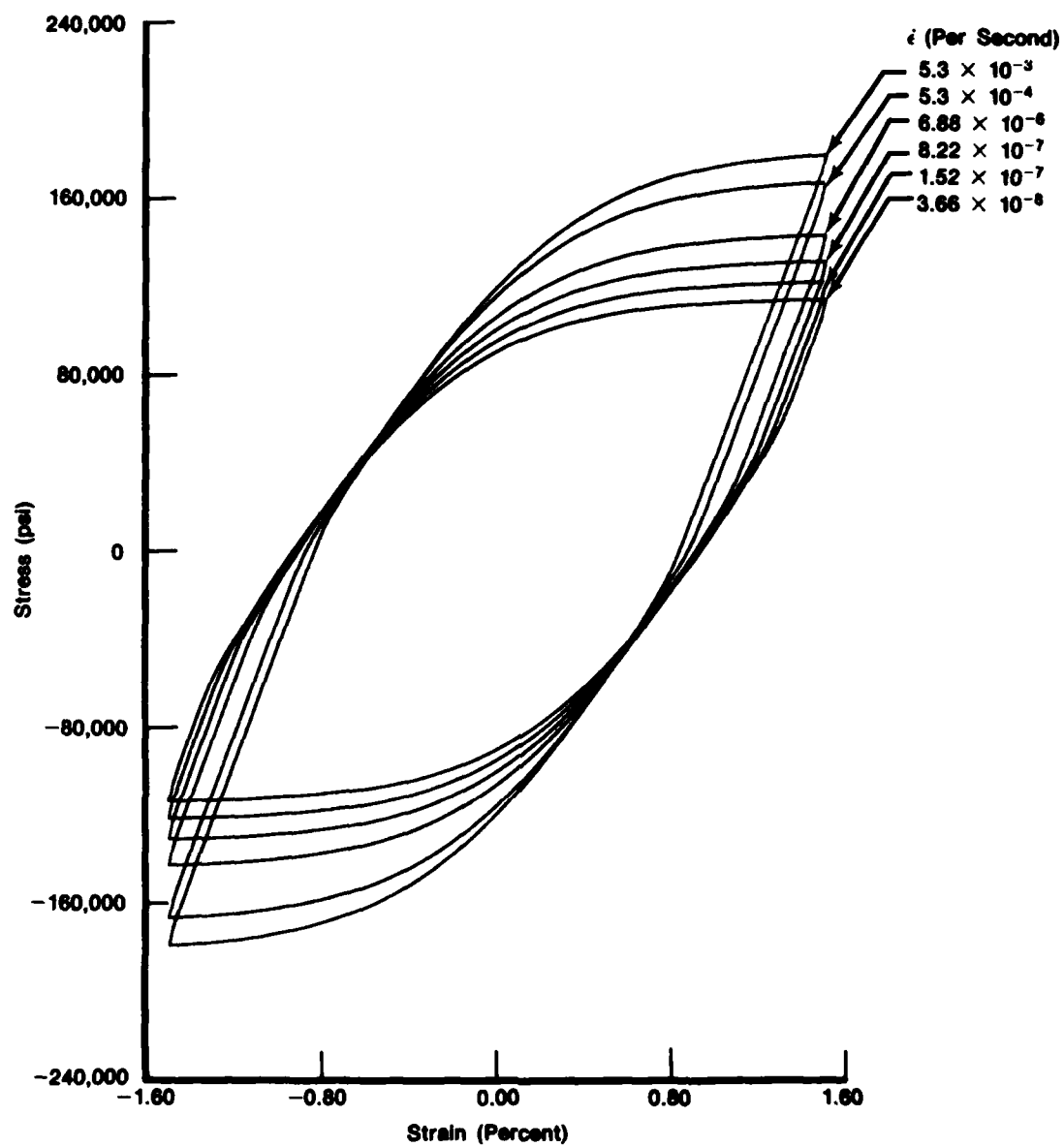
FD 268874

Figure 2-5. Computed Variation of Steady-State Hysteresis Loop With Strain Rate Between ±1.5 Percent Strain Limits

2-9

240,000

160,000

80,000

Stress (psi)

0

−80,000

−160,000

−240,000

$\dot{\epsilon}$ (Per Second)

5.3 × 10⁻³

5.3 × 10⁻⁴

6.86 × 10⁻⁶

8.22 × 10⁻⁷

1.52 × 10⁻⁷

3.66 × 10⁻⁸

−1.60   −0.80   0.00   0.80   1.60

Strain (Percent)
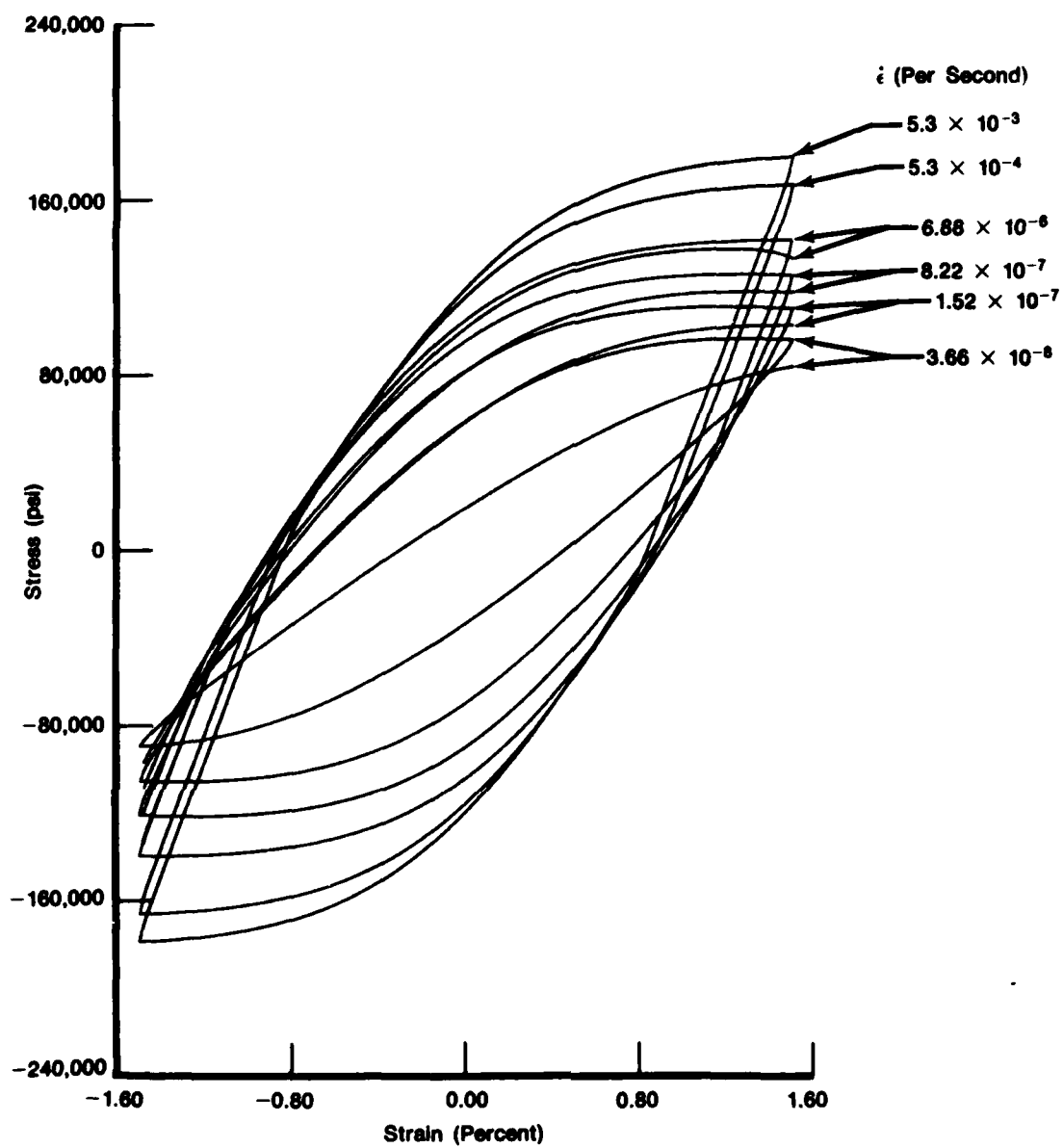
Figure 2-6. Effect of Creep Damage on the Second Cycle Hysteresis Loops
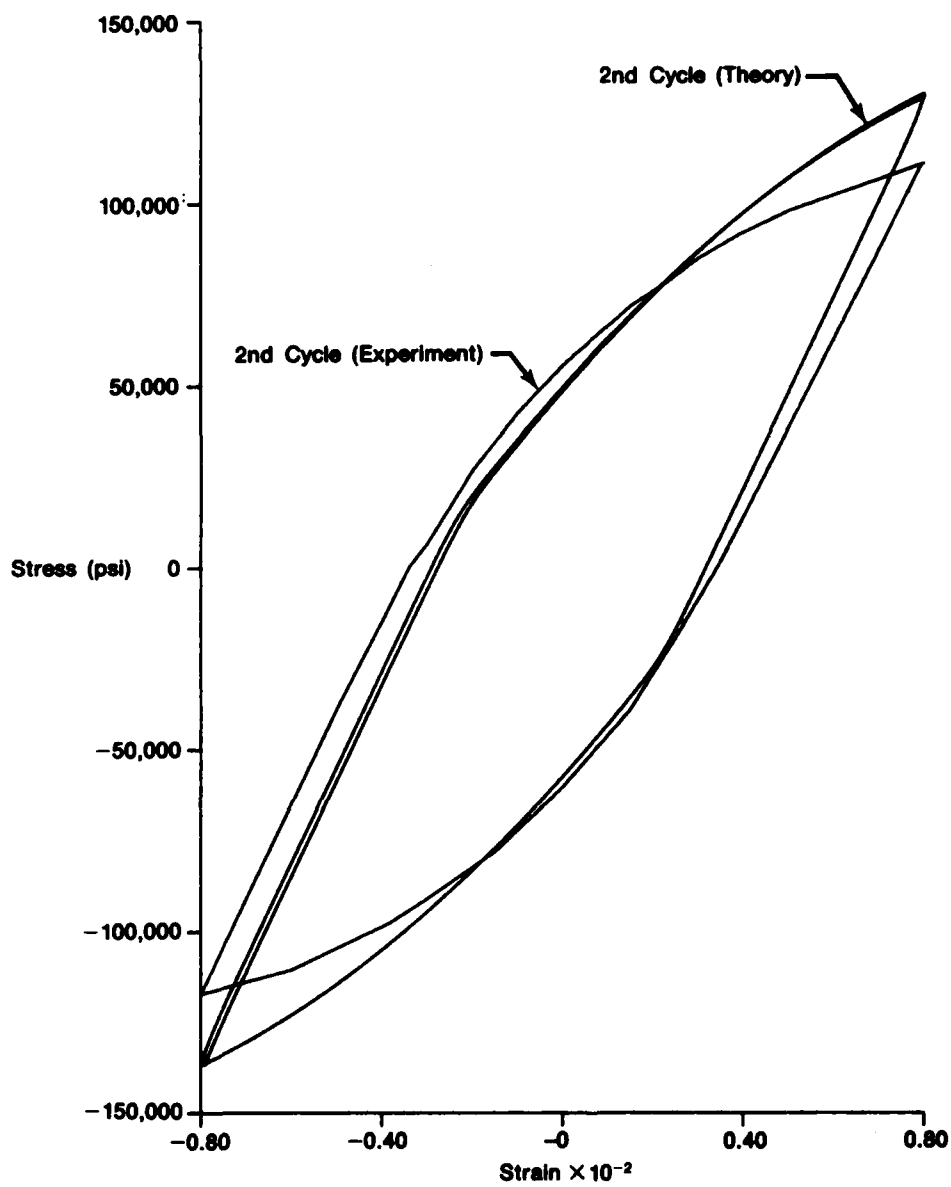
FD 271666

Figure 2-7. Predicted Cyclic Softening at 1 cpm Between ±0.8% Strain Limits for 2nd Cycle

2-11

150,000
100,000
50,000
0
-50,000
-100,000
-150,000

40th Cycle (Theory)

2nd Cycle (Experiment)

Stress (psi)

-0.80   -0.40   0   0.40   0.80

Strain ×10⁻²
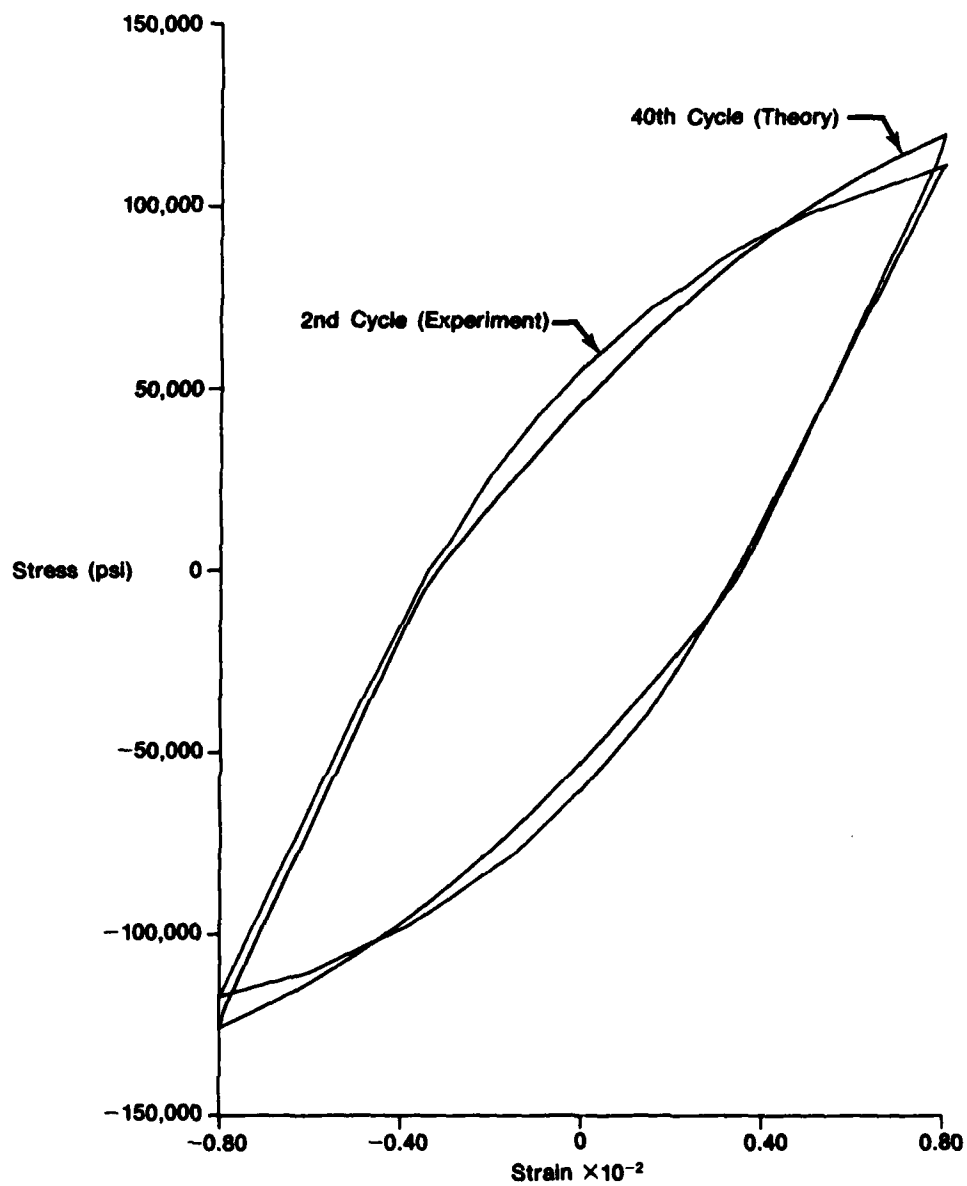
FD 271667

Figure 2-8. Predicted Cyclic Softening at 1 cpm Between ±0.8% Strain Limits for 40th Cycle

2-12
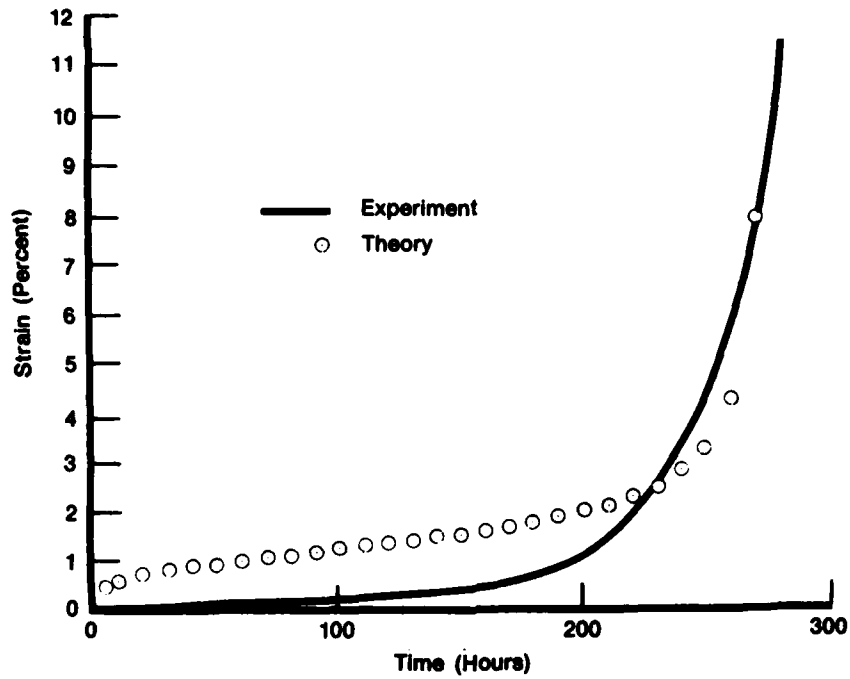
FD 258186A

Figure 2-9. Comparison of Experimental and Theoretical Creep Response at 100 ksi
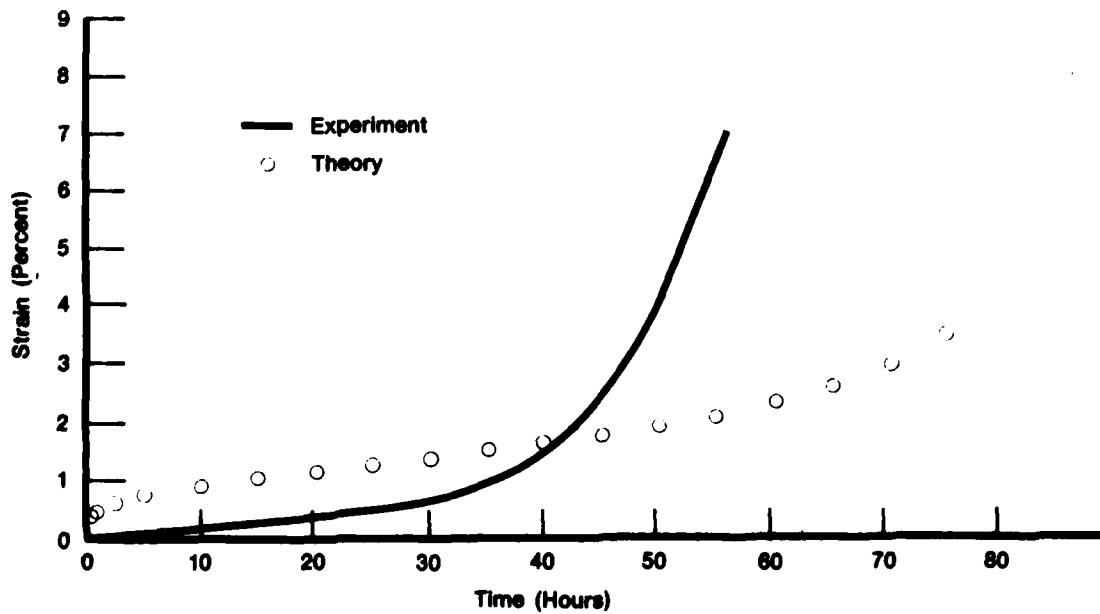
FD 258187A

Figure 2-10. Comparison of Experimental and Theoretical Creep Response at 110 ksi
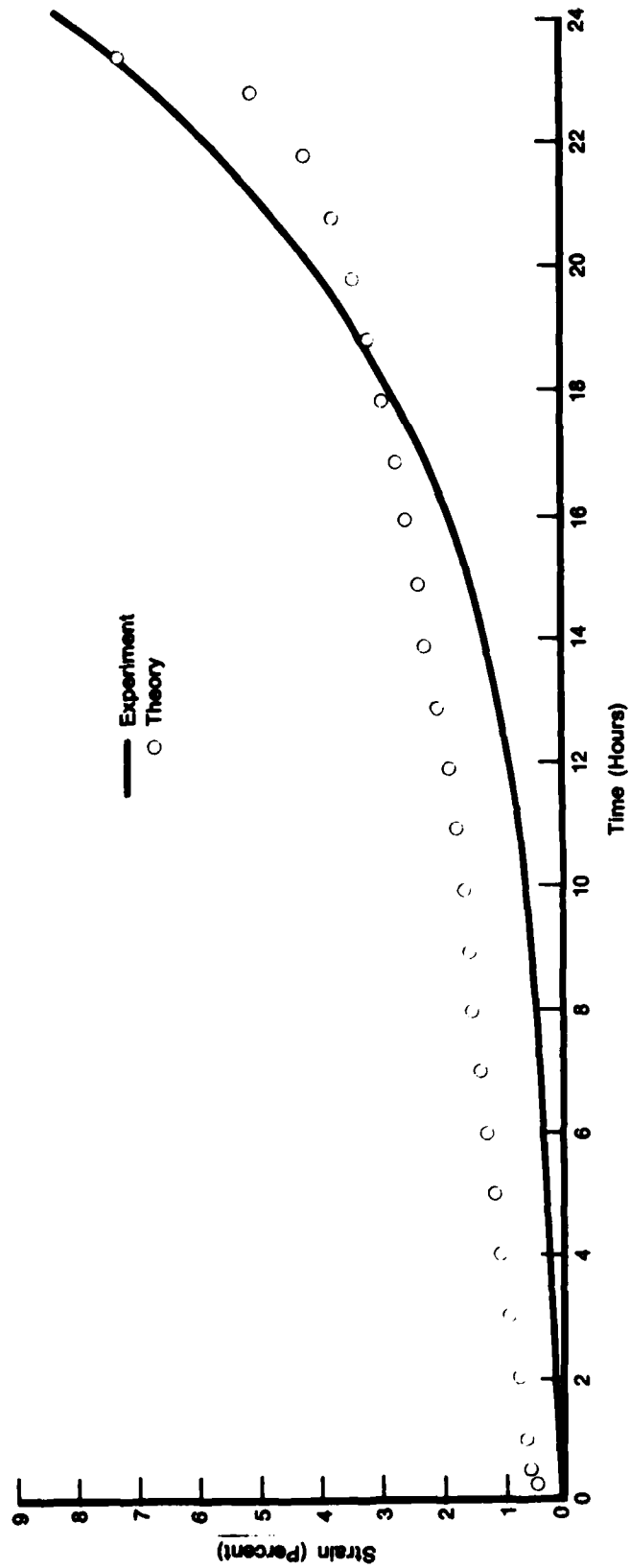
Figure 2-11. Comparison of Experimental and Theoretical Creep Response at 120 ksi

FD 258108A
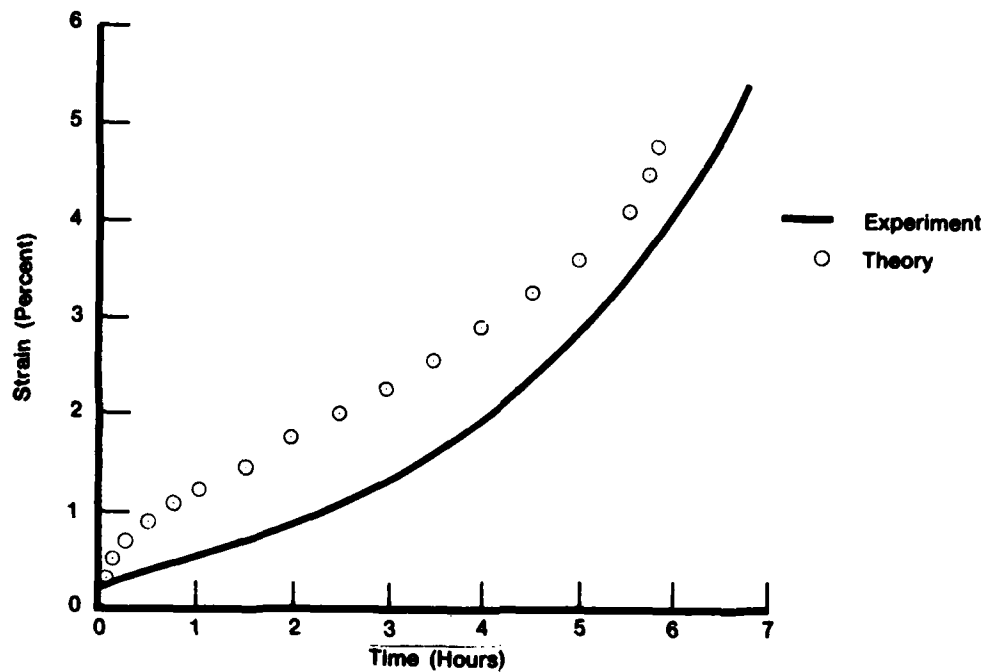
FD 258189A

Figure 2-12. *Comparison of Experimental and Theoretical Creep Response at 130 ksi*
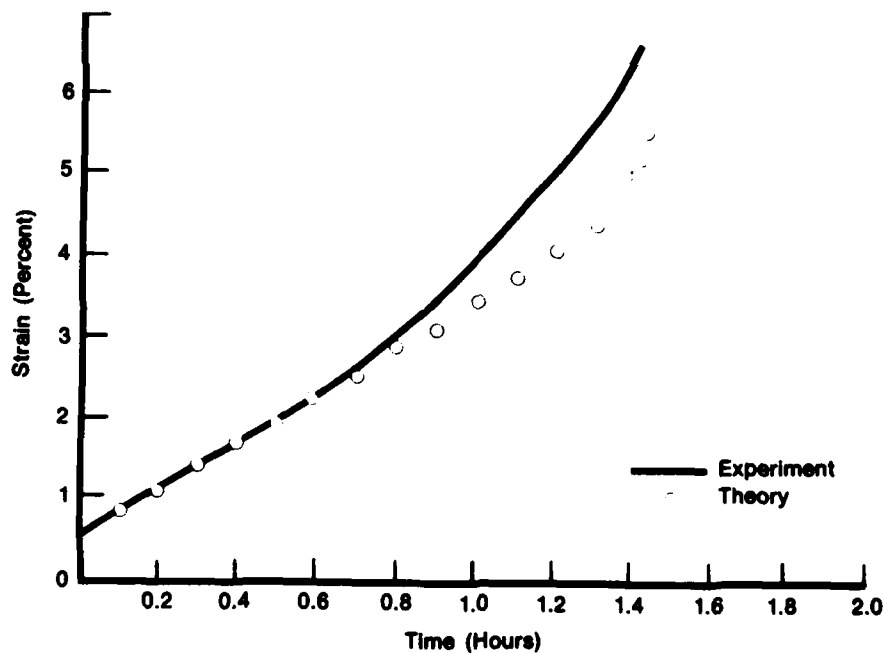
FD 258190A

Figure 2-13. *Comparison of Experimental and Theoretical Creep Response at 140 ksi*

2-15

Table 2-5. Comparison of Theoretical and Experimental Creep Rupture Exponents

Stress (psi)	k (Data)	$k = 1 + 1.011\,E\text{-}4e^{9.446\,E\text{-}5\,\sigma}$
100000	2.28	2.28
110000	3.64	4.29
120000	7.18	9.46
130000	17.06	22.77
140000	56.99	56.98

Table 2-6. Comparison of Theoretical and Experimental Creep Rupture Times

Stress (psi)	Rupture Time Experiment (sec)	Rupture Time (sec) from $t_r = [A\,\sigma^r\{k(\sigma)+1\}]^{-1}$
140000	5040	5041
130000	24840	21000
120000	91800	85015
110000	204120	315123
100000	1011960	1011687

$A = 2.394 \times 10^{-43}$, $r = 7.22$, $k(\sigma) = 1 + 1.011E\text{-}4e^{9.446E\text{-}5\,\sigma}$

The magnitude of the equilibrium stress state variable at the point of strain reversal was determined from a sequence of relaxation tests commencing at various stress levels on both the tension and compression unloading branches of the hysteresis loops. These loops were executed at a strain rate of 5.3×10^{-4} per second between strain limits of ± 0.8 percent. At points A, B, C, etc. in Figure 2-14 the strain was held at a constant value, and the stress relaxation was monitored as a function of time. The stress relaxations obtained from the unloading branch in tension at points A, B, C, etc. are shown in Figure 2-15. At levels above 80 ksi the stress relaxes in a normal fashion, while at levels below 80 ksi the initial stress relaxation is in an upward direction. Since the initial relaxation rate and its direction (upwards or downwards) depends on the difference between the stress and the equilibrium stress state variable, Figure 2-15 indicates a value of about 80 ksi for the value of the equilibrium stress at the point of tensile strain reversal. The stress relaxations obtained from the unloading branch in compression at points D, E, F, etc. are shown in Figure 2-16. This figure again indicates a value of about −80 ksi for the value of the equilibrium stress at the point of compressive strain reversal. For the unified viscoplastic formulation given in Appendix B, the saturation value of the equilibrium stress is given by the ratio of the material constants n_2/n_3. This ratio is given by $n_2/n_3 = 83,086$ psi.

Schematic Representation:
14 Points were Actually
Measured

Unloading Branch
in Compression

Unloading Branch in Tension

Note: Relaxation Curves Obtained
at Points A-F on the Unloading
Branches in Tension and Compression
are Shown in Figures 2-15 and 2-16.
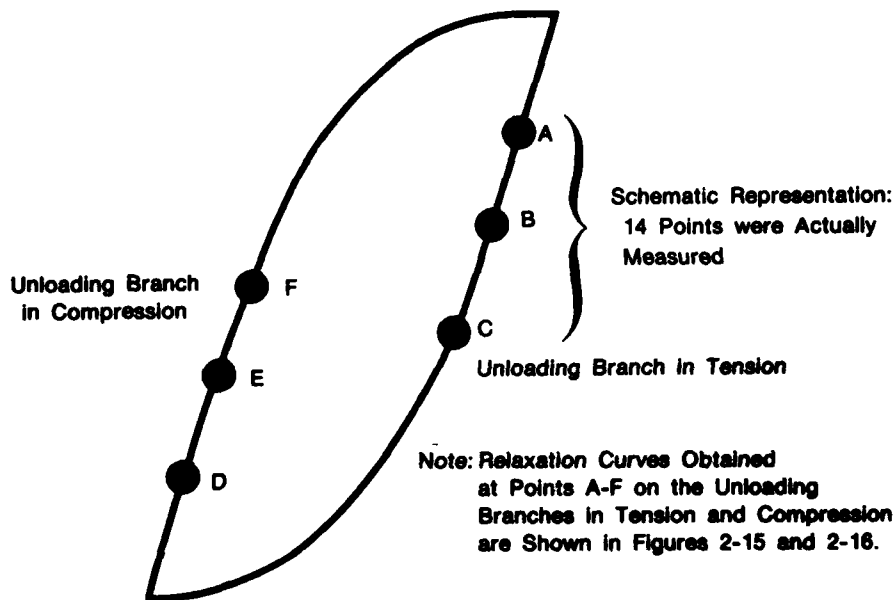
FD 258197A

Figure 2-14. Hysteresis Loop Is Executed at One Cycle Per Minute Between ±0.8 Percent Strain Limits
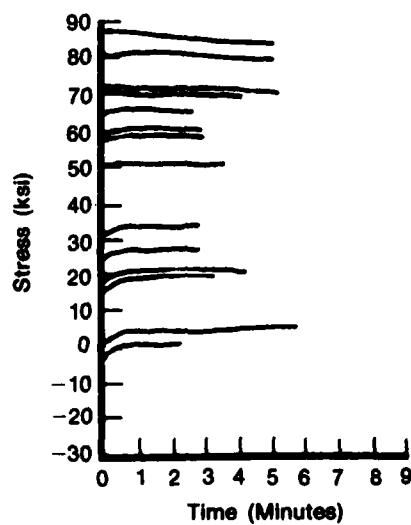
FD 258196A

Figure 2-15. Relaxation Curves Starting from Points on Tension Unloading Branch in Figure 2-14
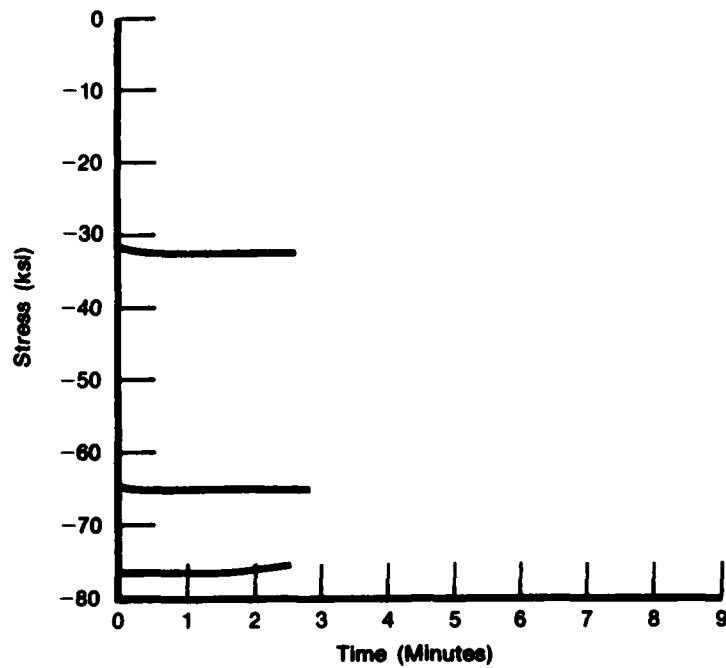
Figure 2-16. Relaxation Curves Starting from Points on Compression Unloading Branch in Figure 2-4

2.3 CREEP AND FATIGUE MODELING

A Kachanov type of continuum damage model has been proposed by Chaboche [8] which includes damage due to both creep and fatigue. The creep damage model is outlined in Appendix C and the fatigue damage model in Appendix D. These models have been incorporated into the unified viscoplastic constitutive formulation by replacing the stress tensor σ by an effective stress tensor $\sigma/(1 - D)$, where D is the continuum damage parameter which has the value $D = 0$ in the initial undamaged virgin material and which has the value $D = 1$ in the final ruptured state. The growth of the continuum damage D is assumed to be governed by the rate equation

$$\dot{D} = \dot{D}_c + \dot{D}_f,$$

where $\dot{D}_c$ is the rate of growth of creep damage with time governed by the creep damage model in Appendix C, and $\dot{D}_f$ is the rate of growth of fatigue damage with time due to fatigue cycling governed by the fatigue damage model in Appendix D.

Material constants for the creep damage model were determined from creep rupture tests on uniaxial specimens of INCO 718 at 1200°F (649°C). The specimens were given a standard heat treatment per specification AMS 5596C as follows:

> Solution anneal at 1750°F (854°C) for one hour. Air cool to below 932°F (500°C). Age at 1325°F (718°C) for eight hours. Furnace cool to 1150°F (621°C). Age at 1150°F (621°C) for a total time of 18 hours aging, cooling, and aging. Air cool to room temperature. The test material was furnished in the form of 0.5 in. (12.7 mm) thick flat plates having nominal dimensions 12 × 4 in. (305 × 102 mm).

Figure 2-17 shows a plot of log σ versus log t_R for the creep rupture tests performed in the present contract and for creep rupture data generated by Domas et al [6] and by Thakker and Cowles [9]. Values of the function, $k(\sigma)$, as a function of initial applied creep stress, σ, were determined by fitting the theoretical tertiary creep response shown in Figures 2-9 through 2-13 to the experimental tertiary creep data.

The rupture time, t_R, corresponding to an initial tensile stress level, σ, can be determined from the uniaxial form of the damage growth relation presented in Appendix C. This relationship may be written in the uniaxial form

$$\frac{dD_c}{dt} = \frac{A\sigma^r}{(1-D_c)^{k(\sigma)}} . \tag{1}$$

Integration between the limits $D_c = 0$ to $D_c = 1$ gives the creep rupture time in the form

$$t_R = \left[A\sigma^r \left\{ k(\sigma) + 1 \right\} \right]^{-1} . \tag{2}$$

A least squares fit to the three data sets is achieved with the values

$$A = 1.17 \times 10^{-38}, \quad r = 6.31, \quad k(\sigma) = 1 + (1.011 \times 10^{-4}) \exp (9.446 \times 10^{-5} \sigma).$$
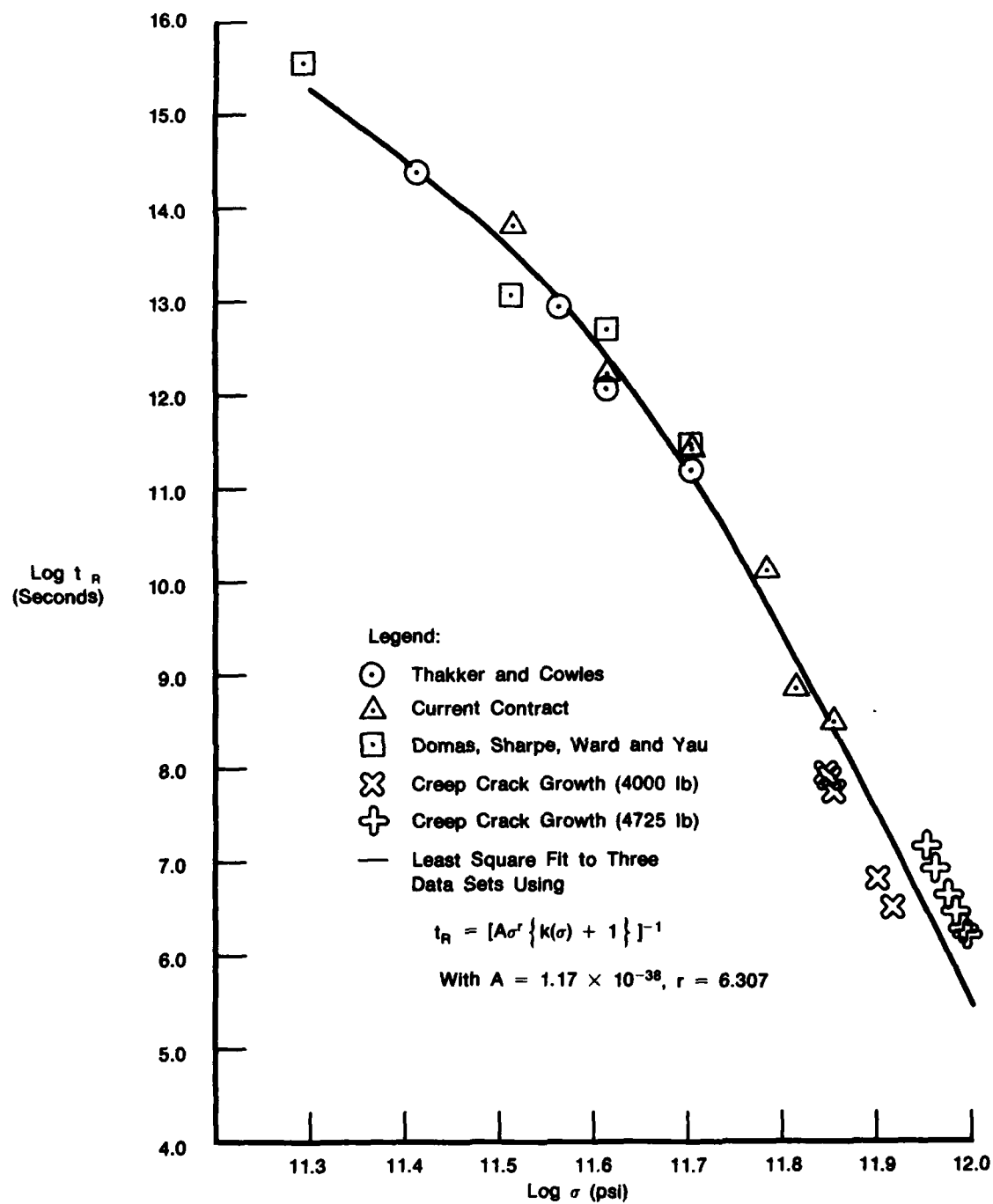
Figure 2-17. Experimental Creep Rupture Data and Least Square Theoretical Fit

FD 268876

This fit is shown as the solid line in Figure 2-17. For the data generated in the present contract a least square fit is achieved with the values

$$A = 2.394 \times 10^{-43}, \quad r = 7.22, \quad k(\sigma) = 1 + (1.011 \times 10^{-4}) \exp(9.446 \times 10^{-5} \sigma).$$

The three dimensional form of Chaboche's fatigue model, which includes mean stress effects, is given in Appendix D. This growth law may be written in the uniaxial form

$$\frac{dD_f}{dN} = \left[1 - (1 - D_f)^{\beta + 1}\right]^{\alpha} \left[\frac{\Delta\sigma}{M_o (1 - b \, \sigma_m)(1 - D_f)}\right]^{\beta} \tag{3}$$

where

$$\alpha = 1 - \frac{M_o^{\beta}}{C(\beta + 1)} (\Delta\sigma)^{\gamma - \beta}, \tag{4}$$

and M_o, C, β, γ are material constants. The quantities $\Delta\sigma$ and σ_m represent the cyclic stress amplitude and the cyclic mean stress, respectively.

Integration of this fatigue model from $N = 0$ ($D_f = 0$) to $N = N_f$ ($D_f = 1$) for a constant stress amplitude, $\Delta\sigma$, gives the number of cycles to failure in the form:

$$N_f = \frac{1}{(\beta + 1)(1 - \alpha)\left(\dfrac{\Delta\sigma}{M_o(1 - b\sigma_m)}\right)^{\beta}}. \tag{5}$$

Substitution of (4) into (5) then gives the cyclic failure relation

$$N_f = C(\Delta\sigma)^{-\gamma}(1 - b\sigma_m)^{\beta}. \tag{6}$$

From uniaxial fatigue tests carried out under constant stress amplitudes of ± 80, ± 85, ± 90, ± 95, ± 100, ± 110, and ± 120 ksi under zero mean stress, the least square values

$$C = 3.809 \times 10^{90}, \gamma = 16.625$$

are obtained. The constants β, M_o and b have the values

$$\beta = 9.14, M_o = 286{,}000, b = 5.99 \times 10^{-6}.$$

The cyclic softening exhibited by INCO 718 at 1200°F (649°C) may be seen by the increase in the width of the fatigue hysteresis loops in Figures 2-18 through 2-24. If the differential fatigue model is integrated under constant stress amplitude, $\Delta\sigma$, from $D_f = 0$ to $D_f = D$, the following relation is obtained:

$$\frac{N}{N_f} = [1 - (1 - D)^{\beta + 1}]^{1 - \alpha}. \tag{7}$$

Equations (5) and (7) may then be combined to yield the accumulation of the damage parameter D as a function of cycle number in the form

$$D = 1 - \left[1 - \left(\frac{N}{N_f}\right)^{(\beta + 1)\, N_f\, (\Delta\sigma/Mo)^\beta}\right]^{1/\beta + 1},$$

in which it is assumed that the mean stress, σ_m, is zero.

This equation shows that the damage parameter accumulates slowly with cycle number at the beginning of the fatigue test and accumulates rapidly towards the end of the test.
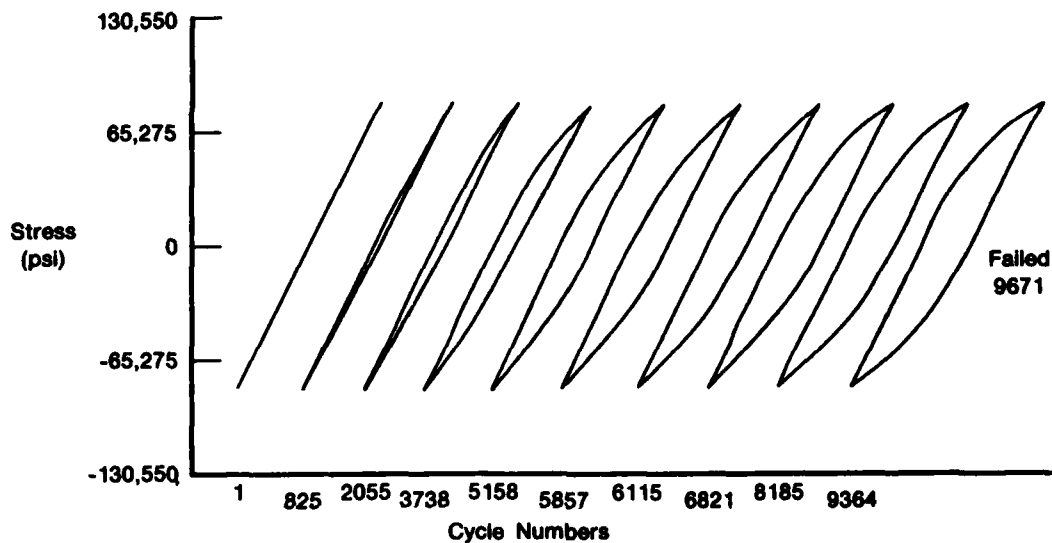
FD 268877

Figure 2-18.   Hysteresis Loops for INCO 718 at 1200°F (649°C) Under ±80 ksi Stress Amplitude Loading at 10 cpm

FD 288878
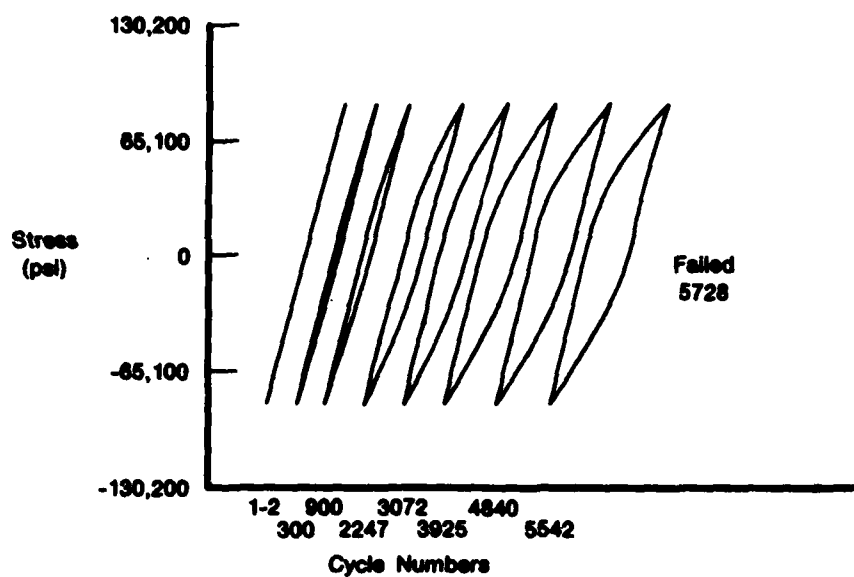
Figure 2-19. Hysteresis Loops for INCO 718 at 1200°F (649°C) Under ±85 ksi Stress
Amplitude Loading at 10 cpm
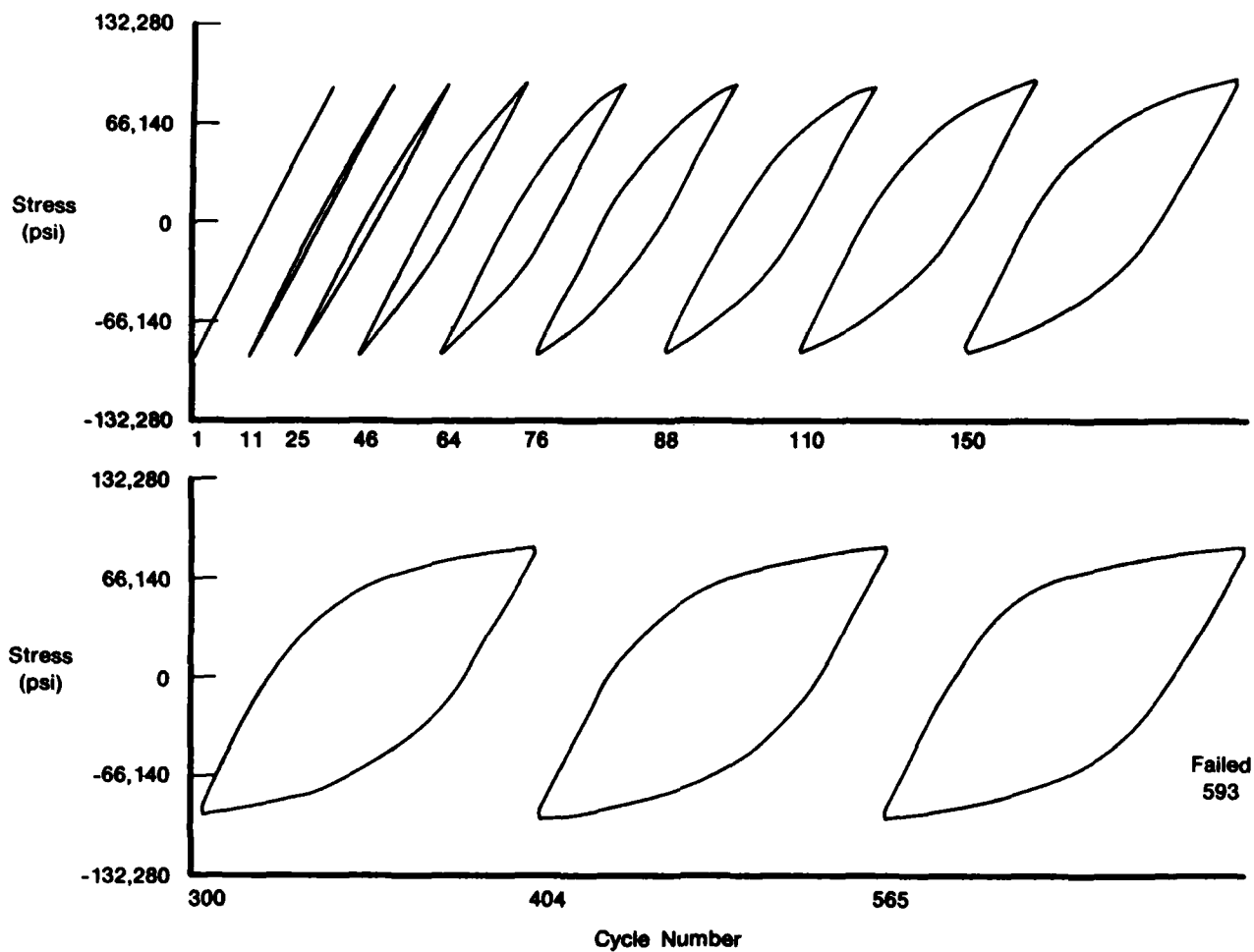
Figure 2-20. *Hysteresis Loops for INCO 718 at 1200°F (649°C) Under ±90 ksi Stress Amplitude Loading at 10 cpm*

FD 268879

2-24
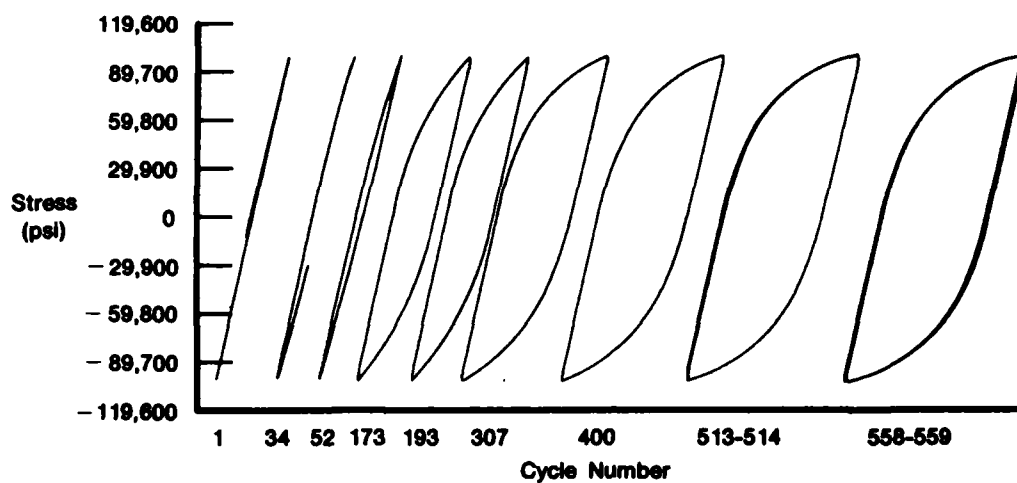
FD 268881

Figure 2-21. Hysteresis Loops for INCO 718 at 1200°F (649°C) Under ±100 ksi Stress Amplitude Loading at 10 cpm
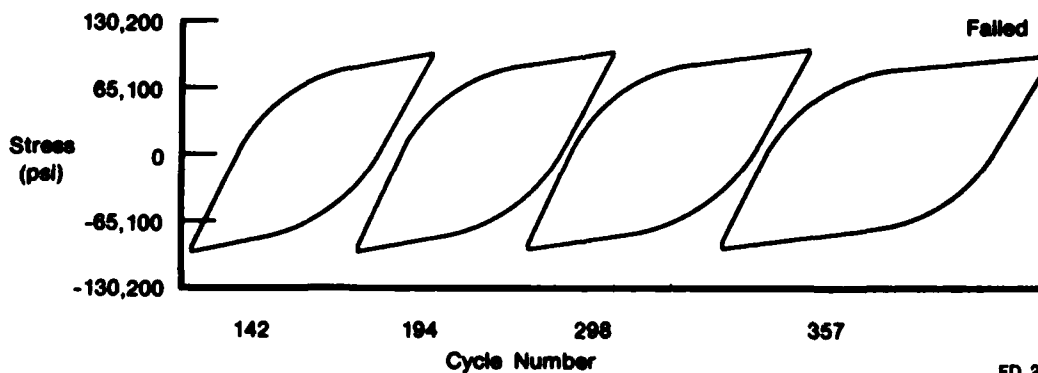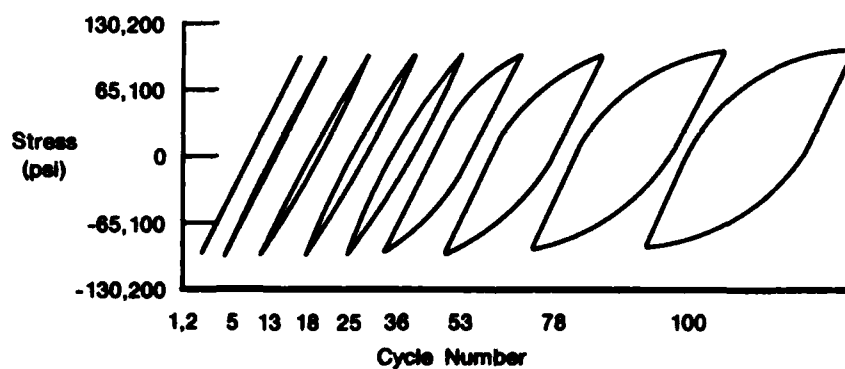
FD 268880

Figure 2 22. Hysteresis Loops for INCO 718 at 1200°F (649°C) Under ±95 ksi Stress Amplitude Loading at 10 cpm
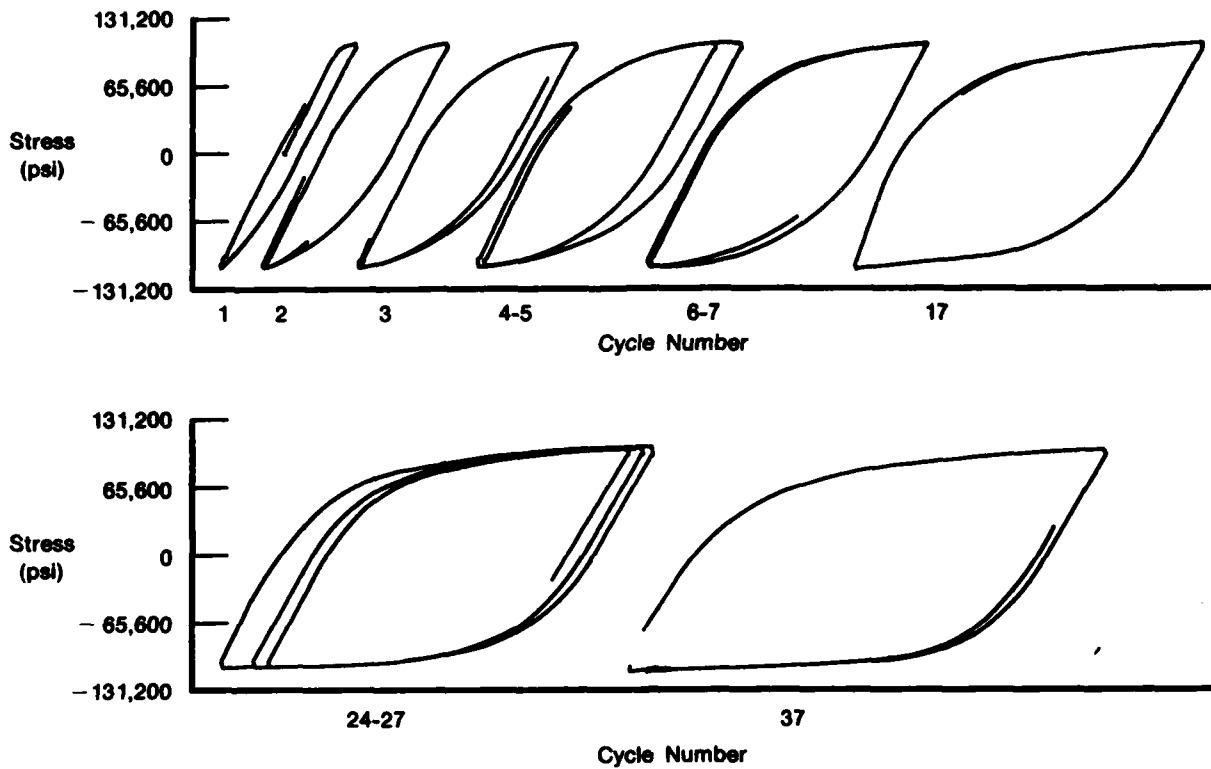
Figure 2-23. *Hysteresis Loops for INCO 718 at 1200°F (649°C) Under ±110 ksi Stress Amplitude Loading at 10 cpm*
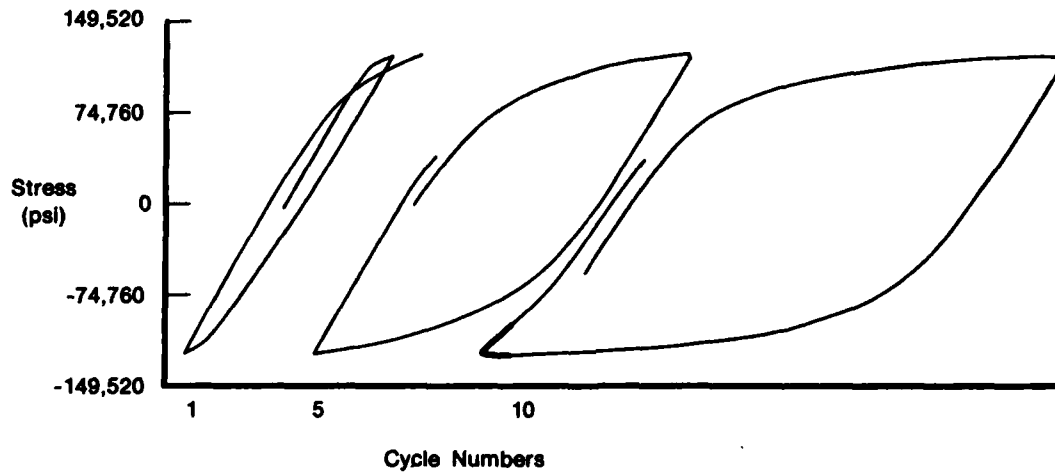
Figure 2-24. *Hysteresis Loops for INCO 718 at 1200°F (649°C) Under ±120 ksi Stress Amplitude Loading at 6.7 cpm*

2-26

Figure 2-25 shows a least square fit to the experimental Wohler curve for INCO 718 at 1200°F (649°C), while Table 2-7 compares the predicted least square values against the experimental results.
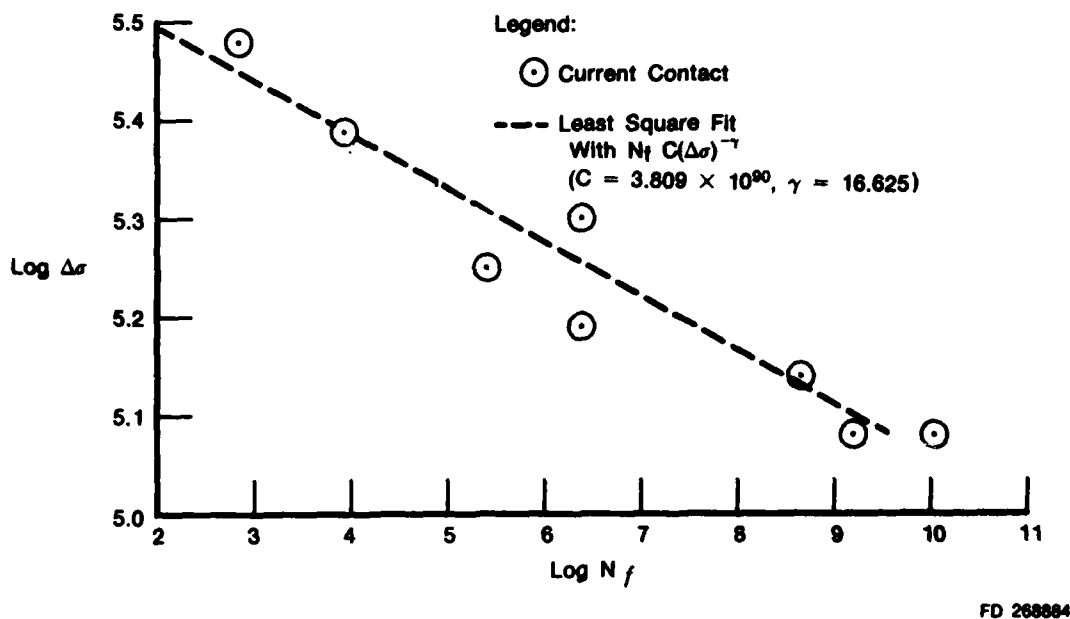
Figure 2-25. *Wohler Curve for INCO 718 at 1200°F (649°C)*

Table 2-7. *Comparison of Theoretical and Experimental Fatigue Failure Data (C = 3.809 × 10^{90} and γ = 16.625)*

Stress Range (ksi)		$N_f = C(\Delta\sigma)^{-\gamma}$	Experimental N_f
160	(±80)	11,542	9,671 and 22,826
170	(±85)	4,213	5,728
180	(±90)	1,629	593
190	(±95)	663	357
200	(±100)	283	578
220	(±110)	58	50
240	(±120)	14	17

The data presented in Figure 2-25 can be enclosed in a scatterband by taking the constant C to have the values $C = 7.6 \times 10^{90}$ and $C = 1.9 \times 10^{90}$, respectively.

To obtain the accumulation of damage parameter with cycle number on an experimental basis, the following procedure was used. The unified viscoplastic constitutive formulation with the damage set equal to zero was integrated over two cycles under fully reversed strain controlled conditions at a strain rate of $\varepsilon = 5.3 \times 10^{-3}$ per second. The computed stress amplitude, $\Delta\sigma$, was then determined as a function of the inelastic width of the loop, Δc^*, for various strain amplitudes and fitted to obtain the following power law relationship:

$$\Delta c^* = \left(\frac{\Delta\sigma}{K_c}\right)^{m_c},$$

(9)

2-27

where $K_c = 902,757$ and $m_c = 4.25$. This cyclic stress-strain relation does not include the accumulation of damage. With damage included, equation (9) may be written in the form:

$$\Delta c = \left(\frac{\Delta \sigma}{K_c(1 - D_f)} \right)^{m_c} .$$

(10)

These relations allow the damage parameter D_f to be written as

$$D_f = 1 - \left(\frac{\Delta c^*}{\Delta c} \right)^{1/m_c} ,$$

(11)

where Δc^* is the width of the hysteresis loop when the damage parameter D_f is zero, and Δc is the width of the hysteresis loop with damage included. Figure 2-21 shows the increase in the width of the hysteresis loop in a test carried out at $\Delta \sigma = 200$ ksi (± 100 ksi) at 1200°F (649°C). The values of Δc^* found from the first cycle can then be divided by the width of the loop, Δc, at the Nth cycle. Equation (11) then allows a plot of D_f versus N to be constructed. Plots of D_f versus N found in this manner are displayed in Figures 2-26 through 2-28.
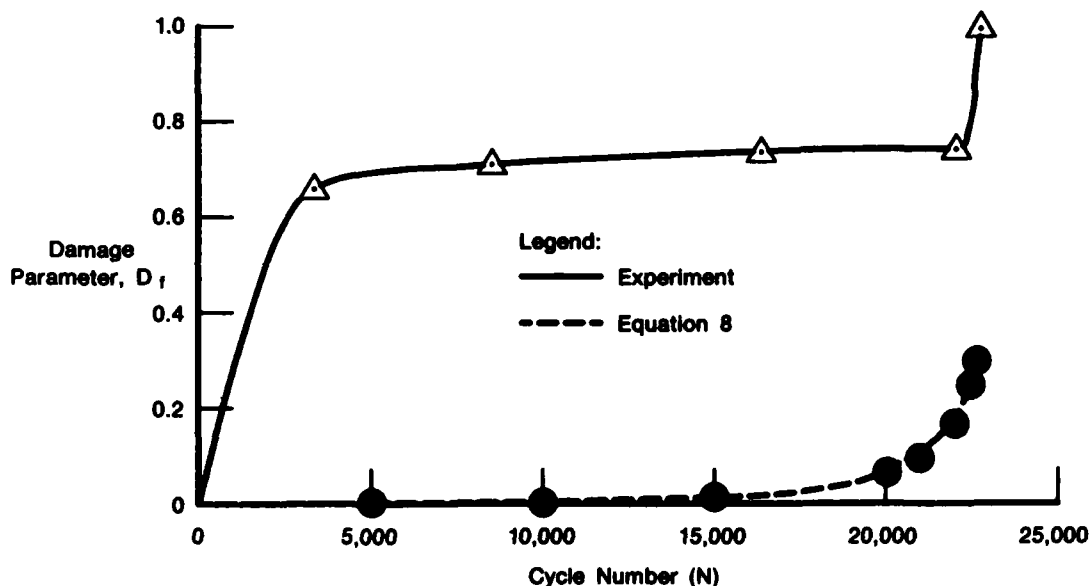
FD 268885

Figure 2-26. Accumulation of Damage Parameter With Cycle Number at Constant Stress Amplitude $\Delta \sigma = 160$ ksi (+/−80 ksi)

In the construction of these figures it has been implied that K_c in equation (9) was constant, and that Δc increased due to an increase in D_f. But the tests shown in Figures 2-2 through 2-4 under strain controlled conditions show that INCO 718 cyclically softens at 1200°F (649°C), implying that K_c decreases with cycle number. This suggests the following interpretation of Figures 2-26 through 2-28. Over the first half of the fatigue tests, the apparent rise of the damage parameter and its subsequent saturation to an apparent plateau value of $D_f \approx 0.7$ may be attributed to cyclic softening in which the actual damage parameter is very small.

2-28
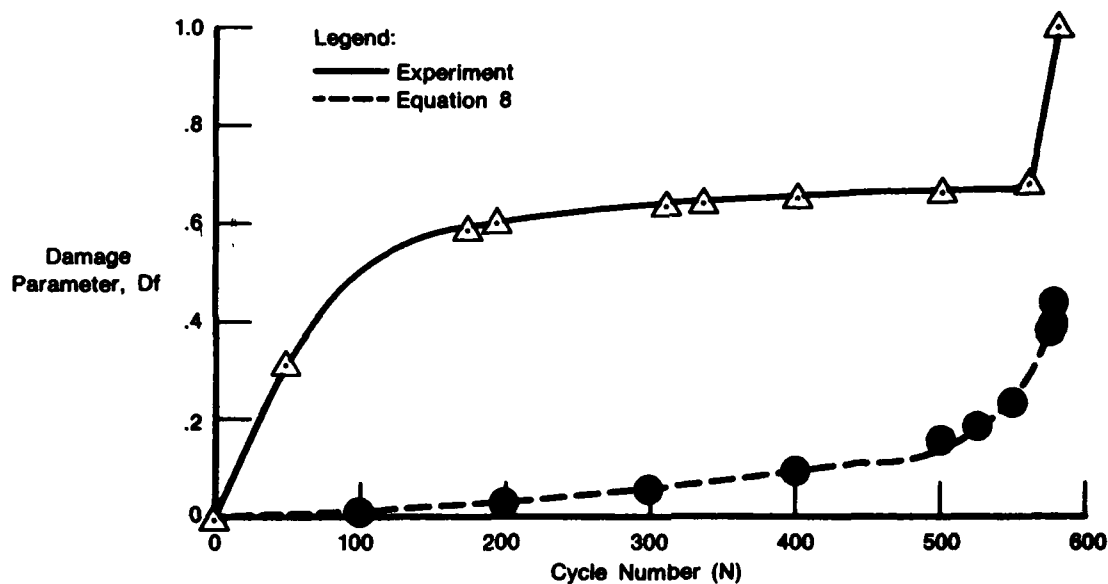
FD 268886

Figure 2-27. Accumulation of Damage Parameter With Cycle Number at Constant Stress Amplitude $\Delta\sigma = 200$ ksi (+/−100 ksi)
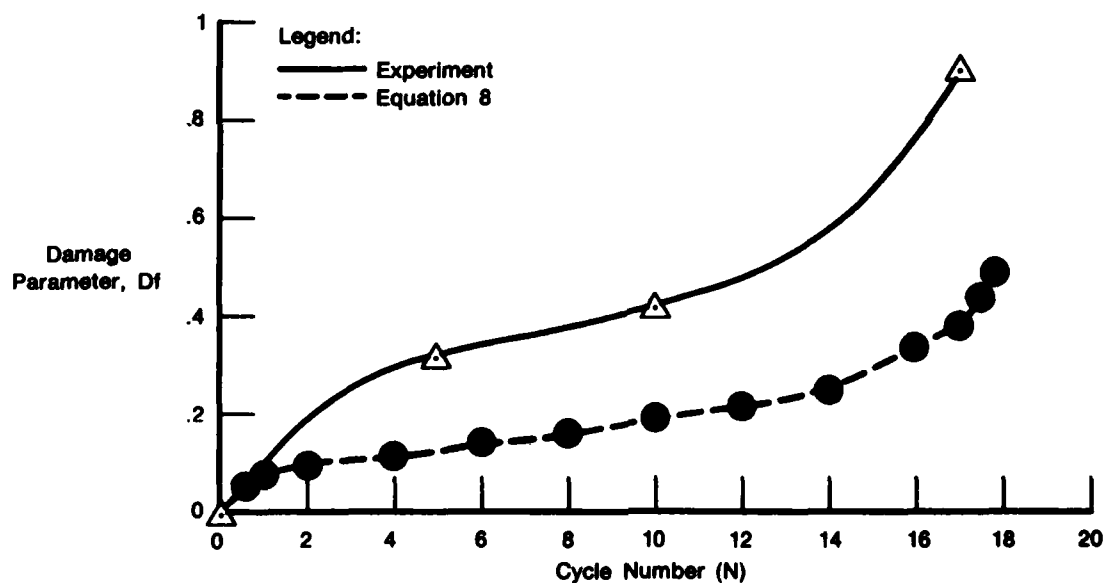
FD 268887

Figure 2-28. Accumulation of Damage Parameter With Cycle Number at Constant Stress Amplitude $\Delta\sigma = 240$ ksi (+/−120 ksi)

The apparent rise of D_f is due to the decrease in K_c from cyclic softening. As K_c saturates to a reduced value under cycling and the actual damage parameter is still small, a plateau is reached. Finally, as D_f increases rapidly at the end of the test, the curve rises steeply. Most of the increase in the width of the loops in Figures 2-2 through 2-4 with increasing cycle number is therefore attributed to cyclic softening and not to an increase in the damage parameter.

2-29

2.4 FINITE ELEMENT MODELING

2.4.1 FORTRAN Code

The unified viscoplastic constitutive formulation including Chaboche's continuum creep/fatigue model outlined in Appendices B, C, and D was incorporated into a FORTRAN subroutine of the ABAQUS [1] general purpose nonlinear finite element program. A listing of the FORTRAN subroutine has been supplied to the Air Force.

The ABAQUS program solves the nonlinear finite element equilibrium equations by a Newton-Raphson iterative method. For quasistatic loading conditions the finite element equilibrium equations are solved in the form:

$$\Sigma (\int B^T J B \, dV) c^k = P(t + \Delta t) - \Sigma \int B^T (\sigma(t) + \Delta\sigma(\Delta u^k)) dV, \tag{12}$$

$$\Delta u^{k+1} = \Delta u^k + c^k. \tag{13}$$

In these equations the matrix B transforms incremental nodal displacements Δu to incremental strains according to the relationship

$$\Delta\epsilon = B \, \Delta u. \tag{14}$$

The stress increment $\Delta\sigma$ for the unified viscoplastic constitutive formulation is a function of the strain increment $\Delta\epsilon$, and is therefore a function of the nodal displacement increments Δu via equation (14). Equation (12) provides the correction c^k to the kth iteration for the displacement increment Δu^k.

In order to implement the Newton-Raphson iterative method for solving the finite element equilibrium equations, it is necessary to provide the Jacobian matrix J in equation (12). This matrix is determined from the relationship

$$J = \left(\frac{\partial \sigma}{\partial \epsilon} \right)_{t + \Delta t}. \tag{15}$$

Since the unified viscoplastic formulations result in rather stiff differential equations, the stress increment $\Delta\sigma$ resulting from Δu must be determined by a subincrement method. The simplest method, and the one used in the present contract, is to split the finite element increment into a number of equally sized subincrements and to integrate the viscoplastic equations over each subincrement with an Euler forward difference method. This can result in an unstable integration operator if the subincrement size is too large. In the FORTRAN subroutine the inelastic strain rate is determined by the forward difference representation of equation (1) of Appendix B. If the magnitude of the argument of the exponential factor in equation (1) exceeds 30 in any subincrement, the integration procedure is stopped. The number of subincrements is then tripled and the subincrement integration procedure is restarted from the beginning. This procedure is repeated until no subincrement produces an exponential argument magnitude greater than 30.

Since the Jacobian matrix J cannot be obtained in algebraic form when a subincremental integration procedure is used, it is necessary to obtain this matrix numerically. A numerical Jacobian matrix is computed in the following manner. First, the viscoplastic constitutive subroutine is entered to determine the stress increments $\Delta\sigma_{xx}$, $\Delta\sigma_{yy}$, $\Delta\sigma_{xy}$ corresponding to the

strain increments $\Delta\varepsilon_{xx}$, $\Delta\varepsilon_{yy}$, $\Delta\varepsilon_{xy}$. Let $\Delta\sigma_{xx}^{xx}$, $\Delta\sigma_{yy}^{xx}$, $\Delta\sigma_{xy}^{xx}$ be the stress increments corresponding to the perturbed strain increments $\Delta\varepsilon_{xx} + 0.01\,\Delta\varepsilon_{xx}$, $\Delta\varepsilon_{yy}$, $\Delta\varepsilon_{xy}$; let $\Delta\sigma_{xx}^{yy}$, $\Delta\sigma_{yy}^{yy}$, $\Delta\sigma_{xy}^{yy}$ correspond to the perturbed strain increments $\Delta\varepsilon_{xx}$, $\Delta\varepsilon_{yy} + 0.01\,\Delta\varepsilon_{yy}$, $\Delta\varepsilon_{xy}$; and let $\Delta\sigma_{xx}^{xy}$, $\Delta\sigma_{yy}^{xy}$, $\Delta\sigma_{xy}^{xy}$ correspond to the perturbed strain increments $\Delta\varepsilon_{xx}$, $\Delta\varepsilon_{yy}$, $\Delta\varepsilon_{xy} + 0.01\,\Delta\varepsilon_{xy}$. The numerical plane stress Jacobian is then determined from the matrix relation:

$$
J = \begin{bmatrix}
\dfrac{\Delta\sigma_{xx}^{xx} - \Delta\sigma_{xx}}{0.01\Delta\epsilon_{xx}} & \dfrac{\Delta\sigma_{xx}^{yy} - \Delta\sigma_{xx}}{0.01\Delta\epsilon_{yy}} & \dfrac{\Delta\sigma_{xx}^{xy} - \Delta\sigma_{xx}}{2(0.01\Delta\epsilon_{xy})} \\[2em]
 & \dfrac{\Delta\sigma_{yy}^{yy} - \Delta\sigma_{yy}}{0.01\,\Delta\epsilon_{yy}} & \dfrac{\Delta\sigma_{yy}^{xy} - \Delta\sigma_{yy}}{2(0.01\Delta\epsilon_{xy})} \\[2em]
\text{Symmetric} & & \dfrac{\Delta\sigma_{xy}^{xy} - \Delta\sigma_{xy}}{2(0.01\Delta\epsilon_{xy})}
\end{bmatrix} \cdot \tag{16}
$$

Thus, the plane stress Jacobian matrix requires four calls to the viscoplastic constitutive subroutine at each Gaussian integration point in the structural model. One call is required to obtain the unperturbed stress increment $\Delta\sigma$, while three additional calls are required for each perturbed strain increment.

It is necessary to use the same number of subincrements in each of the four calls to the viscoplastic constitutive subroutine. Otherwise, the Jacobian matrix will contain components resulting from the operation $\partial\sigma/\partial$ (change in number of subincrements). For this reason it was not considered worthwhile to change the size of the subincrements by means of some self-adaptive error detecting method during the finite element integration step, since the size of each subincrement would have to be stored in order to use the same subincrement breakup in each of the perturbed strain increment calls to the constitutive subroutine. The simple procedure of using enough subincrements to prevent the magnitude of the exponential argument from exceeding the value of 30 was therefore adopted.

In order to determine the number of subincrements to be used in the finite element integration step, the following empirical procedure was adopted. Let $\Delta\varepsilon_{max}$ denote the largest absolute value of either $\Delta\varepsilon_{xx}$, $\Delta\varepsilon_{yy}$ or $\Delta\varepsilon_{xy}$ for the case of plane stress. Numerical studies have shown that the forward difference integration procedure is generally stable provided the strain increment does not exceed the value of 10^{-4}. The number of subincrements for a given Gaussian integration point in some finite element in the structure is then determined as $\Delta\varepsilon_{max}/10^{-4}$. In crack propagation experiments in a compact type specimen, the stress and strain increments are large only in the immediate vicinity of the crack tip. All other elements away from the crack tip vicinity generally experience small strain increments. Thus, in the element ahead of the crack tip, the Gaussian integration points may require 50 subincrements, while those elements further from the crack tip generally require only 2 or 3 subincrements.

If the finite element load increment is large, then all of the finite elements will require a large number of subincrements to integrate the constitutive relations. This will be the case for structures which are free of large stress or strain gradients. However, for cracked structures, the large stress and strain gradients in the vicinity of the cracks and stress risers prevent large finite element load increments from being taken. This arises from the fact that the large stress or strain gradients give a very small radius of convergence to the Newton-Raphson iteration method for solving the finite element equilibrium equations. This small radius of convergence of the iteration method for cracked structures is not peculiar to the Newton-Raphson method. During the contract a Picard, or successive substitution method, was also used to solve the finite element equilibrium equations. For cracked structures the radius of convergence of this iteration method was also found to be very small. In addition, the rate of convergence for small increments with

the Picard method is linear, whereas the rate of convergence of t.. 'ewton-Raphson method is quadratic. For this reason the Newton-Raphson iteration method for solving the finite element equilibrium equations for cracked structures appears preferable to the Picard successive substitution procedure.

The fact that small finite element increments must be used to solve the equilibrium equations for cracked structures implies that most of the structure is subjected to very small finite element strain increments. One or two subincrements are then required for most of the Gaussian points in the structure, and it is doubtful if more refined integration methods (implicit) are required for these structures.

When continuum damage is coupled with the unified viscoplastic equations, the system becomes unstable when the damage parameter approaches unity. In this case the constitutive equations, when written in differential equation form, will always tend to exhibit unstable behavior whether or not explicit forward difference or implicit backward difference methods are used in the integration method. The tendency to unstable behavior in the differential equations arises from the fact that the right hand sides of the differential equations become very large as the damage parameters approaches unity. In this case it may be advantageous to apply a recursion method (see [7]) to integrate the integral form of the unified constitutive equations, since in this case the factor (1-D) appears on the right hand side of the equation for the stress. As D approaches unity the stress decreases to zero and no instability should be encountered.

2.4.2 Creep Crack Growth Modeling

Experimental creep crack growth data have been generated during the present contract by loading compact type specimens of INCO 718 with applied load levels of 4000 lb and 4725 lb at 1200°F (649°C). It is difficult to measure crack length as a function of time on the surface of the compact type specimen with any accuracy due to the fact that the amount of crack growth is usually small, and the crack may grow internally in the specimen without associated surface crack growth. Instead of measuring creep crack growth directly, displacements across the crack were measured as a function of time at the two points shown in Figure 2-29 by means of speckle interferometry (refer to paragraph 2.5). Finite element calculations were then used to determine the theoretical creep crack growth rate with computed displacements at the two speckle interferometry points which agreed with the experimental measurements. Crack growth versus time is then obtained indirectly from the analytical results in the manner employed by Hinnerichs [4].

The computations were made using plane stress assumptions. Plane stress calculations were chosen based on the analysis reported by Atluri and Nakagaki [10] where theoretical plane stress J integral values gave the best agreement with 1.0 inch thick compact type specimen test data. The thickness of the compact type specimens used in the present contract is 0.5 inch. Plane stress computations were also chosen by Hinnerichs [4] to analyze creep crack growth in a center cracked plate which had a thickness of 0.3 inch with crack lengths as small as 0.12 inch.

Figure 2-30 shows the finite element mesh used to analyze one half of the compact type specimen. The mesh for the creep crack growth computations consists of 115 isoparametric 8 noded quadrilateral elements with 420 node points. Reduced integration was employed in the analysis so that the surface integrations over each element, required in the formulation of the matrices in equation (12), employed only four Gaussian integration points per element. Thirty-six square elements, each of dimension 0.01 in. by 0.01 in., are located in the area immediately surrounding the crack tip. Details of the crack tip mesh are displayed in Figure 2-31.
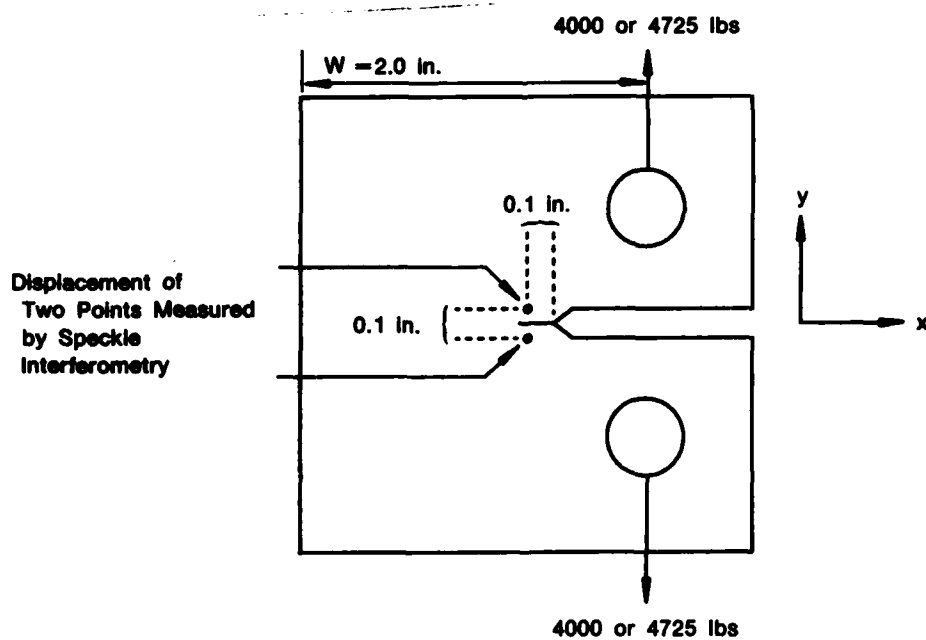
Figure 2-29. *Location of Two Points on Either Side of the Crack Where Displacement Is Measured by Speckle Interferometry*
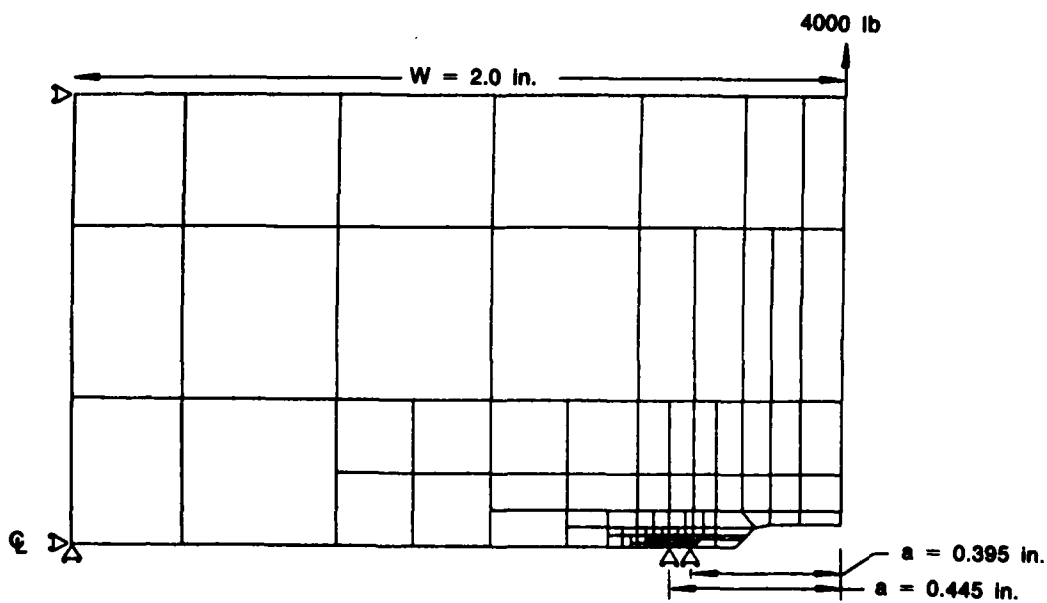
Figure 2-30. *Finite Element Mesh for Creep Crack Growth in Compact Type Specimen*
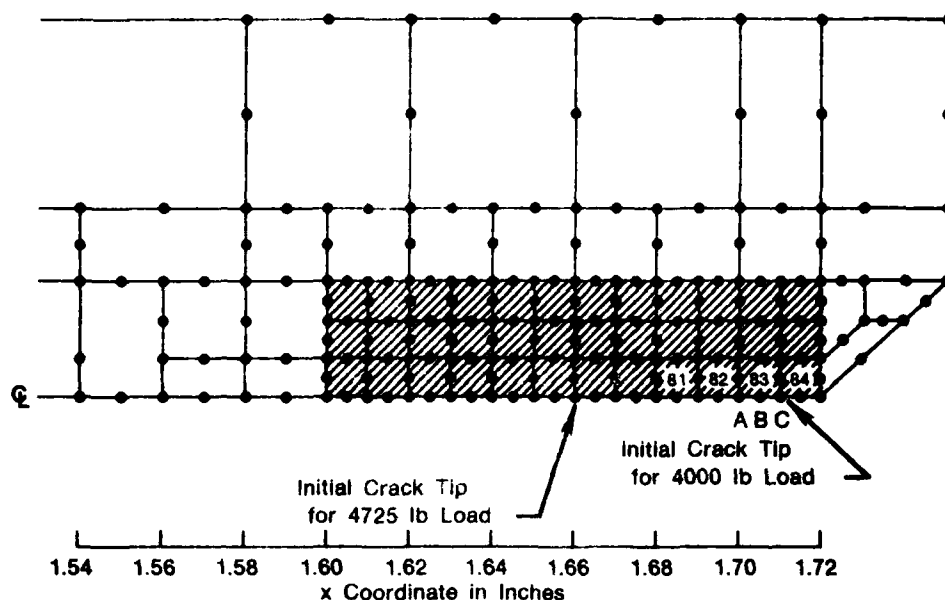
Figure 2-31. Detail of Crack Tip Region in Compact Type Specimen

The adequacy of the finite element mesh was checked by computing the elastic stress intensity factor generated by the model under plane strain conditions. For an applied load P, the stress intensity factor is given by

$$K_1 = \left[\frac{EP}{t\,(1-\nu^2)} \quad \frac{\delta(a+1) - \delta(a)}{1} \right]^{1/2} \tag{17}$$

In the above formula, a is the perpendicular distance from the crack tip to the point of application of the load P, and $\delta(a)$ is the displacement of the load application point perpendicular to the centerline of the compact type specimen and measured with respect to the centerline. The displacement $\delta(a+1)$ is the corresponding displacement of the load application point when the crack is of length a+1, with $1 < a$. Using the values P = 4000 lbs, E = 26.3 × 10⁶ lb/in.², v = 0.3, t = 0.5 in., a = 0.395 in.; 1 = 0.01 in.; the plane strain elastic finite element model gives $\delta(a+1)$ = 2.6978 × 10⁻³ in. and $\delta(a)$ = 2.6735 × 10⁻³ in. Equation (17) then yields the value K_1 = 23,701 lb/in.³/². The handbook formula [11] for the elastic stress intensity factor of a compact type specimen is

$$K_1 = \frac{P}{t\sqrt{W}} \quad \frac{[0.886 + 4.64\alpha - 13.32\alpha^2 + 14.72\alpha^3 - 5.6\alpha^4](2 + \alpha)}{(1-\alpha)^{3/2}} \tag{18}$$

where

$$\alpha = a/W \tag{19}$$

2-34

This formula is valid for $0.2 \leq a/W \leq 1$. Taking $a = 0.395$ in., $W = 2$ in. gives $a/W = 0.1975$ which lies just below the inferior limit. With $P = 4000$ lb, $t = 0.5$ in., $W = 2.0$ in., the handbook stress intensity factor is

$$K_t = 23996 \text{ lb/in.}^{3/2}$$

which compares favorably with the finite element prediction of

$$K_I = 23701 \text{ lb/in.}^{3/2}$$

For the case of the 4725 lb applied load, the values for insertion into equation (12) are:

$P = 4725$ lb, $E = 26.3 \times 10^6$ lb/in.^{2}, $v = 0.3$, $t = 0.5$ in., $a = 0.445$ in., $l = 0.01$ in., $\delta(a+l) = 3.3401 \times 10^{-3}$ in., $\delta(a) = 3.3081 \times 10^{-3}$ in. The finite element plane strain calculation of the elastic stress intensity factor therefore gives

$$K_I = 29560 \text{ lb/in.}^{3/2}$$

while the handbook formula for $a/W = 0.2225$ and $t = 0.5$ in. gives

$$K_I = 30488 \text{ lb/in.}^{3/2}.$$

For both of the applied loads, the finite element mesh gives plane strain elastic stress intensity factors which compare favorably with the handbook values. This justifies the use of the mesh for further crack growth studies.

The finite element predictions were made by applying the load to the top surface of the specimen as indicated in Figure 2-30. No modeling of the actual pin hole was attempted. In order to study the effect of different loading conditions on the elastic stress intensity factor, several plane strain elastic calculations were performed using the boundary element method. In this method only the boundary of the compact type specimen is modeled so that it is an easy matter to change the element mesh and loading conditions. The boundary element method is described in the books by Brebbia [12] and Banerjee and Butterfield [13]. A simple program employing constant displacement and tractions in each boundary element was employed. The compact type specimen was modeled with a total of 122 boundary elements with 244 degrees of freedom. Details of the boundary element mesh in the vicinity of the crack tip for the 4000 lb loading condition with a crack of length 0.395 in. is shown in Figure 2-32. The stresses σ_{xx}, σ_{yy} and σ_{xy} at a polar angle of $\theta = \pi/2$ and at radii of 0.0005, 0.001, 0.004, 0.006, 0.008, and 0.010 in. from the crack tip were computed with the boundary element program. Results of the plane strain elastic stress intensity factor calculations for three different loading conditions are displayed in Table 2-8. The results indicate that the omission of the pin hole, and the subsequent removal of the applied load, P, to the more distant upper surface of the compact type specimen, does not significantly affect the stress intensity in the crack tip vicinity. It would appear, however, that omission of the pin hole with the load applied at the pin hole position, increases the stress intensity factor at the crack tip for a/W values around $a/W \approx 0.2$.

A further comment on the finite element calculations may be made at this point. In both the finite element and boundary element calculations, the end of the compact type was modeled with roller boundary conditions. These can be seen on the left hand side of Figure 2-30. It would have been preferable to have used zero traction boundary conditions on the left hand side and to have imposed the condition that the applied load can move only in the vertical direction but not in the horizontal direction. These boundary conditions are more in accord with the actual experimental conditions. From the agreement of the finite element stress intensity calculations with the ASTM handbook result, it is concluded that the different boundary conditions would not have a significant impact on the stress state in the crack tip vicinity.

Internal Points in Boundary
Element Stress Calculation

$r = 10 \times 10^{-4}$

$r = 5 \times 10^{-4}$

$\theta = \dfrac{\pi}{2}$

7×10^{-4} 3×10^{-4} 10^{-4} 10^{-4} 10^{-4} 3×10^{-4} 7×10^{-4}
10^{-4} 10^{-4} 10^{-4}

Crack Tip

Crack Length = 0.395 in.
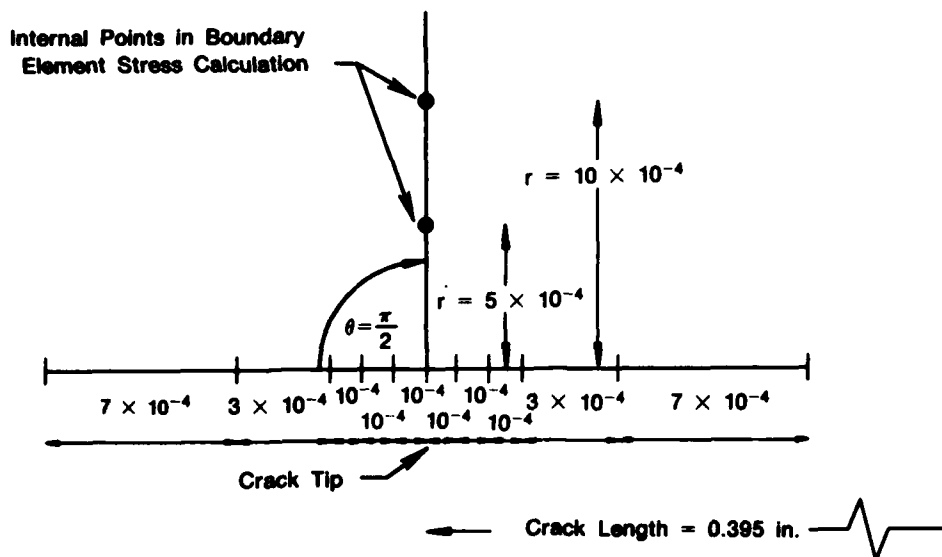
FD 268890

Figure 2-32. Boundary Element Distribution in the Vicinity of the Crack Tip

Table 2-8. Effect of Pinhole and Point of Load Application on the Elastic Stress Intensity Factor K_I Obtained from Boundary Element Method

$a = 0.395$
$W = 2.00$
$t = 0.50$

θ	r	K_I^*	K_I^{**}	K_I^{***}	K_I^*	K_I^{**}	K_I^{***}	K_I^*	K_I^{**}	K_I^{***}
$\pi/2$	0.0005	17608	21108	22930	20665	24685	26916	18980	22476	24726
$\pi/2$	0.001	18665	20467	21634	21902	23884	25394	20118	21665	23332
$\pi/2$	0.004	19408	19736	20493	22755	22824	24075	20906	20473	22131
$\pi/2$	0.006	19414	19693	20436	22752	22669	24033	20906	20249	22095
$\pi/2$	0.008	19383	19742	20377	22705	22636	23996	20867	20155	22062
$\pi/2$	0.01	19345	19833	20287	22649	22658	23927	20821	20123	21999

$$K_I^* = \sigma_y \sqrt{2\pi r} \left[\cos\frac{\theta}{2} \left(1 + \sin\frac{\theta}{2} \sin\frac{3\theta}{2} \right) \right]^{-1}$$

$$K_I^{**} = \sigma_x \sqrt{2\pi r} \left[\cos\frac{\theta}{2} \left(1 - \sin\frac{\theta}{2} \sin\frac{3\theta}{2} \right) \right]^{-1}$$

$$K_I^{***} = \sigma_{xy} \sqrt{2\pi r} \left[\cos\frac{\theta}{2} \sin\frac{\theta}{2} \cos\frac{3\theta}{2} \right]^{-1}$$

$K_I = 23701$ by finite element method

$K_I = 23996$ by handbook formula

Tip of
Crack

2-36
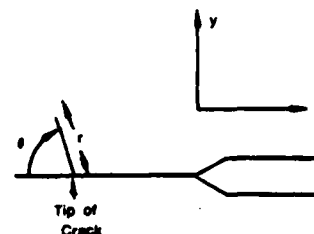
Initially, the continuum damage model was incorporated into the unified viscoplastic constitutive formulation, and the complete constitutive/continuum damage model was coded into a FORTRAN subroutine of the ABAQUS finite element program. When the compact type specimen is initially loaded to 4000 lb, a rapid stress redistribution occurs at the Gaussian integration points closest to the crack tip. The stress at the point closest to the crack tip relaxes (decreases) while the stresses at the points further removed from the crack tip increase slightly to preserve global equilibrium. After about 10 seconds the stress redistribution stabilizes and no further change in the state of the compact type specimen occurs until about 94 minutes have elapsed. The equivalent Von Mises stress at the Gaussian integration point closest to the crack tip, viz., point 2 in element number 83 of Figure 2-33, has a value of 139,200 lb/in.^{2} . The equivalent stress at integration point 1 of element 83 which is further removed from the crack tip has a much lower value of 100,600 lb/in.^{2}. After 94 minutes at the constant stabilized equivalent stress value of 139,200 lb/in.^{2}, integration point 2 in element 83 begins to rapidly accumulate creep damage and failure (creep rupture) occurs after 94.2 minutes. At this point the integration procedure becomes unstable as the damage parameter approaches values close to unity.
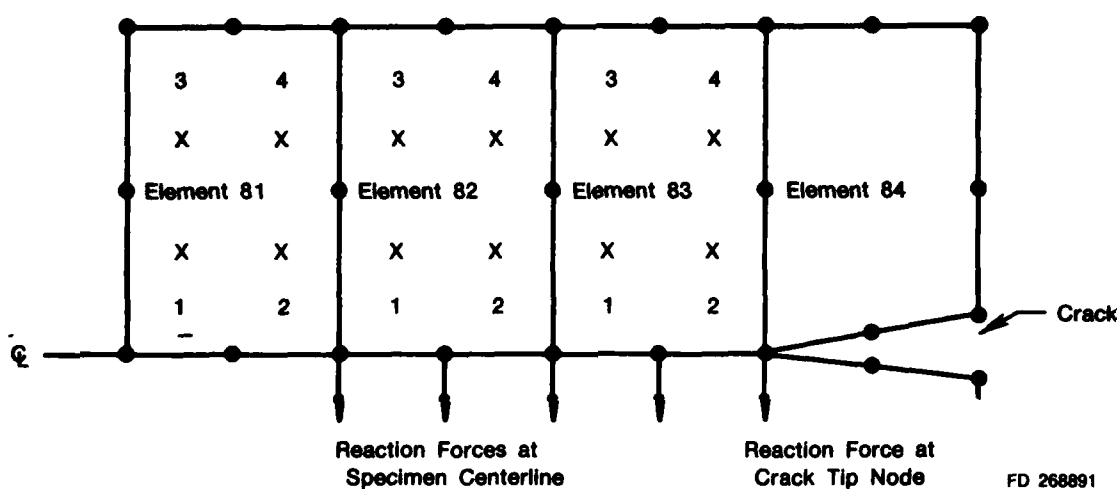
Figure 2-33. Detail of Crack Tip Showing Reaction Forces and Gaussian Integration Points

To avoid this instability, the Gaussian integration point was initially assumed to have failed when the inelastic strain rate with damage included in the constitutive formulation reached three times the magnitude of the inelastic strain rate without damage included in the formulation. However, this results in creep rupture times which were much smaller than the true creep rupture time. By assuming that failure occurs when the damage parameter reaches a value of $D \approx 0.7$, instability is again encountered at high stress levels. There appears to be no way of avoiding the continuum damage instability in the integration of the stiff unified viscoplastic constitutive equations as long as they are integrated as differential equations. An integral formulation of unified viscoplastic formulation may be found in Reference [7], and it would appear that instability can be avoided if the integration procedure uses a recursion procedure to step from time = t to time = t + Δt. This procedure was not used in the present contract due to the fact that a suitable algebraic Jacobian matrix, $J = (\partial \sigma / \partial \varepsilon)_{t+\Delta t}$, could not be developed. Some recent applications of the numerical procedure to determine the Jacobian matrix for the integral formulation have proved successful, and this method ought to be pursued further in an attempt to obtain a stable integration method for the coupled viscoplastic/damage equations.

Since the equivalent stress at the integration point closest to the crack tip remains constant for 94 minutes after the initial 15 second transient, and failure occurs at 94.2 minutes, it was

2-37

decided to remove the damage computation from the viscoplastic FORTRAN subroutine to avoid the instability due to continuum damage accumulation.

The computations for creep crack growth now proceeds as follows. First, the compact type specimen is loaded to either 4000 lb or to 4725 lb. After a brief transient stress redistribution in the vicinity of the crack tip, the equivalent stress remains constant at the Gaussian integration point closest to the crack tip, viz. integration point 2 in element 83 of Figure 2-33. The time to failure for this integration point can then be determined from equation (2). From equation (5) of Appendix B, the last two terms are responsible for decreasing the stress at a material point due to the growth of the damage parameter D. That is to say, as the point fails and its load carrying capacity diminishes with increasing damage, the stress at that point decreases and the load which it carries is shed onto other surrounding material points in the structure. To simulate this decrease in the load carrying capacity of the Gaussian integration point, four increments are carried out in which the stress components are reduced by one half of their value at the beginning of each increment. Each increment lasts for 0.25 second, so that once failure is deemed to have occurred, the stress is reduced to about 6 percent of its initial stabilized value at the integration point in 1 second. In each succeeding increment the stress is further reduced by one half of its value as the analysis proceeds. Integration point 2 of element 83 in Figure 2-33 has now failed. The displacement boundary conditions at crack tip node C in Figure 2-33 are replaced by force boundary conditions. The reaction force required to hold the crack tip node C in its current location is then released in four (4) increments over a period of 1 second and the crack advances to the adjacent node B halfway through the isoparametric element.

A brief transient stress redistribution lasting for about 15 seconds again occurs, followed by a stabilized condition. The equivalent stress after stabilization is then computed at integration point 1 of element 83, and the time to rupture determined once again from equation (2). Once failure has occurred the stress is shed from integration point 1 to 6 percent of its value in 1 second, and the crack tip node B is released in four increments over a 1 second period and the crack advances completely through the isoparametric element to the adjacent node A. This procedure is repeated for all nodes lying in the crack plane ahead of the advancing crack.

The justification for the decoupling of the viscoplastic and continuum damage constitutive models is based on the following observations:

A. The stress falls off very rapidly from the crack tip in the crack plane of a compact type specimen. Consequently the stress at the integration point closest to the crack tip is large and the rupture or failure time is fairly small. The second integration point in the crack tip element and the integration points further away are subjected to such small stresses that the amount of damage accumulated by these points at the time the integration point closest to the crack tip fails is practically zero. The creep rupture time in equation (2) can then be used for each integration point in turn. Even if the damage accrued by each point is not small, the rupture time can still be determined from equation (1) by integration.

B. The transient stress redistribution after initial load-up or after a node release, redistributes in a time which is much smaller than the time required to fail or rupture the integration points closest to the crack plane. Each integration point is therefore subjected to a constant stabilized stress for most of its life.

2.4.3 Fatigue Crack Growth Modeling

Experimental fatigue crack growth data have been generated during the present contract by loading compact type specimens of INCO 718 with cyclic triangular load histories at 1200°F (649°C). The stress ratio (R) used was 0.1 with maximum and minimum loads of P_{max} = 3069 lb and P_{min} = 307 lb applied at a frequency of 10 cycles per minute (cpm). Crack length was determined directly as a function of cycle number by averaging the measured crack length on each side of the specimen. One compact type specimen was subjected to a pure fatigue loading of 10 cpm until fracture occurred, while the other was subjected to the same fatigue loading history with four dwell periods early in the life of the specimen. During these dwell periods the load was maintained at the maximum value of 3069 lb for 30 minutes.

The finite element computations were made with plane stress assumptions using eight (8) noded isoparametric quadrilateral elements with reduced integration, viz. four (4) Gaussian integration points per element. For the reasons cited in section 2.4.2 the fatigue crack computations were made using the uncoupled damage and viscoplastic constitutive formulations.

Computations of the fatigue crack growth proceed as follows. The compact type specimen is first loaded to a maximum load P_{max}, then unloaded to the minimum load, P_{min}, and finally reloaded to P_{max}. During this cycle the maximum and minimum principal stress values at the Gaussian integration point closest to the crack tip are determined. The assumption is then made that this cycle continues unaltered until fatigue fracture of the point occurs. The number of cycles required to fracture the Gaussian integration point is given by the three-dimensional form of equation (6). The specimen is now unloaded to the minimum load value P_{min}.

As with the creep calculations, the decrease in the load carrying capacity of the integration point was simulated by carrying out four increments in which the stress components are reduced by one half of their value at the beginning of each increment. Each increment lasts for 0.25 second, so that once fatigue failure is deemed to have occurred, the stress is reduced to about 6 percent of its initial value at the failed Gaussian integration point in 1 second. In each succeeding increment the stress is further reduced by one half of its value as the analysis proceeds. After failure of the integration point the displacement boundary conditions at the crack tip node are replaced by force boundary conditions. The reaction force required to hold the crack tip node on the centerline of the specimen is then reduced to zero in four increments over a period of 1 second. The crack then advances to the adjacent node on the crack plane halfway through the isoparametric element.

The specimen is now at the minimum load value with the crack advanced halfway through an element. A cycle is now imposed on the specimen in which the load is increased to P_{max}, decreased to P_{min} and increased once again to P_{max}. During this cycle the maximum and minimum principal stresses at the new integration point ahead of the crack tip are determined and the number of cycles required to fracture this new integration point are determined. The integration point's load carrying capacity is then diminished by forcible stress reduction and the crack tip node is released after the load is decreased to P_{min}. This procedure is repeated for each node release.

2.5 EXPERIMENTAL MEASUREMENTS

All test specimens were machined from AMS 5596C (INCO 718) in the form of 0.5 in. (12.7 mm) thick flat plates having nominal dimensions of 12 in. × 4 in. (305 mm × 102 mm). The specimens were oriented with the fracture surfaces parallel to the rolling direction.

The smooth axial low cycle fatigue (LCF) specimens shown in Figure 2-34 were designed to conform to the ASTM E 606-80 recommended practice for constant amplitude low cycle fatigue testing.

Figure 2-34. Low Cycle Fatigue (LCF) Specimen

The tests were conducted in closed-loop servohydraulic LCF test machines. The temperature was maintained with clamshell-type furnaces and controlled uniformly over the specimen gage section.

The creep and tensile specimens were oriented in the same direction as the LCF specimens. The tests were also conducted under the appropriate ASTM standards.

The standard compact type (CT) specimen shown in Figure 2-35 was used to obtain the crack growth rate and the creep crack growth rate data. The cyclic crack growth testing was conducted on a servohydraulic closed-loop, load-controlled testing machine, and the creep crack growth testing was conducted on a hydraulic constant load test frame. All precracking and testing was performed in accordance with procedures outlined in ASTM 647-83. The crack lengths for the cyclic tests were measured on both surfaces directly with a traveling microscope. The specimen heating was provided by resistance, clamshell furnaces having windows to allow observation of the crack growth at test temperature. The crack extension for the creep crack growth tests was determined by a laser heterodyne optical strain measurement system which is discussed in the following paragraphs.

The concept of the heterodyne optical strain measurement system is illustrated in Figure 2-36. A laser beam is split into two parallel beams illuminating two closely spaced points on the object. The comparatively rough surface of the object scatters the laser light in a random manner resulting in two speckle fields reflected from the object surface. These two speckle fields are imaged by a lens system onto the film plane. If a photographic plate is placed at the film plane, a photographic recording of this speckle interference pattern is made.

2-40
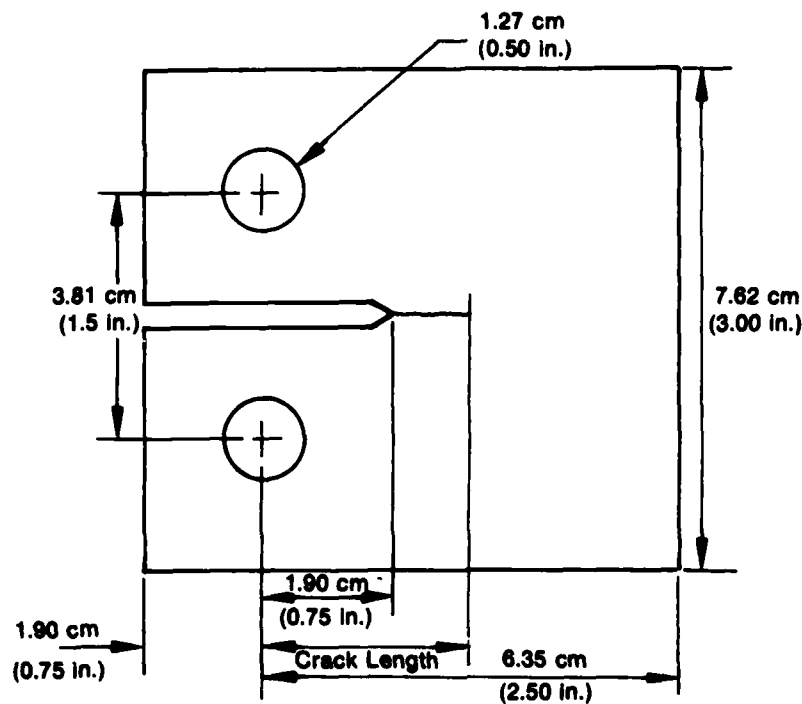
FD 119166A

Figure 2-35. Compact Type (CT) Specimen
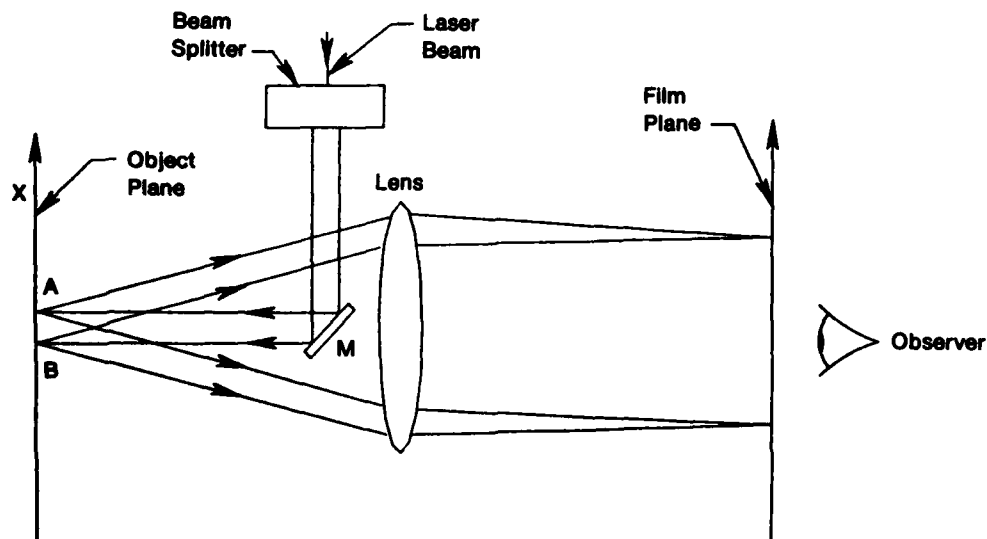
FD 268898

Figure 2-36. Optical Strain Measurement Concept

The recording of the speckle interference pattern is then relocated in the same position it occupied during exposure. When the object is loaded in the X direction (Figure 2-36) causing points A and B on the object to separate in-plane, the spatial frequency of the fine interference fringes will change relative to the pattern previously recorded on the photographic plate with no load on the object. The effect of this change in frequency is to generate a change of phase angle

between the interference pattern reflected from the object and the one recorded on the plate. The result to the observer will be the creation of a Moire' fringe pattern, each fringe of which represents a 180 degree shift in phase. The spatial frequency of these Moire' fringes is proportional to the strain on the object between points A and B.

In previous methods, the Moire' fringes were simply counted and the number of fringes directly related to strain. However, these methods have significant limitations in accurately of measuring strain, such as: (1) strain values corresponding to less than one fringe across the field of view cannot be measured, (2) location of the fringe centers is not accurate, and (3) no distinction can be made between positive and negative strain. All of these undesirable limitations can be eliminated by the incorporation of heterodyned interferometry.

To implement heterodyned interferometry into the system shown in Figure 2-36, a device for constantly changing the phase of the laser beam prior to the beam splitter is added. This causes the Moire' fringes observed in the film plane to scan across the field of view in a constant direction. If the observer is replaced by a photo diode, the output of which is supplied to a phase meter, small changes in phase can easily be measured. Phase meters can accurately measure phase changes to within 0.5 degree which is equivalent to dividing each Moire' fringe into 1000 parts. Therefore, heterodyned readout of the Moire' fringes greatly increases the resolution and accuracy over typical optical techniques.

The heterodyne optical strain measurement system developed in the Materials Engineering and Technology Laboratory (ME&T) of Pratt & Whitney (P&W) is shown in Figure 2-37. The laser used is a 2 watt argon ion laser. The heterodyne signal is provided by a $\lambda/2$ retarder plate mounted in the hollow shaft of an electric motor and by a stationary $\lambda/4$ retarder. The laser beam is split by a calcite beam displacer into two parallel beams 0.100 in. apart, which are then directed by mirrors to the specimen. The light scattered from the specimen is gathered by the strain sensor head and focused onto the photographic plate located in the plate holder. Two photodiodes are placed directly behind the plate.

The signals from the photodiodes after being amplified and filtered, are fed into a counter that measures the phase of the signal from one of the diodes relative to the other. It has been shown that the phase difference between the two signals (φ) can be related to the in-plane strain on the specimen (ε) by:

$$\varepsilon = (\varphi/360)\,(\lambda/2d \sin \theta)$$

where
λ = wavelength of laser light
d = distance between two laser beams
θ = half the angle from the specimen surface to the photodiodes

To conduct elevated temperature tests, an enclosure to stagnate the air between the specimen and the photodiodes is required as shown in Figure 2-37. An access port in the side of the furnace allows the light to reach the specimen and reflect back to the sensor head through a tunnel. The box around the sensor head helps stagnate the air and also shields the photodiodes from room lights.

Figure 2-37. Optical Strain System With Furnace, Tunnel, and Enclosure In-Place

3.1 CREEP CRACK GROWTH

The displacement of two points, located on either side of the crack tip as shown in Figure 2-29, was measured as a function of time by the speckle interferometry technique described in paragraph 2.5. Specimen dimensions and pertinent load data are shown in Figure 3-1.

Creep Specimens		Fatigue Specimen
$P = 4000$	$P = 4725$	$P_{max} = 3069$, $P_{min} = 307$
$W = 2.0$	$W = 2.0$	$W = 2.5$
$a_o = 0.275$	$a_o = 0.275$	$a_o = 0.375$
$a = 0.395$	$a = 0.445$	$a = 0.505$
$t = 0.5$	$t = 0.5$	$t = 0.5$
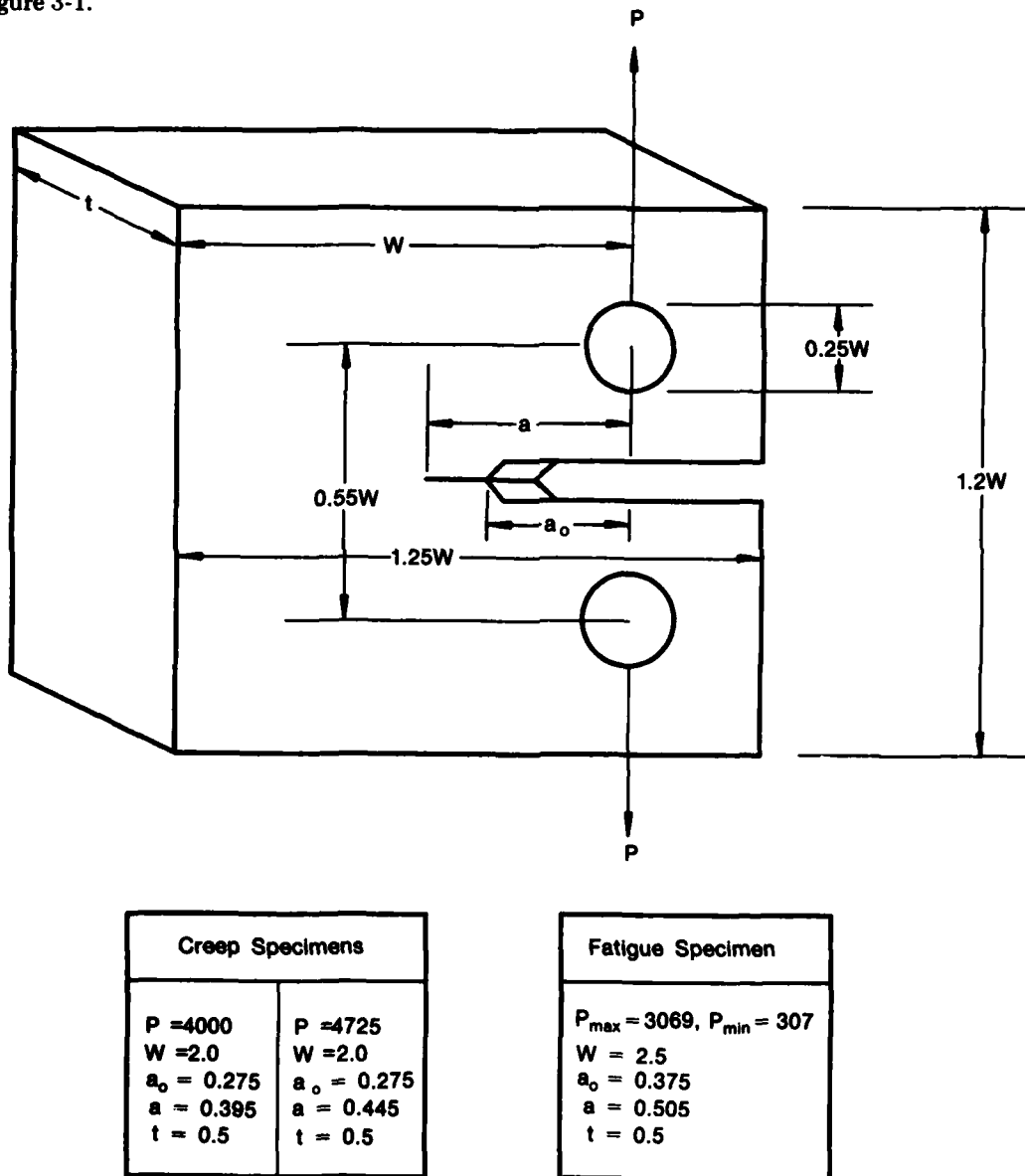
FD 268892

Figure 3-1. Dimensions of Compact Type Specimens Used in Creep and Fatigue Crack Growth Experiments

Figures 3-2 and 3-3 show the experimental displacement of one of the points in the y-direction (see Figure 2-29) as a function of time elapsed after application of load to the compact type specimen. The displacement is measured with respect to the centerline of the specimen and represents an average value for the two locations.
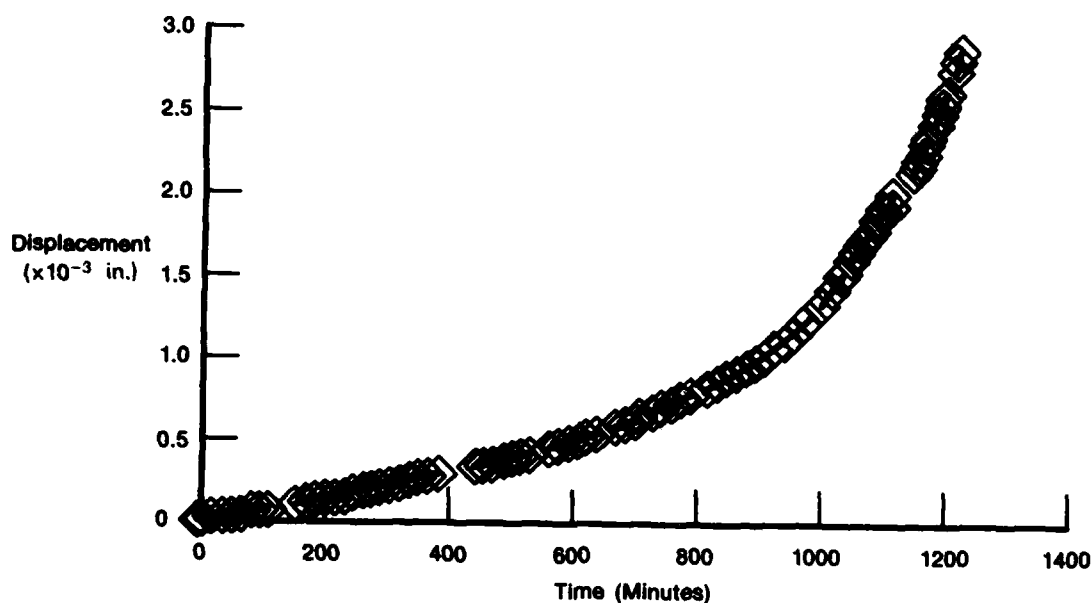
FD 268893

Figure 3-2. *Displacement from Centerline in the y-direction of Speckle Interferometry Point for Specimen Load of 4000 lbs*
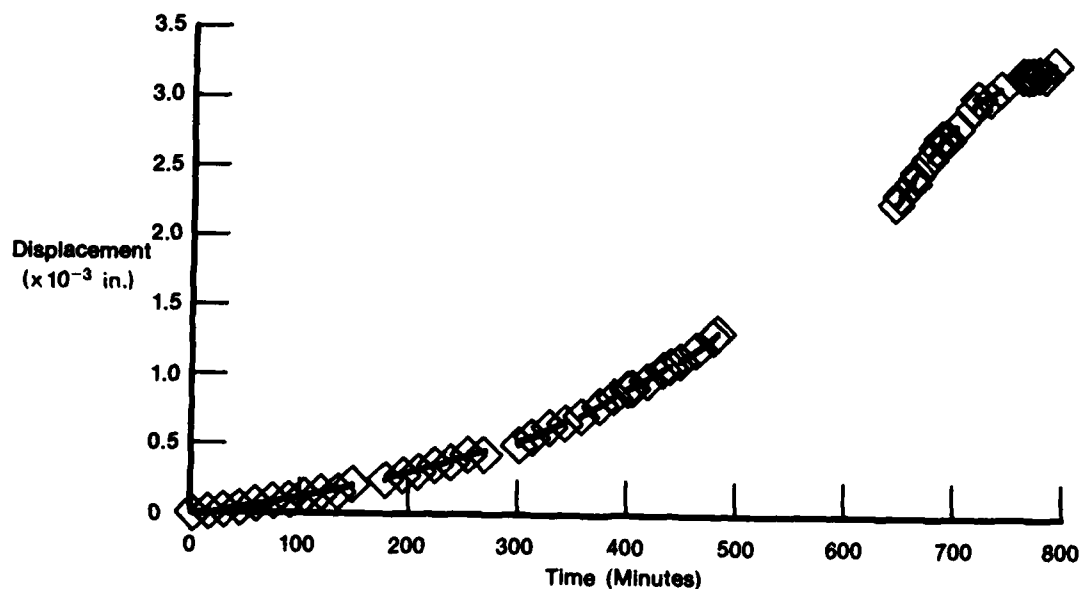
FD 268894

Figure 3-3. *Displacement from Centerline in y-direction of Speckle Interferometry Point for Specimen Load of 4725 lbs*

3-2

The theoretical and experimental results corresponding to the initial portion of these curves are displayed in Figures 3-4 and 3-5. Tables 3-1 and 3-2 give the Von Mises equivalent stress, σ_{II}, obtained from the finite element calculations, and the time required to rupture each Gaussian integration point, t_r, computed with the formula

$$t_R = [A\sigma_{II}^r \{k(\sigma_{II}) + 1\}]^{-1}.$$

(20)

FD 268895
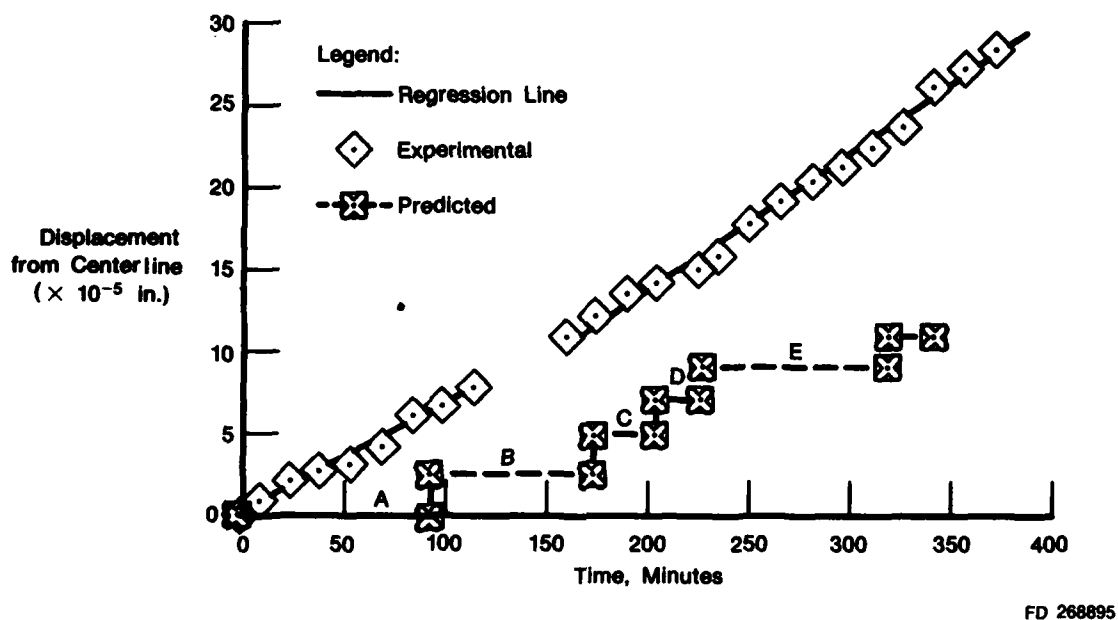
Figure 3-4. Comparison of Measured and Predicted Displacements for Loads of 4000 lbs

FD 268896
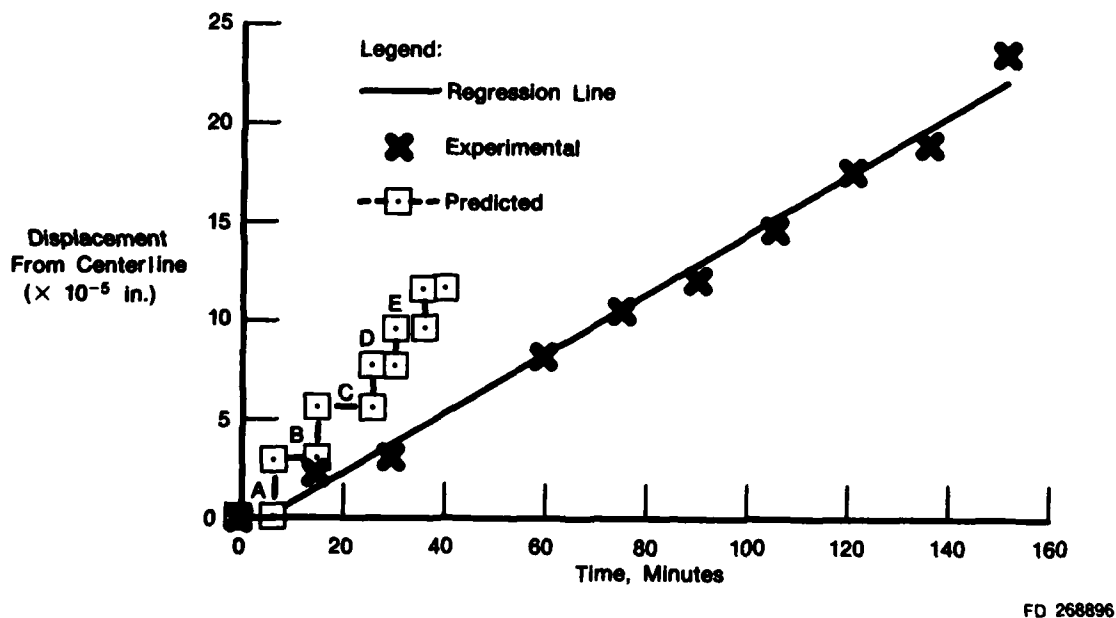
Figure 3-5. Comparison of Measured and Predicted Displacements for Loads of 4725 lbs

3-3

Table 3-1. Finite Element Equivalent Stress versus Rupture Time for 4725 lb Load

Portion of Curve	Prior to Release of Node Number	σ_{II} (psi) Calculated	t_R (sec)* from Eqn (20)	t_R (sec) Required for Calculation to Agree With Experiment
A	1	158,200	385	770
B	2	156,100	516	1,032
C	3	154,500	646	1,292
D	4	161,000	261	522
E	5	159,500	321	642

* t_R is computed from equation (20) using the material constants A = 2.394 × 10⁻⁴³, r = 7.22, k(σ_{II}) = 1 + (1.011 × 10⁻⁴) exp (9.446 × 10⁻⁵σ_{II}), corresponding to a least square fit of the uniaxial creep rupture data obtained in the present contract.

Table 3-2. Finite Element Equivalent Stress versus Rupture Time for 4000 lb Load

Portion of Curve	Prior to Release of Node Number	σ_{II} (psi) Calculated	t_R (sec)* from Eqn (20)	t_R (sec) Required for Calculation to Agree With Experiment
A	1	139,200	5,652	2,826
B	2	140,300	4,830	2,415
C	3	147,200	1,809	904
D	4	149,300	1,343	672
E	5	139,400	5,492	2,746

* t_R is computed from equation (20) using the material constants A = 2.394 × 10⁻⁴³, r = 7.22, k(σ_{II}) = 1 + (1.011 × 10⁻⁴) exp (9.446 × 10⁻⁵σ_{II}), corresponding to a least square fit of the uniaxial creep rupture data obtained in the present contract.

The portions of the curves labelled A, B, C, D, and E in Figures 3-4 and 3-5 correspond to stabilized behavior of the compact type specimen after the 15 second transient and prior to the release of nodes 1, 2, 3, 4, and 5 ahead of the crack tip. As noted in Table 3-1 the material constants A and r in the creep rupture equation are chosen to give a least square fit to the uniaxial creep rupture data generated in the present contract, as opposed to the values quoted in Figure 2-17, which correspond to a least square fit to three sets of independent data.

It is clear from Figures 3-4 and 3-5 that the computed displacement, and hence the computed creep crack growth rate, is about a factor of two, too small at the 4000 lb loading level and too large at the 4725 lb loading level. Hence, the material constants generated from the uniaxial creep rupture data also give an approximate least square fit to the creep crack growth data.

Tables 3-1 and 3-2 show the rupture times required for the creep crack growth calculations to give agreement with the experimental displacements displayed in Figures 3-4 and 3-5. These times were obtained very simply by doubling and halving the computed creep rupture times for the 4725 lb and 4000 lb load cases. A plot of log σ_{II} vs log t_R obtained in this manner from Tables 3-1 and 3-2, which gives agreement between the experimental and finite element displacements at the speckle interferometry points, is given in Figure 2-17. As expected, the points lie on either side of the least square data line obtained from the three sets of uniaxial creep rupture data.

A plot of the Von Mises equivalent stress contours during the creep crack growth computations are shown in Figures 3-6 through 3-15. The frame in which the contours are displayed corresponds to the 36 finite element mesh pattern shown in Figure 2-31. The contours corresponding to negative values of the equivalent stress should be disregarded, since the negative values are used merely to set the contour spacing increments, and are not generated by the finite element calculation.

3-4

Von Mises Equiv Stress
ID   Value

1   −1.00E+05
2   −7.00E+04
3   −4.00E+04
4   −1.00E+04
5   +2.00E+04
6   +5.00E+04
7   +8.00E+04
8   +1.10E+05
9   +1.40E+05
10   +1.70E+05
11   +2.00E+05
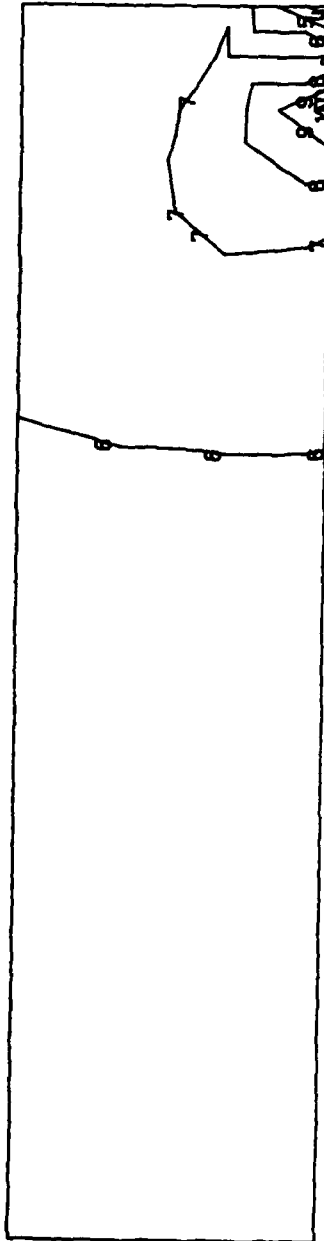
FD 268899

Figure 3-6. Von Mises Equivalent Stress Contours After Initial Load to 4000 lbs

Von Mises Equiv Stress
ID   Value

1   −1.00E+05
2   −7.00E+04
3   −4.00E+04
4   −1.00E+04
5   +2.00E+04
6   +5.00E+04
7   +8.00E+04
8   +1.10E+05
9   +1.40E+05
10   +1.70E+05
11   +2.00E+05
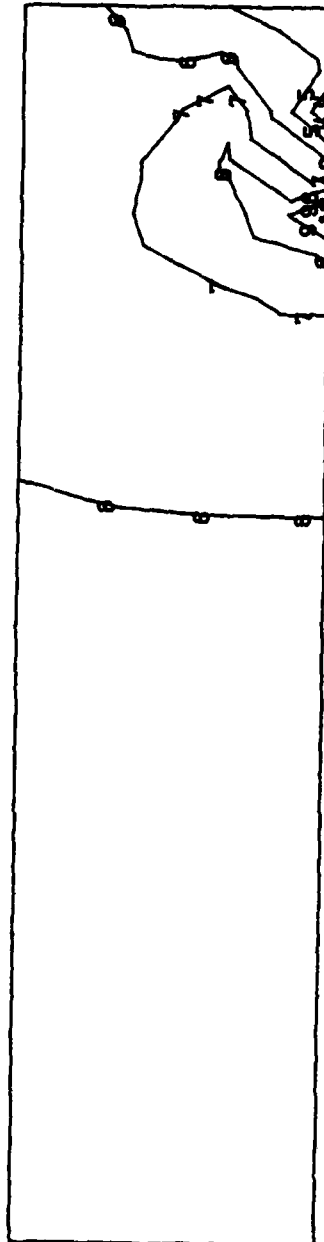
FD 268900

Figure 3-7. Von Mises Equivalent Stress Contours After Release of First Node at 4000 lbs Load Level

Von Mises Equiv Stress

ID	Value
1	−1.00E+05
2	−7.00E+04
3	−4.00E+04
4	−1.00E+04
5	+2.00E+04
6	+5.00E+04
7	+8.00E+04
8	+1.10E+05
9	+1.40E+05
10	+1.70E+05
11	+2.00E+05

FD 271851
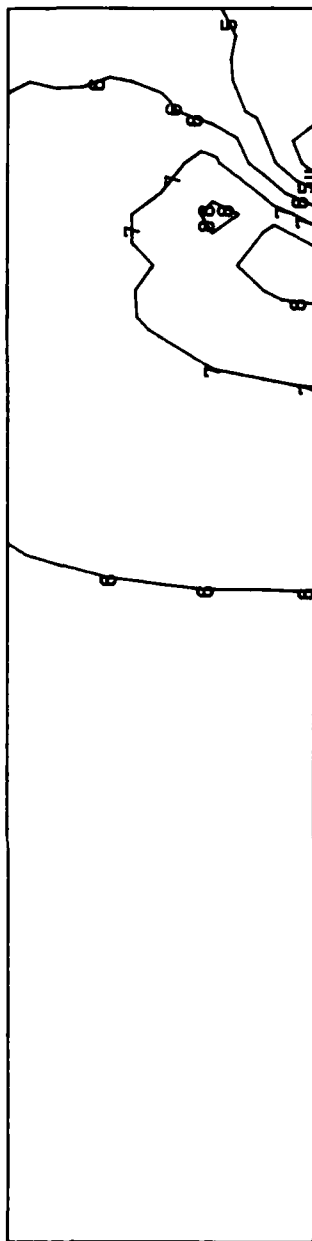
Figure 3-8. Von Mises Equivalent Stress Contours After Release of Second Node at 4000 lbs Load Level

Von Mises Equiv Stress

ID	Value
1	−1.00E+05
2	−7.00E+04
3	−4.00E+04
4	−1.00E+04
5	+2.00E+04
6	+5.00E+04
7	+8.00E+04
8	+1.10E+05
9	+1.40E+05
10	+1.70E+05
11	+2.00E+05

FD 271852
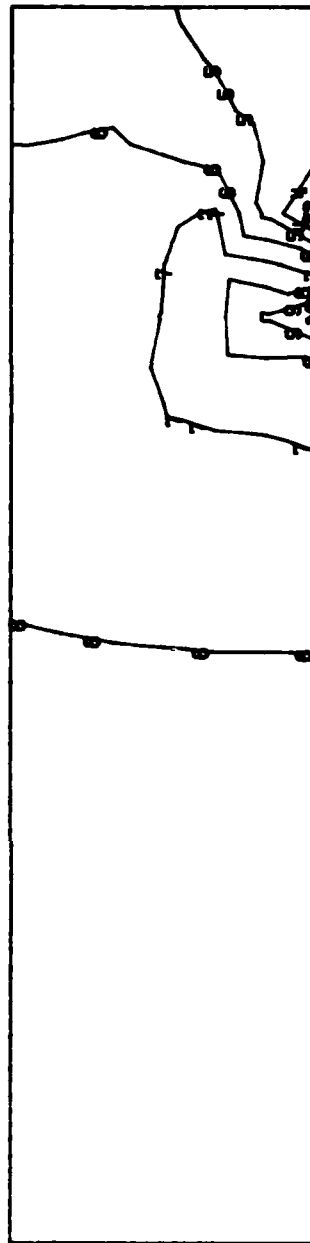
Figure 3-9. Von Mises Equivalent Stress Contours After Release of Third Node at 4000 lbs Load Level

3-6

FD 271653

Von Mises Equiv Stress

ID	Value
1	−1.00E+05
2	−7.00E+04
3	−4.00E+04
4	−1.00E+04
5	+2.00E+04
6	+5.00E+04
7	+8.00E+04
8	+1.10E+05
9	+1.40E+05
10	+1.70E+05
11	+2.00E+05
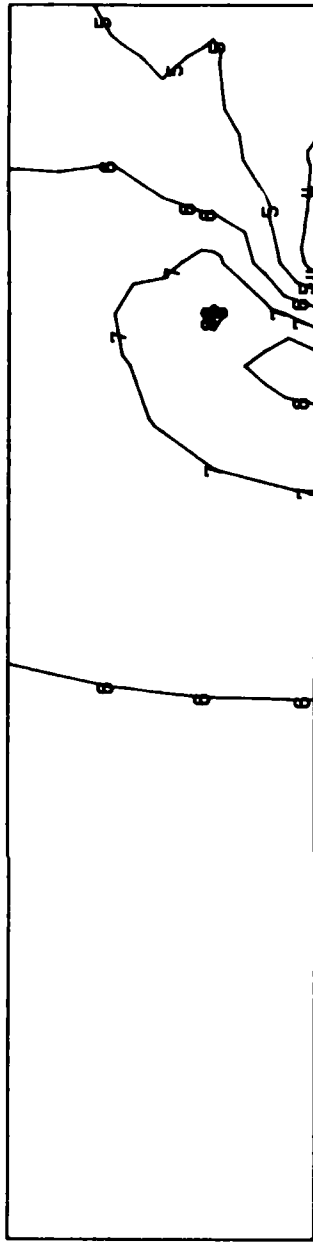
Figure 3-10. Von Mises Equivalent Stress Contours After Release of Fourth Node at 4000 lbs Load Level

FD 271654

Von Mises Equiv Stress

ID	Value
1	+0.00E−00
2	+2.00E+04
3	+4.00E+04
4	+6.00E+04
5	+8.00E+04
6	+1.00E+05
7	+1.20E+05
8	+1.40E+05
9	+1.60E+05
10	+1.80E+05
11	+2.00E+05
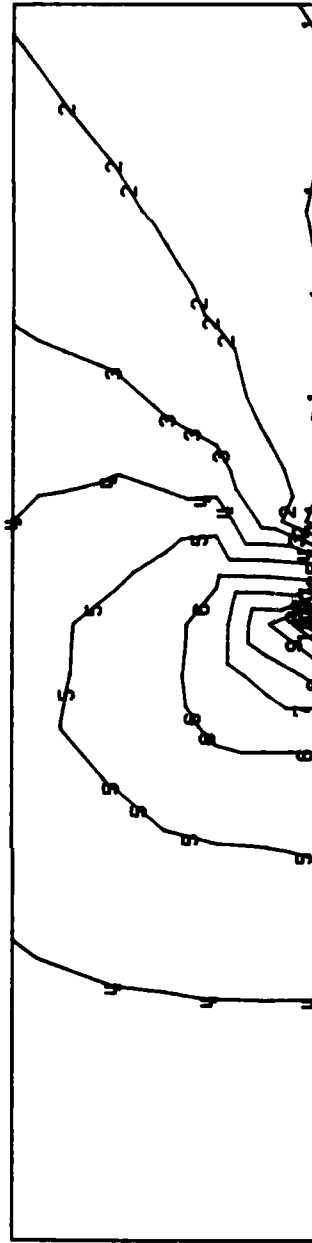
Figure 3-11. Von Mises Equivalent Stress Contours After Initial Load to 4725 lbs

3-7

Von Mises Equiv. Stress
ID	Value
1	−1.00E+05
2	−7.00E+04
3	−4.00E+04
4	−1.00E+04
5	+2.00E+04
6	+5.00E+04
7	+8.00E+04
8	+1.10E+05
9	+1.40E+05
10	+1.70E+05
11	+2.00E+05

FD 271655

Figure 3-12. Von Mises Equivalent Stress Contours After Release of First Node at 4725 lbs Load Level

Von Mises Equiv Stress
ID	Value
1	−1.00E+05
2	−7.00E+04
3	−4.00E+04
4	−1.00E+04
5	+2.00E+04
6	+5.00E+04
7	+8.00E+04
8	+1.10E+05
9	+1.40E+05
10	+1.70E+05
11	+2.00E+05
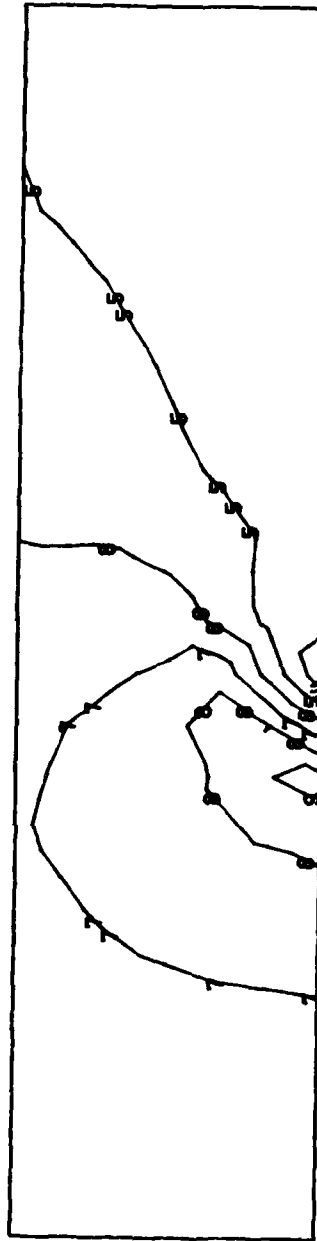
FD 271656

Figure 3-13. Von Mises Equivalent Stress Contours After Release of Second Node at 4725 lbs Load Level

Von Mises Equiv Stress
ID   Value

ID	Value
1	−1.00E+05
2	−7.00E+04
3	−4.00E+04
4	−1.00E+04
5	+2.00E+04
6	+5.00E+04
7	+8.00E+04
8	+1.10E+05
9	+1.40E+05
10	+1.70E+05
11	+2.00E+05
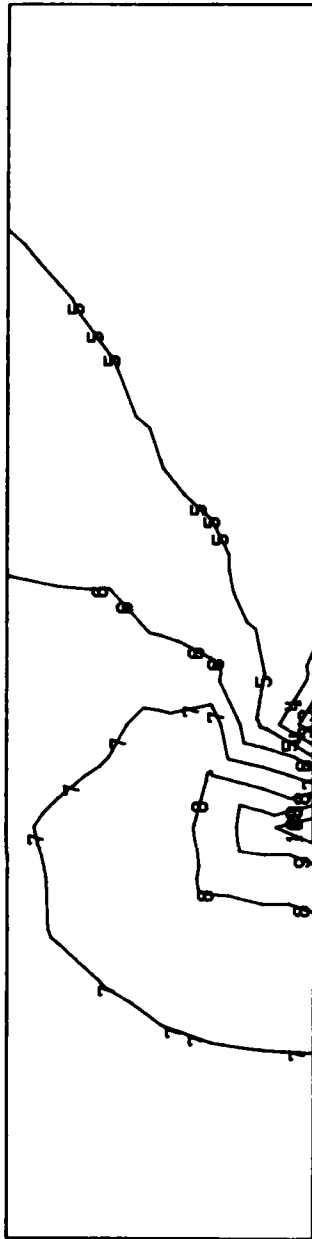
FD 271657

Figure 3-14. Von Mises Equivalent Stress Contours After Release of Third Node at 4725 lbs Load Level

Von Mises Equiv Stress
ID   Value

ID	Value
1	−1.00E+05
2	−7.00E+04
3	−4.00E+04
4	−1.00E+04
5	+2.00E+04
6	+5.00E+04
7	+8.00E+04
8	+1.10E+05
9	+1.40E+05
10	+1.70E+05
11	+2.00E+05
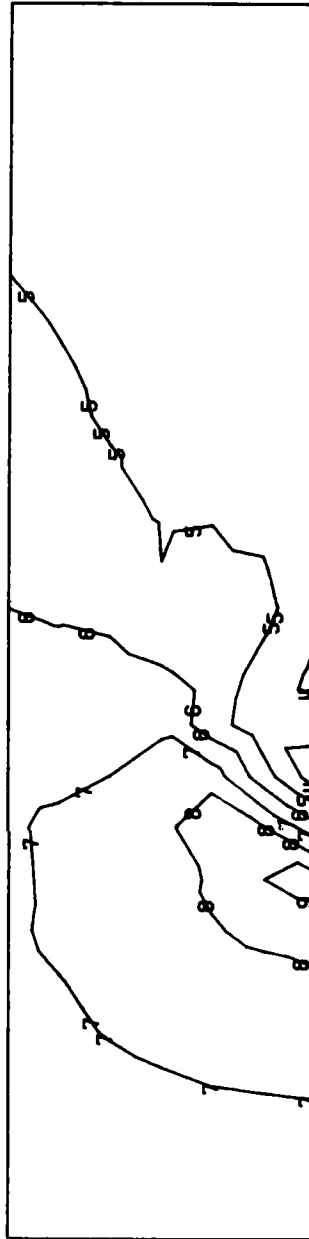
FD 271658
830512
6275B

Figure 3-15. Von Mises Equivalent Stress Contours After Release of Fourth Node at 4725 lb Load Level

3-9

3.2 FATIGUE CRACK GROWTH

Experimental fatigue crack growth rates, both with and without hold periods at the maximum load level, were measured as a function of cycle number. Specimen dimensions and pertinent load data are shown in Figure 3-1.

Experimental crack growth data for the pure fatigue case, in which the compact type specimen was cycled to failure under a triangular load history at 10 cpm, are shown in Table 3-3 and Figures 3-16 through 3-18. Corresponding data for a specimen with the same load history, in which two hold periods of 30 minutes duration at the maximum load level of 3069 lb were applied early in the specimen's life, are shown in Table 3-4 and Figures 3-19 through 3-21. The increase in crack growth rate due to the hold periods is similar to that observed by Sadananda and Shahinian [14].

Attempts at simulating the fatigue crack growth experiments with the finite element mesh shown in Figure 2-31 showed that the mesh surrounding the crack tip was too coarse. A plot of the stress decrease along the crack plane in the compact type specimen for an initial crack length of 0.395 in. at a maximum load of 3069 lb is displayed in Figure 3-22. The finite elements surrounding the crack tip in Figure 2-31 are 0.01 in. in length, and Figure 3-22 shows that the stress decreases by almost a factor of two in the element closest to the crack tip. Moveover, the Gaussian integration point closest to the crack tip experiences a maximum Von Mises equivalent stress of only 108 ksi. The stress amplitude experienced by this integration point is therefore so small (~ 100 ksi) that the number of cycles required to fail or rupture this point is estimated to be several million cycles. Clearly smaller elements are needed in the crack tip vicinity in order to subject the Gaussian integration point closest to the crack tip to a sufficiently high stress amplitude. For the 0.01-inch element the integration point closest to the crack tip experiences an almost elastic history, and 0.003-inch elements would probably be needed to simulate fatigue crack growth for ΔK values around 20,000 lb/in.$^{3/2}$.

Instead of refining the mesh, which would have made the already expensive calculations even more expensive, the simulation of the 3069 lb maximum load fatigue test was abandoned. Of necessity, the simulation of the creep/fatigue interaction was also abandoned.

Finite element calculations of the cyclic crack growth rate as a function of stress intensity factor range, da/dN vs ΔK, were performed with the existing mesh by loading the specimen cyclically to a maximum load of 6000 lb and a minimum load of 1000 lb at 10 cpm. Material constants in the fatigue model were then "fine tuned" to bring the computed da/dN versus ΔK values into agreement with the experimental values obtained from the 3069 lb maximum load fatigue test.

The number of cycles to failure for the multiaxial fatigue model is given by

$$N_f = C(\Delta\sigma_{II})^{-\gamma}(1 - b\sigma_I)^{\beta},$$

(21)

where

$$\sigma_I = \left[\left(\frac{(\sigma_1^{max} + \sigma_1^{min})}{2}\right) + \left(\frac{\sigma_2^{max} + \sigma_2^{min}}{2}\right) + \left(\frac{\sigma_3^{max} + \sigma_3^{min}}{2}\right)\right]$$

(22)

3-10

and

$$\Delta\sigma_{II} = \Big[\frac{\left\{(\sigma_1^{max} - \sigma_1^{min}) - (\sigma_2^{max} - \sigma_2^{min})\right\}^2}{2} +$$

$$\frac{\left\{(\sigma_2^{max} - \sigma_2^{min}) - (\sigma_3^{max} - \sigma_3^{min})\right\}^2}{2} + \frac{\left\{(\sigma_3^{max} - \sigma_3^{min}) - (\sigma_1^{max} - \sigma_1^{min})\right\}^2}{2}\Big]^{1/2}. \tag{23}$$

The quantities σ_i^{max} and σ_i^{min} are the maximum and minimum values of the ith principal stress during the fatigue cycle.

Values for the material constants C and γ were obtained from the uniaxial fatigue tests carried out under stress control with zero mean stress (i.e., $\sigma_I=0$ for these tests). With C = 3.809×10^{90} and $\gamma = 16.625$ the number of cycles to failure computed using equation (21) agrees with the uniaxial test data to within a factor of two.

The material constant b determines the reduction in fatigue life due to an increase in the mean stress. If N_o is the fatigue life for a specified stress amplitude under zero mean stress, then the fatigue life, N, at the same stress amplitude with mean stress, σ_I, is given by

$$\frac{N}{N_o} = (1 - b\sigma_I)^\beta. \tag{24}$$

Table 3-5 shows the results of uniaxial fatigue tests carried out under increasing mean stress values at a stress amplitude of 160 ksi. The scatter in the data precludes a precise determination of b from equation (24). If an average value of $N_o = 16248$ is taken when $\sigma_I = 0$, then the two data points for $\sigma_I = 20$ ksi and $\sigma_I = 40$ ksi give a least square value of $b = 2.6 \times 10^{-6}$. Bui-Quoc [15] suggests a value of $b = 0.78/\sigma_u$ for IN100, where σ_u is the ultimate stress. Using values of 160 ksi and 170 ksi for σ_u gives values of $b = 4.9 \times 10^{-6}$ and $b = 4.6 \times 10^{-6}$ for INCO 718 at 1200°F (649°C).

The value of b may now be "fine-tuned" so that the finite element calculation of da/dN versus ΔK agrees with the experimentally determined values. For a compact type specimen with W = 2.0 in., t = 0.5 in., $P_{max} = 6000$ lb, $P_{min} = 1000$ lb and a = 0.395 in., we find that $\Delta K = 30,000$ lb/in.$^{3/2}$. From Table 3-3 the value of da/dN is found to be approximately 4.5×10^{-5} in. per cycle. The finite elements surrounding the crack tip have a length of 0.01 in., and the crack advances half way through an element every time the Gaussian integration point closest to the crack tip fails. Thus, the finite element value of da/dN is obtained from the relation

$$\frac{da}{dN} = \frac{0.005}{N_f}, \tag{25}$$

where N_f is the number of cycles required for failure of the integration point under a stress amplitude $\Delta\sigma_{II}$ and mean stress σ_I. The value of N_f is obtained from equation (21) assuming that the integration point experiences a constant stress amplitude and mean stress until failure occurs. The average values of $\Delta\sigma_{II}$ and σ_I at the integration points closest to the crack tip during the first four node releases were determined to be $\Delta\sigma_{II} = 128,000$ psi and $\sigma_I = 100,000$ psi, with considerable scatter about these values. We therefore obtain from

$$N_f = C(\Delta\sigma_{II})^{-\gamma}(1-b\sigma_I)^{\beta} \text{ and } \frac{da}{dN} = \frac{0.005}{N_f} = 4.5 \times 10^{-5}$$

the relation

$$C(\Delta\sigma_{II})^{-\gamma}(1-b\sigma_I)^{\beta} = \frac{0.005}{4.5 \times 10^{-5}}.$$

Taking $C = 3.809 \times 10^{90}$, $\gamma = 16.625$, $\beta = 9.14$, $\Delta\sigma_{II} = 128,000$, $\sigma_I = 100,000$ gives $b = 5.99 \times 10^{-6}$. At first sight this value of b appears to be in reasonable agreement with the values deduced earlier from uniaxial tests and from taking $b = 0.78/\sigma_u$. However, an examination of Table 3-6 reveals the extreme sensitivity of the number of cycles to failure, N_f, to changes in the constant, b, at values of $\Delta\sigma_{II} = 128,000$ psi and $\sigma_I = 100,000$ psi.

Since $da/dN = 0.005/N_f$, it is readily apparent that slight inaccuracies in the determination of b will affect the computed fatigue crack propagation rate by many orders of magnitude. This variability arises from the fact that $b\sigma_I$ can vary from 0.2 to 0.8 as b ranges from 2×10^{-6} to 8×10^{-6} with $\sigma_I = 100,000$ psi. Values of $1 - b\sigma_I$ when raised to the power of β, with $\beta \approx 9$, therefore may change by many orders of magnitude. This sensitivity to mean stress arises from the very large value of the mean stress σ_I in the crack tip vicinity. The cyclic life is also very sensitive to changes in the stress amplitude, $\Delta\sigma_{II}$, since this quantity is raised to the power of γ, where $\gamma \approx$ 16. This sensitivity to stress amplitude can also be seen by examining Figure 3-23 which compares fatigue data obtained by Thakker and Cowles [9] to data obtained by the General Electric Company. From this figure it may be observed that cyclic life increases from 5000 cycles to about 1,000,000 cycles for a slight decrease in total strain amplitude.

The sensitivity of cyclic life to mean stress is, in some measure, due to the assumption embodied in equation (4) for the exponent α, which leads to the result expressed in equation (24). If more experimental data on mean stress effects had been gathered, the exponent α could have been fitted to obtain the form proposed by Chaboche [8], viz.

$$\alpha = 1 - a\frac{\sigma_{max} - \sigma_{\ell}^{\bullet}}{\sigma_u - \sigma_{max}} \tag{26}$$

with

$$\sigma_{\ell}^{\bullet} = \sigma_{\ell} + (1-b\sigma_{\ell})\sigma_{mean}. \tag{27}$$

In these equations σ_{max} and σ_{mean} are the maximum and mean stresses in the cycle, σ_u is the ultimate stress, and σ_{ℓ} is the fatigue limit. This form would no doubt reduce the sensitivity of cyclic life to mean stress effects, but fatigue lives in Table 3-6 indicate that extrapolation of cyclic life to mean stress values encountered at the crack tip is liable to uncertainty.

Table 3-3.   *Crack Growth Data for Compact Type Specimen Under Pure Fatigue at 10 cpm*

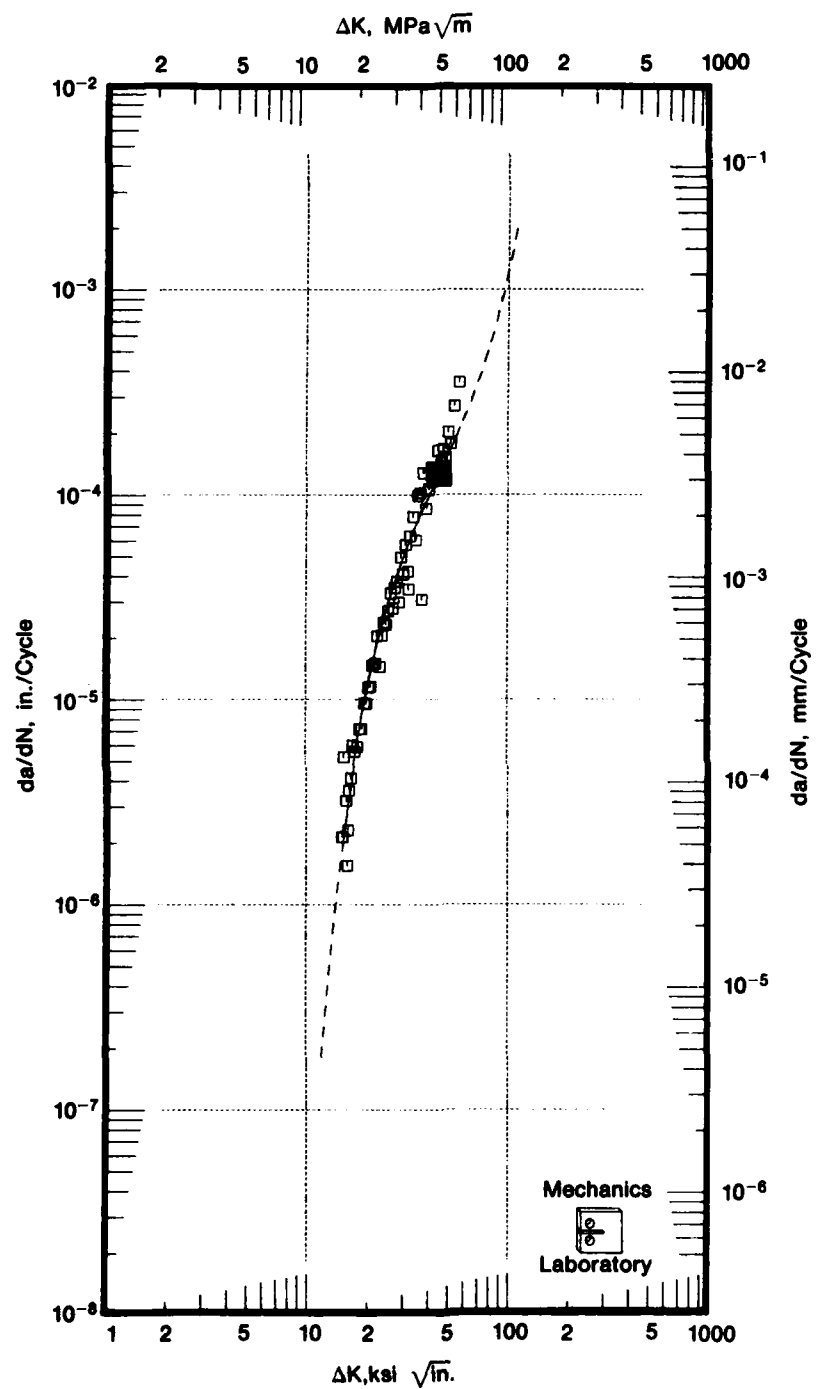| Cycles	a	K_{max}	Direct Secant Method		Seven Point Incremental Polynomial Method	
			ΔK	da/dN	ΔK	da/dN
1100.00	0.505					
15000.0	0.513	16.76	15.08	2.137E-06		
19000.0	0.522	16.93	15.23	2.138E-06		
23000.0	0.543	17.22	15.50	5.225E-06	15.63	2934E-06
27000.0	0.555	17.56	15.80	3.187E-06	15.86	2.971E-06
31000.0	0.562	17.75	15.97	1.538E-06	16.05	3.068E-06
35000.0	0.571	17.90	16.11	2.300E-06	16.21	3.223E-06
39000.0	0.585	18.14	16.33	3.600E-06	16.46	3.768E-06
44000.0	0.606	18.50	16.65	4.110E-06	16.87	4.690E-06
49000.0	0.636	19.02	17.11	5.970E-06	17.36	5.482E-06
53500.0	0.661	19.59	17.63	5.556E-06	17.86	6.077E-06
57500.0	0.684	20.10	18.09	5.863E-06	18.34	6.817E-06
61000.0	0.709	20.62	18.56	7.171E-06	18.80	7.587E-06
64000.0	0.731	21.13	19.02	7.167E-06	19.26	8.571E-06
67000.0	0.759	21.69	19.52	9.600E-06	19.81	9.699E-06
69000.0	0.778	22.24	20.01	9.500E-06	20.21	1.077E-05
71000.0	0.801	22.72	20.45	1.140E-05	20.69	1.193E-05
73000.0	0.824	23.26	20.94	1.152E-05	21.20	1.359E-05
75000.0	0.853	23.89	21.50	1.460E-05	21.83	1.503E-05
76500.0	0.876	24.53	22.08	1.493E-05	22.37	1.622E-05
78000.0	0.906	25.21	22.69	2.033E-05	22.96	1.781E-05
79500.0	0.928	25.90	23.31	1.437E-05	23.62	1.960E-05
80500.0	0.948	26.46	23.82	2.045E-05	24.11	2.131E-05
81500.0	0.972	27.08	24.37	2.370E-05	24.63	2.358E-05
82500.0	0.995	27.75	24.98	2.320E-05	25.30	2.617E-05
83500.0	1.022	28.50	25.65	2.695E-05	26.04	2.868E-05
84300.0	1.049	29.32	26.39	3.306E-05	26.71	3.104E-05
85000.0	1.068	30.06	27.05	2.793E-05	27.38	3.239E-05
85700.0	1.093	30.79	27.71	3.500E-05	28.08	3.524E-05
86200.0	1.112	31.53	28.38	3.770E-05	28.63	3.729E-05
86700.0	1.126	32.13	28.92	2.980E-05	29.24	4.113E-05
87200.0	1.151	32.86	29.57	4.950E-05	29.94	4.438E-05
87700.0	1.172	33.71	30.34	4.090E-05	30.74	4.705E-05
88200.0	1.200	34.69	31.22	5.690E-05	31.66	5.031E-05
88400.0	1.209	35.45	31.90	4.225E-05	32.01	5.520E-05
88600.0	1.215	35.77	32.20	3.450E-05	32.45	5.731E-05
89000.0	1.241	36.47	32.82	6.288E-05	33.34	6.320E-05
89400.0	1.272	37.74	33.97	7.775E-05	34.49	7.573E-05
89700.0	1.290	38.92	35.03	6.000E-05	35.58	7.561E-05
89900.0	1.309	39.87	35.88	9.875E-05	36.30	8.066E-05
90100.0	1.330	40.91	36.82	1.018E-04	37.06	8.379E-05
90300.0	1.336	41.63	37.47	3.075E-05	37.93	8.939E-05
90500.0	1.362	42.52	38.27	1.277E-04	38.80	9.458E-05
90700.0	1.379	43.77	39.39	8.550E-05	39.84	1.025E-04
90900.0	1.400	44.94	40.45	1.065E-04	41.11	1.176E-04
91100.0	1.425	46.44	41.79	1.258E-04	42.48	1.266E-04
91300.0	1.449	48.12	43.30	1.195E-04	44.19	1.407E-04
91500.0	1.482	50.18	45.16	1.635E-04	45.20	1.517E-04
91600.0	1.496	52.01	46.81	1.420E-04	47.31	1.605E-04
91700.0	1.512	53.27	47.94	1.650E-04	48.58	1.676E-04
91800.0	1.528	54.63	49.17	1.525E-04	49.81	1.810E-04
91900.0	1.548	56.22	50.59	2.015E-04	51.26	2.120E-04
92000.0	1.565	58.00	52.20	1.765E-04		
92100.0	1.592	60.24	54.21	2.705E-04		
92200.0	1.628	63.60	57.24	3.525E-04		

AMS 5596 1200F (649C) Air 10 CPM R = 0.1
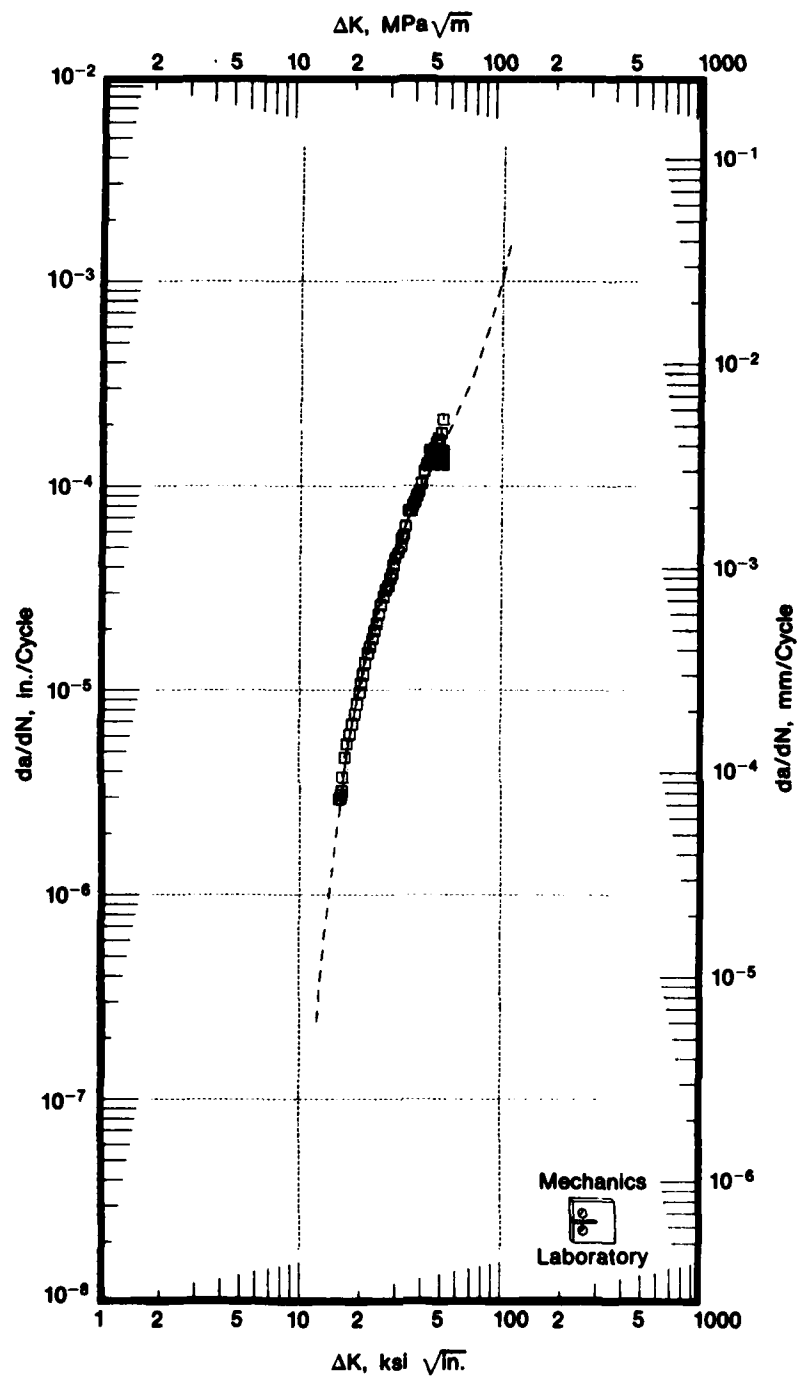a_o = 0.373 in. P_{max} = 3069 lb P_{min} = 307 lb W = 2.501 in. B = 0.500 in.
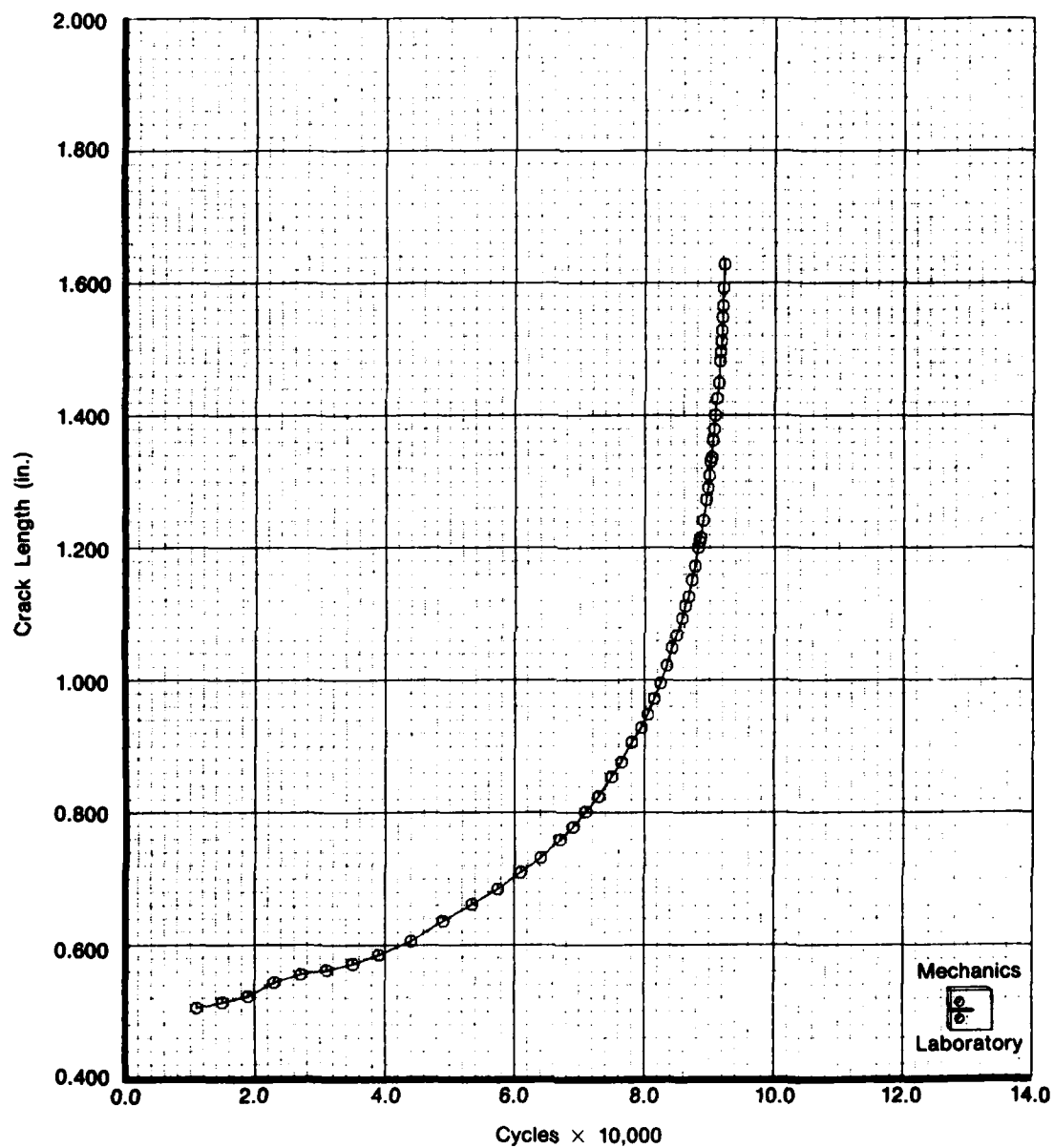
FD 271659

Figure 3-16. *Crack Length vs Cycle Number for Compact Type Specimen in Pure Fatigue*

Figure 3-17. Correlation of Pure Fatigue Crack Growth Rate Data With ΔK by Direct Secant Method

FD 271660

42044

ΔK, MPa√m̄

FD 271661

Figure 3-18. *Correlation of Pure Fatigue Crack Growth Rate Data With ΔK by Seven Point Incremental*
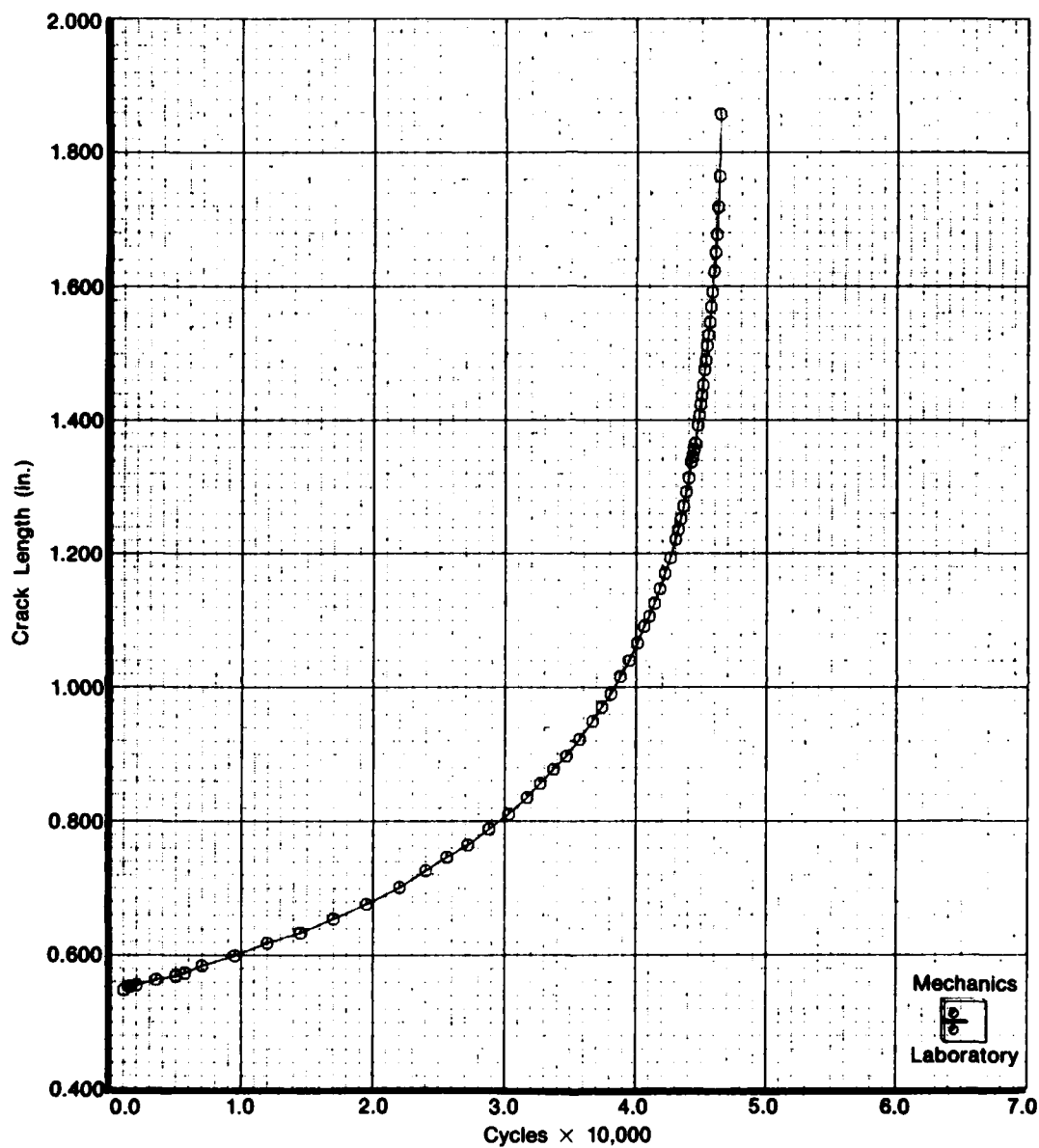
Table 3-4. Crack Growth Data for Compact Type Specimen Under Creep/Fatigue Interaction With 10 cpm Fatigue Cycle

Cycles	a	K_{max}	Direct Secant Method		Seven Point Incremental Polynomial Method	
			ΔK	da/dN	ΔK	da/dN
11000.0	0.548					
11500.0	0.553	17.54	15.79	1.080E-05		
30 Minute Dwell						
12000.0	0.555	17.62	15.85	3.500E-06		
13500.0	0.563	17.71	15.94	5.400E-06	16.00	5.376E-06
15000.0	0.569	17.86	16.08	4.300E-06	16.15	5.640E-06
15700.0	0.573	17.96	16.17	5.214E-06	16.22	5.915E-06
30 Minute Dwell						
17000.0	0.584	18.11	16.30	8.231E-06	16.38	6.418E-06
19500.0	0.599	18.38	16.54	6.300E-06	16.69	6.912E-06
22000.0	0.618	18.73	16.86	7.500E-06	17.00	7.216E-06
24500.0	0.633	19.08	17.17	6.120E-06	17.34	7.717E-06
27000.0	0.654	19.45	17.51	8.120E-06	17.70	8.653E-06
29500.0	0.676	19.90	17.91	8.920E-06	18.12	9.816E-06
32000.0	0.701	20.41	18.37	9.880E-06	18.64	1.094E-05
34000.0	0.726	20.95	18.86	1.275E-05	19.09	1.188E-05
35600.0	0.746	21.46	19.31	1.256E-05	19.48	1.273E-05
37200.0	0.764	21.88	19.69	1.109E-05	19.91	1.381E-05
38800.0	0.788	22.35	20.12	1.469E-05	20.36	1.520E-05
40300.0	0.810	22.89	20.60	1.520E-05	20.85	1.709E-05
41700.0	0.835	23.46	21.12	1.786E-05	21.40	1.879E-05
42700.0	0.856 ·	24.02	21.62	2.075E-05	21.83	2.015E-05
43700.0	0.877	24.54	22.09	2.100E-05	22.31	2.180E-05
44700.0	0.897	25.07	22.56	2.035E-05	22.82	2.356E-05
45700.0	0.922	25.66	23.09	2.470E-05	23.39	2.547E-05
46700.0	0.949	26.35	23.72	2.685E-05	24.04	2.848E-05
47400.0	0.970	27.01	24.31	2.950E-05	24.57	3.053E-05
48100.0	0.990	27.60	24.84	2.900E-05	25.14	3.312E-05
48800.0	1.016	28.28	25.45	3.736E-05	25.77	3.666E-05
49500.0	1.040	29.04	26.14	3.393E-05	26.52	3.984E-05
50100.0	1.066	29.83	26.85	4.317E-05	27.25	4.242E-05
50600.0	1.091	30.67	27.60	5.000E-05	27.90	4.551E-05
51000.0	1.106	31.35	28.22	3.750E-05	28.49	4.836E-05
51400.0	1.125	31.95	28.76	4.725E-05	29.11	5.092E-05
51800.0	1.147	32.71	29.44	5.173E-05	29.79	5.458E-05
52200.0	1.170	33.57	30.21	5.538E-05	30.59	6.009E-05
52600.0	1.193	34.47	31.02	5.913E-05	31.49	6.578E-05
53000.0	1.221	35.53	31.98	6.963E-05	32.52	7.466E-05
53200.0	1.236	36.46	32.81	7.400E-05	33.12	8.228E-05
53400.0	1.252	37.16	33.44	8.150E-05	33.81	8.911E-05
53600.0	1.271	37.97	34.17	9.350E-05	34.58	9.701E-05
53800.0	1.292	38.94	35.04	1.070E-04	35.50	1.029E-04
54000.0	1.313	40.00	36.00	1.032E-04	36.51	1.060E-04
54200.0	1.337	41.19	37.07	1.225E-04	37.57	1.027E-04
54300.0	1.345	42.07	37.87	7.501E-05	38.07	1.097E-04
54400.0	1.356	42.60	38.34	1.100E-04	38.62	1.143E-04
54500.0	1.365	43.17	38.85	8.600E-05	39.15	1.159E-04
54700.0	1.392	44.26	39.83	1.382E-04	40.61	1.384E-04
54800.0	1.407	45.60	41.04	1.505E-04	41.46	1.436E-04
54900.0	1.423	46.61	41.95	1.580E-04	42.36	1.578E-04
55000.0	1.437	47.63	42.86	1.395E-04	43.35	1.623E-04
55100.0	1.452	48.65	43.78	1.495E-04	44.41	1.712E-04
55200.0	1.475	50.05	45.04	2.295E-04	45.63	1.774E-04
55300.0	1.489	51.48	46.33	1.400E-04	46.97	1.838E-04
55400.0	1.511	52.92	47.63	2.160E-04	48.35	1.902E-04
55500.0	1.527	54.56	49.11	1.685E-04	49.79	1.941E-04

3-17

Table 3-4.   Crack Growth Data for Compact Type Specimen Under
             Creep/Fatigue Interaction With 10 cpm Fatigue Cycle
             (Continued)

Cycles	a	K_{max}	Direct Secant Method		Seven Point Incremental Polynomial Method	
			ΔK	da/dN	ΔK	da/dN
55600.0	1.546	56.18	50.56	1.910E-04	51.40	2.152E-04
55700.0	1.569	58.15	52.34	2.255E-04	53.28	2.331E-04
55800.0	1.591	60.38	54.34	2.165E-04	55.64	2.538E-04
55900.0	1.622	63.27	56.94	3.180E-04	58.29	2.819E-04
56000.0	1.650	66.76	60.08	2.745E-04	61.41	3.189E-04
56100.0	1.677	70.29	63.26	2.755E-04	64.86	4.108E-04
56200.0	1.718	75.08	67.57	4.005E-04		
56300.0	1.764	82.02	73.82	4.620E-04		
56400.0	1.857	95.79	86.21	9.370E-04		

AMS 5596 1200F (649C) AIR 10 CPM R=0.1
$a_o = 0.374$ in. $P_{max} = 3070$ lb $P_{min} = 307$ lb $W = 2.498$ in. $B = 0.502$ in.

FD 271662

Figure 3-19. Crack Length vs Cycle Number for Compact Type Specimen Under Creep/Fatigue Interactions
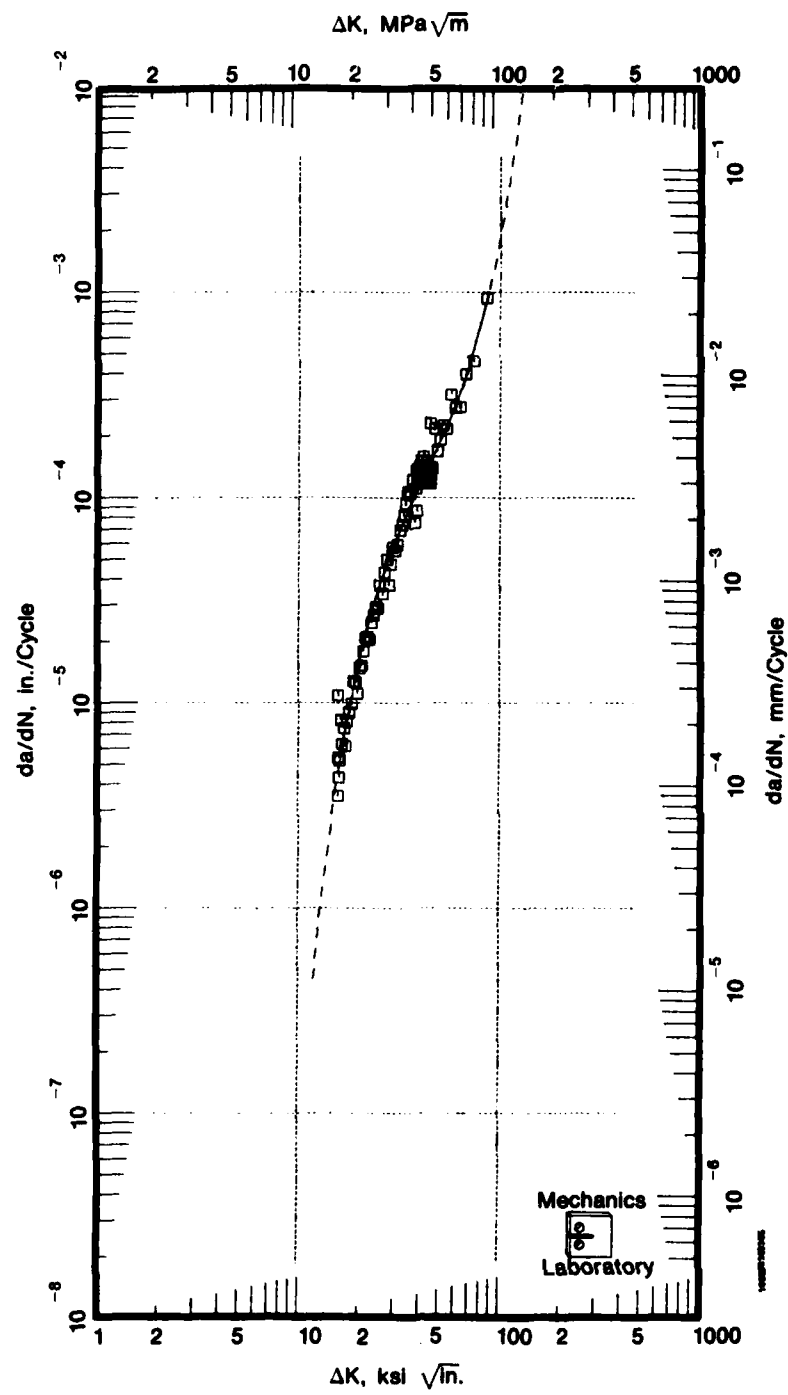
FD 271663

Figure 3-20. *Correlation of Creep/Fatigue Crack Growth Rate Data With ΔK by Direct Secant Method*

FD 271664
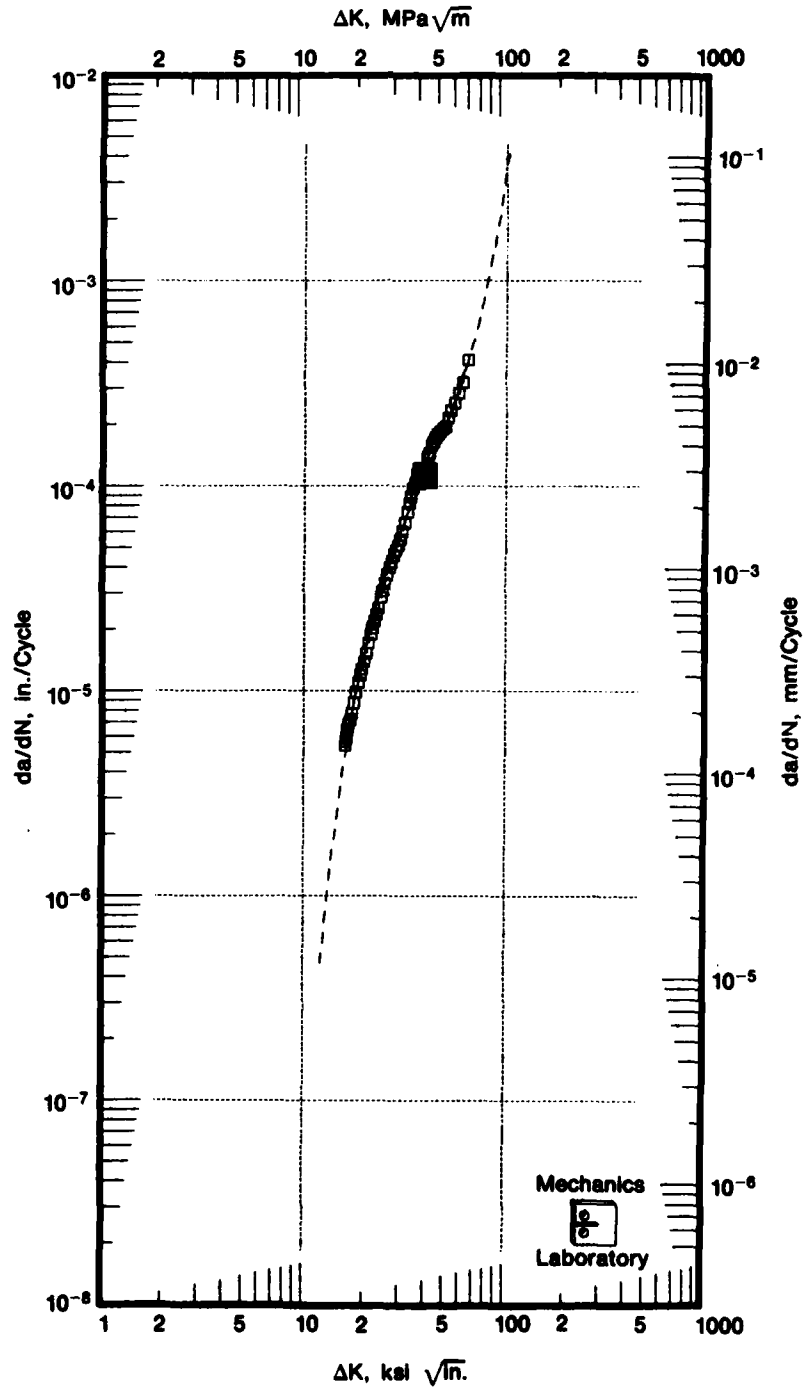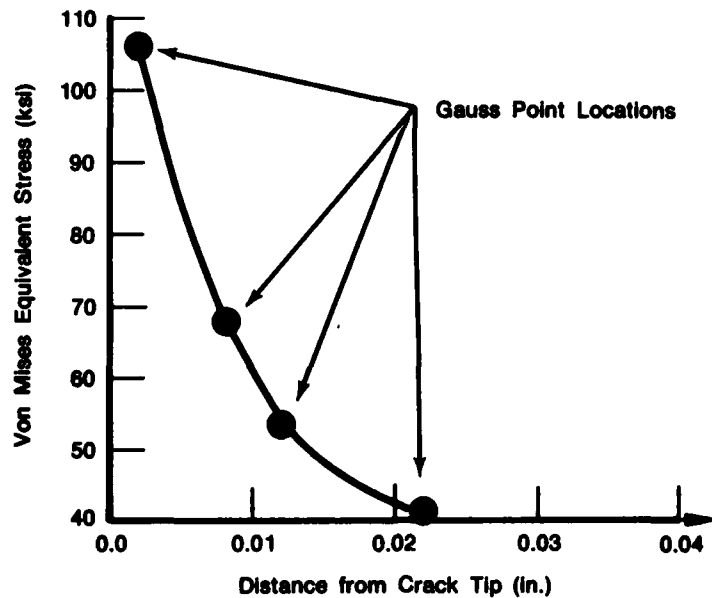
Figure 3-21. Correlation of Creep/Fatigue Crack Growth Rate Data With ΔK by Seven Point Incremental Polynominal Method

FD 271665

Figure 3-22. Stress Decrease Along Crack Plane in Compact Type Specimen for Initial
Crack Length a = 0.395 in. at Maximum Load of 3069 lb

Table 3-5.   Effect of Mean Stress on Fatigue Life of INCO
                  718 at 1200°F (649°C)

Stress Range (ksi) $\Delta\sigma_{II}$	Mean Stress (ksi) σ_I	N_f (Experiment)
160 (+80) (−80)	0	9,671 and 22,826
160 (+100) (−60)	20	14,182
160 (+120) (−40)	40	8,580

Table 3-6.   Sensitivity   of N_f and
               da/dN to Changes in the
               Mean Stress Constant b at
               $\Delta\sigma_{II}$ = 128,000 psi and σ_I
               = 100,000 psi

b	N_f	da/dN = 0.005/N_f
8×10^{-6}	0.19	2.6×10^{-2}
7×10^{-6}	8	6.3×10^{-4}
6×10^{-6}	109	4.6×10^{-5}
5×10^{-6}	836	6.0×10^{-6}
4×10^{-6}	4,423	1.1×10^{-6}
3×10^{-6}	18,098	2.8×10^{-7}
2×10^{-6}	61,332	8.2×10^{-8}
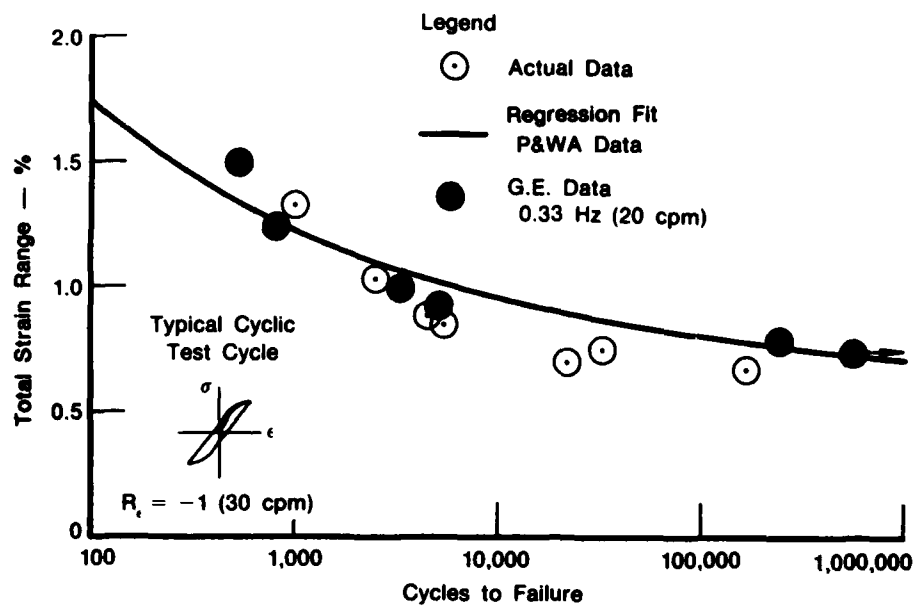
Figure 3-23. *Total Strain Range vs Cycles to Failure for Fully Reversed Continuous Cycle INCO 718 Data at 649°C (1200°F)*

FD 258492

SECTION 4.0

CONCLUSIONS AND RECOMMENDATIONS

4.1 CONCLUSIONS

Creep and fatigue crack growth have been measured in compact type specimens of INCO 718 at 1200°F (649°C). Theoretical predictions of crack growth were made by employing the ABAQUS nonlinear general purpose finite element program in conjunction with a unified viscoplastic constitutive model and a continuum damage failure criterion.

Conclusions for the current program are summarized as follows:

A. Initial creep crack growth rates at 1200°F (649°C) in the INCO 718 compact type specimens can be predicted by the theoretical model. Crack growth is assumed to take place due to creep rupture of the material in the immediate vicinity of the crack tip and material constants for the continuum damage creep failure model were determined from creep rupture tests on uniaxial bar specimens of INCO 718 at 1200°F (649°C). Calculations were performed under plane stress conditions.

B. The differential form of the unified viscoplastic constitutive model becomes very unstable when continuum damage is included in the formulation. It appears that an integral formulation of the unified viscoplastic model should be used to obtain a stable integration algorithm.

C. Speckle interferometry appears well suited for high temperature creep crack growth measurement.

D. Fatigue crack growth computations in compact type specimens made of INCO 718 require a very fine finite element mesh in the vicinity of the crack tip. The crack growth rate obtained from the continuum damage fatigue model is sensitive to the large mean stress in the crack tip vicinity. Uniaxial fatigue tests should be conducted at large mean stress values to avoid extrapolation from tests carried out at small mean stresses. In the computations carried out under the present contract the 0.01 in. finite elements were too large and the continuum damage fatigue model required too much extrapolation from small mean stress values to verify the failure criterion.

4.2 RECOMMENDATIONS

Based on the experience gained in the present contract it is evident that:

A. Continuum damage models should be included in integral formulations of unified viscoplastic constitutive models.

B. Boundary Element Programs should be modified to allow viscoplastic and continuum damage theories to be incorporated. These programs could then be used to compute crack growth under full three dimensional loading conditions.

4314C

C. Crack growth under general and thermomechanical loading conditions should be studied in both an experimental and theoretical framework.

D. Fatigue experiments should be conducted under conditions similar to those experienced in the vicinity of a crack tip, viz. under high mean stress conditions and biaxial loading conditions.

REFERENCES

1. Users Manual, Example Problems Manual, Systems Manual and Theory Manual for the ABAQUS general purpose nonlinear finite element program developed by Hibbitt, Karlsson & Sorensen, Inc., 35 South Angell St., Providence, R.I. 02906.

2. Miller, A. K., "An Inelastic Constitutive Model for Monotonic, Cyclic, and Creep Deformation," Part I "Equations Development and Analytical Procedures" and Part II "Application to Type 304 Stainless Steel," ASME J. of Eng. Mat. Tech., Vol. 98, No. 2, pp. 97-113, 1976.

3. Kobayashi, A. S., "Current and Future Experimental Methods," *Fracture Mechanics,* Edited by N. Perrone, H. Liebowitz, D. Mulville and W. Pilkey, 10th Symposium on Naval Structural Mechanics, Washington, D.C., 1978.

4. Hinnerichs, T. D., *Viscoplastic and Creep Crack Growth Analysis by the Finite Element Method,* Report AFWAL-TR-80-4140, Wright-Patterson Air Force Base, Ohio, 1981.

5. Sharpe, Jr., W. N., Unpublished Data on USAF Contract F33615-77-C-5003, Wright-Patterson Air Force Base, Ohio, 1979, (Cf. reference 3).

6. Domas, P. A., W. N. Sharpe, M. Ward, and J. Yau, *Benchmark Notch Test for Life Prediction,* Final Report NASA CR-165571 on NASA Lewis Contract NAS3-22522, 1982.

7. Walker, K. P., *Research and Development Program for Nonlinear Structural Modeling With Advanced Time-Temperature Dependent Constitutive Relationships,* Final Report NASA CR-165533 on NASA Lewis Contract NAS3-22055, 1981.

8. Chaboche, J. L., "Thermodynamic and Phenomenological Description of Cyclic Viscoplasticity With Damage," Translation of Publication No. 1978-3 of the Office National d'Etudes et de Researches Aerospatiales, France, by the European Space Agency Technical Translation Service, Publication Number ESA-TT-548, 1979.

9. Thakker, A. B., and B. A. Cowles, *Low Strain, Long Life Creep Fatigue of AF2-1DA and INCO 718,* Final Report NASA CR-167989 on NASA Lewis Contract NAS3-22387, 1983.

10. Atluri, S. N., and M. Nakagaki, AIAA Journal, Vol. 15, No. 7, pp. 923-931, 1977.

11. ASTM E647-83, Section 9.3.1.

12. Brebbia, C. A., "The Boundary Element Method for Engineers," Halsted Press.

13. Banerjee, P. K., and R. Butterfield, "Boundary Element Methods in Engineering Science," McGraw-Hill.

14. Sadananda, K., and P. Shahinian, "Elastic-Plastic Fracture Mechanics for High Temperature Fatigue Crack Growth," Proceedings of the Twelfth Symposium on Fracture Mechanics, ASTM STP 700, pp. 152-163, 1980.

15. Bui-Quoc, T., "An Engineering Approach for Cumulative Damage in Metals Under Creep Loading," Journal of Engineering Materials and Technology, Vol. 101, pp. 337-343, 1979.

APPENDIX A

COUPLED CONTINUUM DAMAGE/INTEGRAL VISCOPLASTIC FORMULATION

$$\sigma_{ij}(t) = \frac{2}{3}\Omega_{ij}(t) + (\lambda(t) + \frac{2}{3}\mu(t))(1 - D(t))\delta_{ij}\epsilon_{kk} + \int_o^t e^{-\left|Q(t) - Q(\xi)\right|}\left\{2\mu(\xi)(1 - D(\xi))\frac{\delta\epsilon_{ij}}{\delta\xi}\right.$$

$$\left. - \frac{2}{3}\mu(\xi)(1 - D(\xi))\delta_{ij}\frac{\delta\epsilon_{kk}}{\delta\xi} - \frac{2}{3}\frac{\delta\Omega_{ij}}{\delta\xi} + \frac{1}{\mu(\xi)}\frac{\delta\mu}{\delta\xi}\frac{2}{3}\Omega_{ij}(\xi)\right\}d\xi \ , \tag{1}$$

$$\Omega_{ij}(t) = \overset{\circ}{\Omega}_{ij}(t) + n_1(t)c_{ij}(t) + n_2(t)\int_o^t e^{-\left|G(t) - G(\xi)\right|}\frac{\delta c_{ij}}{\delta\xi}d\xi \ , \tag{2}$$

$$K(t) = K_1(t) - K_2(t)_e{}^{-n_7(t)R(t)} \ , \tag{3}$$

$$c_{ij}(t) = \epsilon_{ij}(t) + \frac{\lambda(t)}{2\mu(t)}\delta_{ij}\epsilon_{kk}(t) - \frac{\sigma_{ij}(t)}{2\mu(t)(1 - D(t))} \ , \tag{4}$$

$$\overset{\circ}{\Omega}_{ij}(t) = -\delta_{ij}\overset{\circ}{\Omega}(t) + 3\overset{\circ}{\Omega}(t)\frac{c_{ik}(t)c_{kj}(t)}{c_{pq}(t)c_{pq}(t)} \ , \tag{5}$$

$$Q(t) = \int_o^t\left\{\frac{3\mu(\xi)}{K(\xi)}\frac{1}{\log(1 + \beta\frac{\delta R}{\delta\xi})}\frac{\delta R}{\delta\xi} - \frac{1}{\mu(\xi)}\frac{\delta\mu}{\delta\xi}\right\}d\xi, \ , \tag{6}$$

$$G(t) = \int_o^t (n_3(\xi) + n_4(\xi)_e{}^{-n_5(\xi)R(\xi)})\frac{\delta R}{\delta\xi}d\xi \ , \tag{7}$$

$$R(t) = \int_o^t\sqrt{\frac{2}{3}\frac{\delta c_{ij}}{\delta\xi}\frac{\delta c_{ij}}{\delta\xi}}d\xi \ . \tag{8}$$

APPENDIX B

UNIFIED VISCOPLASTIC EXPONENTIAL LAW FOR UNIFIED FORMULATION

$$\dot{c}_{ij} = \frac{\exp\left(\frac{\sqrt{2/3(3s_{ij}/2 - \Omega_{ij})(3s_{ij}/2 - \Omega_{ij})}}{K(1-D)}\right) - 1}{\beta} \cdot \frac{(3s_{ij}/2 - \Omega_{ij})}{\sqrt{2/3(3s_{ij}/2 - \Omega_{ij})(3s_{ij}/2 - \Omega_{ij})}}, \tag{1}$$

$$\dot{\Omega}_{ij} = n_2 \dot{c}_{ij} - \dot{G}_1 \Omega_{ij}, \tag{2}$$

$$\dot{G}_1 = (n_3 + n_4 e^{-n_5 R}) \dot{R}, \tag{3}$$

$$K = K_1 + K_2 e^{-n_7 R}, \tag{4}$$

$$\dot{\sigma}_{ij} = \delta_{ij}\lambda(1-D)\dot{\epsilon}_{kk} + 2\mu(1-D)(\dot{\epsilon}_{ij} - \dot{c}_{ij}) + \delta_{ij}\overline{\lambda(1-D)}\epsilon_{kk} + \overline{2\mu(1-D)}(\epsilon_{ij} - c_{ij}), \tag{5}$$

$$\dot{R} = \sqrt{2/3\dot{c}_{ij}\dot{c}_{ij}} \tag{6}$$

$$s_{ij} = \sigma_{ij} - \frac{1}{3}\delta_{ij}\sigma_{kk}. \tag{7}$$

The constants are chosen to have the values:

$\lambda = 1.517\ E7$, $\mu = 1.012\ E7$, $K_1 = 4219$, $K_2 = -1438$, $\beta = 6.203\ E9$, $n_2 = 22.4\ E6$, $n_3 = 269.6$, $n_4 = 0$, $n_5 = 0$, $n_7 = 14$.

For no cyclic softening $K_1 = 5657$ and $K_2 = 0$.

APPENDIX C

CHABOCHE'S CREEP DAMAGE MODEL

$$D_C = A \left\langle \frac{\sqrt{3/2\, S_{ij}\, S_{ij}}}{1 - D_C} \right\rangle^r \quad (1 - D_C)^{r-k}, \tag{1}$$

$$k = 1 + (1.011 \times 10^{-4}) \exp (9.446 \times 10^{-5} \sqrt{3/2\, S_{ij}\, S_{ij}}) \tag{2}$$

The constants are chosen to have the values:

$A = 2.394 \times 10^{-43}$, $r = 7.22$.

43170

APPENDIX D

CHABOCHE'S FATIGUE DAMAGE MODEL

$$\frac{dD_f}{dN} = \left[1 - (1-D_f)^{\beta+1}\right]^\alpha \left[\frac{\Delta\sigma_{II}}{M_o\,(1-b\sigma_I)\,(1-D_f)}\right]^\beta, \tag{1}$$

$$\alpha = \alpha(\Delta\sigma_{II},\sigma_I), \tag{2}$$

$$\sigma_I = \left[\left(\frac{\sigma_1^{max}+\sigma_1^{min}}{2}\right) + \left(\frac{\sigma_2^{max}+\sigma_2^{min}}{2}\right) + \left(\frac{\sigma_3^{max}+\sigma_3^{min}}{2}\right)\right], \tag{3}$$

$$\Delta\sigma_{II} = \left[\frac{\left\{\sigma_1^{max}-\sigma_1^{min})-(\sigma_2^{max}-\sigma_2^{min})\right\}^2}{2} + \frac{\left\{(\sigma_2^{max}-\sigma_2^{min})-(\sigma_3^{max}-\sigma_3^{min})\right\}^2}{2}\right.$$

$$\left. + \frac{\left\{(\sigma_3^{max}-\sigma_3^{min})-(\sigma_1^{max}-\sigma_1^{min})\right\}^2}{2} \right]^{1/2} \tag{4}$$

where σ_i^{max} and σ_i^{min} are the maximum and minimum values of the ith principal stress during the fatigue cycle.

END

FILMED

1-84

DTIC